UNIVERSITÀ DEGLI STUDI DI PADOVA

UNIVERSITA' DEGLI STUDI DI PADOVA

Dipartimento di Ingegneria Industriale DII

Corso di Laurea Magistrale in Ingegneria Aerospaziale

The Impact of the Inlet Flow Profile on the Unsteady Swirl Distortion Characteristics of an S-Duct Intake Using Stereo PIV Methods

Relatore: prof. Ernesto Benini

Laureanda: Alessia Gloder

Anno Accademico 2018/2019

To Flavio and Fiorella

ABSTRACT (ENG)

Propulsion system integration has attracted a lot of attention in the last decades and convoluted engines are expected to play a major role in the next generation of aircraft. Despite the major improvements in terms of power input and fuel consumption, convoluted diffusing ducts generate notable unsteadiness, which affects the engine performance and operability. Conventional measurements are insufficient to capture the unsteady nature of the flow field, and the need for synchronous, unsteady, high-spatial-resolution measurements such as Stereoscopic Particle Image Velocimetry is evident. Previous work shown by the Cranfield University group has demonstrated swirl distortion measurements and analysis at the exit plane of the studied configurations, but there is still work to be done with non-uniform flow profiles at the inlet of the S-duct. In this investigation, Stereo Particle Image Velocimetry has been applied at the Aerodynamic Interface Plane of a high-offset S-duct to quantify the unsteady flow distortion caused by the ingestion of a non-uniform flow profile at different inlet locations.

The results revealed enhanced flow distortion in terms of both time-averaged and unsteady levels and patterns. The flow was demonstrated to be highly unsteady, while steady data were proven to be misleading of the flow behaviour. High swirl intensities were generally observed, with peak values at the inner-most radial position. The pattern of the unsteady swirl distortion significantly deviated from the classical twin swirl configuration and multiple swirling regions could be observed. Different swirl patterns of different intensities drove the flow distortion depending on the ingestion location and on the investigated radial position. The results allow to have a greater understanding of the impact of the inlet flow profile on the unsteady aerodynamic at the exit of an S-duct intake and give access to more reliable datasets about the aerodynamic performance of S-ducts.

Keywords:

Non-uniform flow profile, S-duct, S-PIV, Unsteady flow distortion, swirl distortion.

ABSTRACT (ITA)

L'integrazione di nuovi sistemi propulsivi ha attratto notevole attenzione negli ultimi decenni, ed è chiaro ormai che essi saranno di fondamentale importanza in futuro. Nonostante i notevoli progressi fatti in termini di potenza in ingresso e consumo di carburante, però, l'integrazione di prese d'aria diffusive porta ancora a notevoli instabilità, influendo negativamente sulla performance e operabilità di un motore. I sistemi di misura convenzionali sono inoltre limitati e inadeguati per misure non stazionarie del profilo fluido caratteristico dei motori integrati, rendendo evidente la necessità di un sistema di misura sincrono e dotato di grande risoluzione spaziale. Una tecnica ottica sperimentale che soddisfa questi requisiti è la Stereoscopic Particle Image Velocimetry (S-PIV), non di uso comune nel campo industriale.

Precedente lavoro svolto dal gruppo di ricerca dell'Università di Cranfield ha visto l'applicazione della tecnica S-PIV al piano di interfaccia aerodinamico di prese d'aria integrate di diversa geometria, con l'obiettivo di misurare e analizzare le distorsioni del profilo fluido turbolento associato a tali prese, ottenendo notevoli risultati. Nonostante questo, rimane ancora molto lavoro da svolgere relativamente a profili fluidi non uniformi in ingresso a prese d'aria con geometria ad S.

Nel presente lavoro la tecnica S-PIV è stata applicata al Piano di Interfaccia Aerodinamico di una presa d'aria ad S di geometria nota per quantificare la distorsione del fluido in uscita causata da un profilo fluido in ingresso non uniforme. Durante una campagna di test la misura è stata ripetuta diverse volte per simulare l'ingestione del profilo non uniforme in differenti punti d'ingresso alla presa, caratteristico di differenti condizioni di volo.

I dati ottenuti rivelano la presenza di notevoli distorsioni, sia in termini geometrici che quantitativi, osservate in misure sia mediate nel tempo che non stazionarie. Il fluido è apparso altamente non stazionario, dimostrando chiaramente come i risultati ottenuti tramite misure stazionarie siano fuorvianti e non rappresentativi del vero comportamento di un fluido all'interno di una presa ad S. Elevate intensità sono state rilevate in generale, con picchi di valori in particolare nelle posizioni radiali più interne del condotto. Inoltre

i contorni della distorsione fluida si discostano in maniera consistente dalla classica configurazione a doppio vortice, con l'apparizione di multiple regioni vorticose.

Da tali misure si evince che la distorsione del fluido e le sue configurazioni in termini geometrici e di intensità dipendono dalla posizione di ingestione e dalla posizione radiale di misura. I risultati ottenuti permettono una maggiore comprensione dell'impatto del profilo di ingresso fluido sull'aerodinamica non stazionaria all'uscita di una presa ad S, e danno accesso ad ulteriori dati relativamente alla performance aerodinamica dei condotti ad S.

Parole chiave: profilo fluido non uniforme, presa ad S, S-PIV, distorsione fluida non stazionaria, distorsione vorticosa.

ACKNOWLEDGEMENTS

First of all, I would like to thank my Italian supervisor prof. Ernesto Benini for giving me the opportunity to study at Cranfield University. It has been an experience that has changed my life, enlarged my horizons and has allowed me to meet so many interesting people from all over the world. A second big thank you goes to prof. Pavlos Zachos. During the year spent working on the thesis he has given me great support, and the possibility to develop my technical and experimental skills. He has taught me with patience about particle image velocimetry and has allowed me to develop a thesis about a topic that few MSc students have the luck to work on. He is a great professor and a great person, it has been a pleasure to have him as a mentor.

A thank goes to PhDs Jésus Matesanz (#thanksforthecake) and Geoffrey Tanguy for the enlightening speeches, but a special one goes to Matteo Migliorini, that has been to me a second supervisor, a colleague and a friend at the same time. Thanks for the patience, the help and the good conversations (in italiano). Good luck with your PhD, and… do not give up on music!

A special mention is deserved by my boyfriend Alejandro Peñalver Mauri: Cranfield would not have been the same without you. Thank you for being such a special person. Thanks to the "new" friends in Cranfield, with whom I have shared a long, sometimes difficult year and to the "old" ones for the support and the love showed me.

Last but not least a huge, enormous "thank you!" goes to my family, without whom I would not be here, and I would not be graduating. Without my parents and my sisters I would not be the same person I am: I am lucky to have you all.

TABLE OF CONTENTS

LIST OF FIGURES

LIST OF TABLES

OPERATORS AND SUBSCRIPTS

$\langle . \rangle$	Time average
AIP	Evaluated at the AIP
amb	Relative to the ambient conditions
in	Evaluated at the inlet plane
max	Maximum value
mean	Area-averaged values
min	Minimum value
out	Evaluated at the outlet plane
ref	Evaluated at the reference plane
std	Standard deviation

LIST OF ABBREVIATIONS

AIP	Aerodynamic Interface Plane
BL	Boundary Layer
BLI	Boundary Layer Ingestion
BWB	Blended Wing Body
CFD	Computational Fluid Dynamics
EE	Embedded Engine
PDF	Probability Density Function
PIV	Particle Image Velocimetry
SAE	Society of Automotive Engineers
SD	Swirl Directivity
SI	Swirl Intensity
SM	Swirl Margin
SP	Swirl Pair
S-PIV	Stereo Particle Image Velocimetry
ΔPRS	Stability Pressure Ratio
ΔSM	Loss in Stability Margin

NOMENCLATURE

D	Diameter, *m*
h	Vertical offset of the S-duct centreline, *m*
L	Axial length of the S-duct, *m*
L_s	Length of the S-duct centreline, *m*
M_{ref}	Reference Mach number
MFR	Mass flow ratio
p	Static pressure, *Pa*
P	Total pressure, *Pa*
P_{bulk}	Probability of bulk swirl events, *%*
P_{twin}	Probability of twin swirl events, *%*
R	Radius of the S-duct cross-section, *m*
R_c	Curvature radius of the S-duct centreline arcs, *m*
Re_D	Reynolds number based on the cross-section diameter, $\rho_{ref} w_{ref} D/\mu$
SD_i	Swirl directivity at the *i-th* radius
SI_i	Swirl intensity at the *i-th* radius, *deg*
SP_i	Swirl pairs at the *i-th* radius
S_t	Strouhal number, $f D_{AIP}/\langle \overline{w} \rangle_{AIP}$
Δt	Time step of the laser beam, *s*
u, v, w	Cartesian velocity components, m/s
α	Swirl angle, *deg*
δ	Thickness of the boundary layer, *m*
θ	Rotation of the BLI location, *deg*
Ψ	Angular position along the arcs that define the S-duct centreline, *deg*
Ψ_c	Total angle of the arcs that define the S-duct centreline, *deg*

1 INTRODUCTION

1.1 Background

A great effort in the aviation industry has been done in the last decades to improve fuel efficiency and reduce pollutant emissions. Between 1960 and 2014, the average commercial aircraft fuel efficiency has approximately doubled [1]. This can be explained through many factors, among which improved materials, aircraft aerodynamics and engines. The critical requirements of size, compactness, noise, and intake performance of the last years have driven the industries towards new and different designs. Although further progress may be achieved in external aerodynamics and in systems and structures, the major improvements will probably be obtained in terms of new powerplant designs ad performances and their integration into the aircrafts [2].

In the last decades, the propulsion system integration has attracted attention in a variety of applications and configurations, such as distributed electric propulsion or boundary layer ingestion (BLI). The latter concept, of interest for this MSc work, consists in embedding the engine into the airframe. This allows the engine to ingest a portion of the airframe boundary layer, which decreases wake drag penalties. Following the tendency, a drive towards shorter and more complex intakes for advanced propulsion system installations has been recently developed. Such an interest has been noticed not only for civil, but also for military applications, where there is an increased demand for highly integrated engines. In such configurations, ducts with an “S” shape are required to connect the inlets to the aero engine intake systems. Compared to the jet engines, this kind of propulsors require less propulsive power inputs to produce the required amount of aircraft thrusts, leading to a considerable reduction in the amount of fuel that is consumed [3]. Consequently, a reduction in drag and weight is observed. However, the convoluted diffusing duct that supplies the air to the gas turbine engine generates notable unsteadiness which affects the performance of the engine, and in particular of the fan. Consequently, inlet flow distortion can be a critical design aspect for designs with unconventional intakes [4].

Flow distortion and flow separation are observed at the exit of the S-duct, in a plane conventionally referred to as Aerodynamic Interface Plane (AIP). Distortion can be

severe, and it can compromise the performance of the downstream turbomachinery. Some consequences can be: increased complex total pressure and swirl flow fields, vortical regions, unsteady flow perturbations that consistently affects the pressure rise, the compressor flow capacity and the surge margin. Regarding this last point, it has been observed that counter-rotating swirl in conjunction with total-pressure distortion can completely consume the surge margin of the compression system [5] [6] [4] [7]. From an industrial point of view, it is evident the need to consider swirl distributions during operability assessments in a large range of applications [7]. From previous work, it is clear that spatially and temporally rich and synchronous datasets are needed to accurately assess pressure and swirl distortions [8]. Different measurement techniques exist, and current industry practice relies on intrusive rakes with low spatial resolution. To approach this, both computational and experimental techniques have been previously used by the Cranfield research team. The work of Zachos et al. [4] is of particular relevance in the context, since it first performed and demonstrated the possibility to apply Stereoscopic Particle Image Velocimetry (S-PIV) at the full AIP of a convoluted intake. The results show that the S-PIV technique has a better spatial resolution than typical pressure measurements, since the latter underestimate the swirl distortion level. Despite S-PIV is a mature technique, no work exists with non-uniform flow profiles at the inlet of the S-duct. The indications are the inlet flow profile dictates the exit plane unsteadiness to a great extent. Moreover, the effects have never been quantified through the S-PIV method. The data acquired will give access to more reliable datasets about the aerodynamic performance of S-ducts and will educate the design process of new propulsion system integration of the engines.

1.2 Aim and objectives

The main aim of this work is to quantify the impact of the inlet flow profile on the unsteady aerodynamics at the exit plane of a previously studied S-duct intake using the S-PIV method.

The following objectives have been established to achieve the aim:

- Generation of the experiment and simulation of a non-uniform boundary layer through a 3D-printed distortion screen, placed upstream the S-duct intake. The distortion screen will have to provide the same boundary layer studied by Giuliani [9].
- Data acquisition through the Stereoscopic Particle Image Velocimetry technique applied at the Aerodynamic Interface Plane of 6 main cases, one with uniform boundary layer ingestion to be considered as a reference and five with non-uniform boundary layer ingestion. Distortion screen rotation of 45 degrees in each case to simulate the ingestion of boundary layer at different inlet locations, therefore representing cross-wind conditions. Flow conditions of $M_{ref} = 0.27$
- Processing and post-processing of the data and definition of a new processing tree.
- Quantification of the impact of the non-uniform flow field at the AIP in terms of the unsteady flow metrics and established distortion descriptors.
- Comparison of the results between the cases

2 LITERATURE REVIEW

2.1 BLI

Conventional or podded engines ingest clean, free stream flow at the cruise design point, and their propulsion system performance is well-known and can be adequately described with the typical parameters of weight, airframe drag, nacelle drag, and interference drag [10] . Despite this, the trend towards new propulsion systems integrated in the aircrafts has recently attracted a lot of attention. These new designs can be used in a variety of applications and configurations, such as distributed electric propulsion or boundary layer ingestion (BLI). In the latter case for example the engines are integrated into the airframe and are able to capture part of the airframe boundary layer, that is ingested by the propulsion system.

While in conventional engines the propulsion system design and its performance are often considered separately, for BLI systems this diversification is more difficult. New aircraft configurations with such a concept are being studied, and in general it is observed that the two systems require a closer coupling than the past.

The ingested boundary layer, passing through the propulsor, is exploited to improve the fuel efficiency of the engine, based on a re-energization of the aircraft energy. In this way, less kinetic energy is wasted and the aircraft requires less propulsive power inputs to produce the required amount of thrust, leading to a considerable reduction in the amount of fuel that is consumed and increasing the propulsive efficiency compared to a more traditional engine configuration [12] [13].

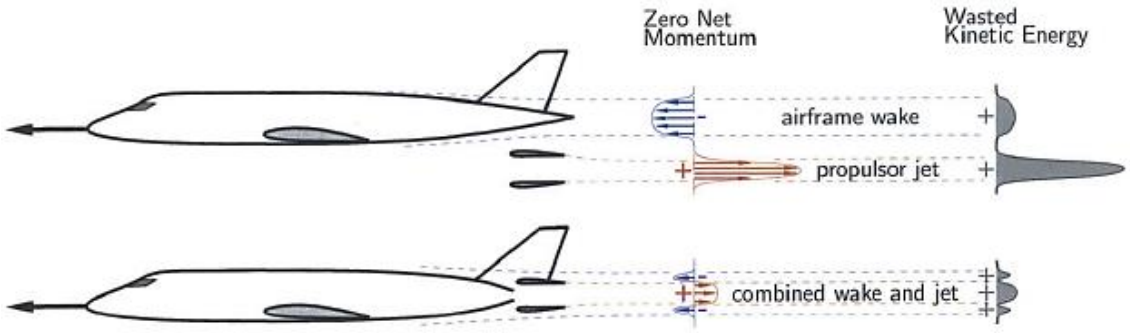

Figure 2-1: Boundary layer ingestion reduces wasted energy both in the wake of the airframe [13]**.**

Figure 2-1 illustrates the BLI concept, with a comparison between podded and BLI engines. In the upper aircraft, where no boundary layer is ingested, a balance between the airframe drag and the engine thrust is shown, that results in a zero-net momentum configuration in the downstream wake. In order words, the momentum deficit in the wake downstream the airplane is balanced by the excess of momentum in the propulsor jet. The kinetic energy in excess is lost as viscous dissipation, and it has to be taken into account for the calculation of the propulsive power necessary to produce thrust.

In the lower part of the Figure, an unconventional concept with BLI ingestion is represented. In this case, the drag produced by the airframe is partially ingested by the propulsor, and it manifests as a lower momentum fluid. This allows a reduction of the wake momentum deficit and the jet kinetic energy, resulting in a lower amount of required propulsive power and fuel burnt [3] [15].

Despite the several positive sides of the BLI concept, with such a technology the flow distortion at the inlet is observed to be at least one order of magnitude higher than in conventional aircrafts at cruise operation. High levels of flow distortions are not only connected to the upstream section of the inlet, but also with its downstream. BLI propulsion in fact often requires curved intakes to connect the inlets to the aero engine intake systems. These curved intakes are responsible for flow separations and swirling regions that highly affect the engine performance [15]. All these effects have to be taken into account while analysing and designing BLI propulsion systems [16], that are therefore complex technologies.

To sum up, novel concepts of propulsion that rely on boundary layer ingestion add complexity to the overall design, partially shifting the design challenge from the airframe to the propulsion system. High flow distortion is observed, and this affects the performance through aeromechanical, stability/operability, and acoustic issues in the downstream turbomachinery [17]. Moreover, because of these large flow distortions, a strong coupling between the fan and the upstream flow field is needed. With a BLI configuration a fan must withstand high levels of inlet flow distortion that create great difficulties for its design, with the need to avoid mechanical failure while maintaining thrust, efficiency and stability [18].

2.1.1 BLI effects in S-ducts

A parallel flow, but non-uniform in terms of density or velocity, obliged to follow a curved path generates a three-dimensional motion of the fluid flow [19]. Velocity components normal to the flow direction are observed, and a similar cross-flow generates a streamwise component known as vorticity or secondary flow. According to Greitzer et al. [19], considering a fluid moving through an incremental angle dθ, it is possible to define the streamwise component of the vorticity as:

$$\boldsymbol{\omega_s = -2\Delta\theta\omega_i} \quad \textbf{(2-1)}$$

Where Δθ is the bend angle along the duct and ω_i is the bend inlet vorticity.

If a duct with an S shape (Figure 2-2) is involved in the phenomenon, as studied by Greitzer [19], the viscous effects can generate an inlet flow vorticity that is responsible for the formation of secondary flows, even though the generation and evolution downstream the duct is mainly inviscid [19]. A generation of streamwise vorticity that points in the upstream direction can be observed in the initial part of the duct, as well as a secondary flow in the boundary layer region. This is indicated with $\Phi = 180°$ in Figure 2-3.

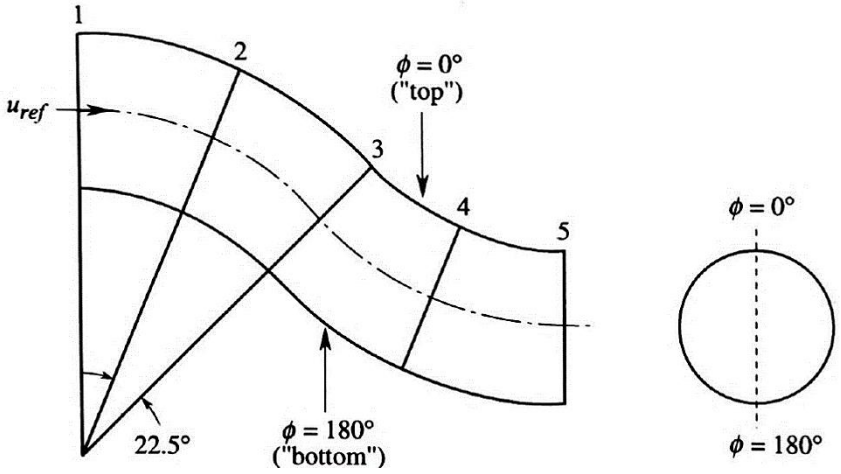

Figure 2-2: S-shaped duct [19]. Original picture from Bandson and Bradshaw, 1971.

Figure 2-3 also shows that a low-pressure region is observed in the lower part of the section area downstream the duct, whose thickness increases along the duct itself. This

distorted pattern results in a pair of counter-rotating vortices at the Aerodynamic Interface Plane, associated with the low stagnation pressure region depicted at the bottom of the Figure. Overall, it is observed that BLI in S-ducts is responsible of great levels of unsteadiness.

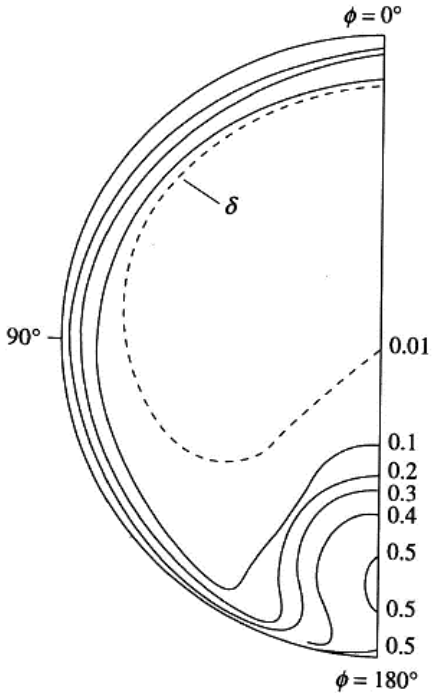

Figure 2-3: Stagnation pressure distortion at the exit of the S-duct [19]. Original picture from Bandson and Bradshaw, 1971.

High-resolution experimental measurements and full-annulus CFD calculations in S-ducts with BLI have been performed by E.J. Gunn and C.A. Hall [18] to further assess the phenomenon. The work shows the fluid dynamics and the loss sources associated to a BLI fan that is running at cruise conditions.

The presence of three main phenomena was observed:

- A three-dimensional flow redistribution, responsible of the attenuation of the axial velocity non-uniformities upstream the rotor and of non-uniform swirl and radial angle distributions at the rotor inlet.
- A distorted flow, characterised by a circumferential and radial variation in diffusion factors and a corresponding loss variation around the annulus.

- A localised peak at the rotor tip, responsible of an unsteady separation of the casing BL, while non-uniform swirl and radial angles at the rotor exit lead to possible variations in the profile loss and affect the corner separation size.

Moreover, BLI is found to be responsible also of great variations in rotor shock structure, strength and position, and of losses through the shock BL interaction.

Despite the several negative sides of the BLI technology, according to Plas, A. [12], "it is found that boundary layer ingestion can provide decreases in fuel burn of several per cent, ad that a promising avenue for mitigating the risks in BLI is to mix out the flow before it reaches the engine face". The benefits connected to BLI are function of many different elements. Some of them are: amount of BLI ingested, properties of the wake, engine cycles, inlet and turbomachinery losses connected to the distorted flow and airframe drag. [17]. According to Plas et al. [12] the ingestion of a reduced velocity air flow into the engine allows a reduction in the propulsion system ram drag, as well as weight and drag of the aircraft. Moreover, maximum propulsive efficiency benefits up to 28% are evidenced, as well as a net fuel burn reduction of 3-4% with modest levels of BLI (more or less 16% of the entire BL produced on the surface). The same benefits are described by Daggett et al., for whom a reduction up to 5.5% is reachable in the case of a blended wing body (BWB).

Overall, the section provides an overview of the boundary layer ingestion phenomenon, with both its positive and negative sides. From the overview, it is clear that a compromise to overcome the issues related to embedded engines is needed. In addition, good understanding of the boundary layer behaviour is fundamental if accurate designs are pursued.

2.2 Intake performance

Since the aim of this work is to study the impact of the ingestion of a non-uniform flow profile on the flow distortion at the exit of an S-duct, a greater understanding of inlets is necessary.

The main task for an engine intake is to transport the air mass flow required by the engine at the highest total pressure to the Aerodynamic Interface Plane (AIP), with as

little total pressure losses as possible [20]. This requires either acceleration or deceleration of the air flow inside the intake to match the flight conditions, depending on the flight Mach number [20]. Two main aspects are of great importance at the engine interface: one includes the delivery of the air with the highest total pressure and uniformity possible (both spatially and timewise) to ensure high trust levels and shaft power, as well as stable operations. The other deals with the compatibility aspect of the intake. Despite this, since intake designs are generally a compromise between various design aspects, ideal flight and propulsion conditions with respect to the efficiency and the flow uniformity are not generally achieved [20].

It has been seen in the previous section that intakes can suffer of flow distortion. This, known also as "intake distortion", could be a non-uniform distribution in total temperature, static pressure, total pressure, swirl or a combination of them. The total pressure distribution and swirl distortion are generally the most intense distortion parameters [20].

In case of high levels of distortion at the intake, notable unsteadiness could be generated. This greatly affects the performance of the engine and of the fan and results in increased complex total pressure and swirl flow fields, vortical regions, and unsteady flow perturbations, with a negative impact on the compressor flow capacity and surge margin [4], [5].

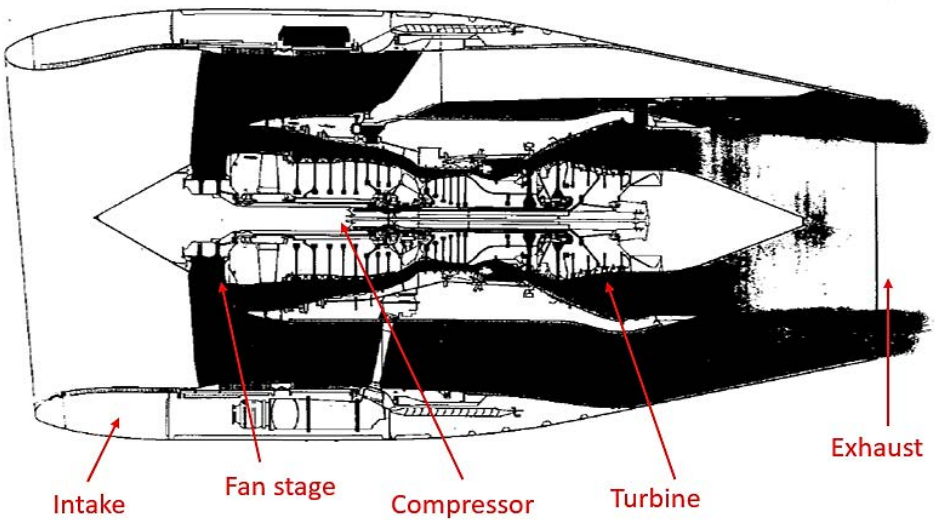

Figure 2-4: Podded engine, RB211-524L [10].

Although consistent experience in the design and building of engine intakes exists, the compatibility is hard to predict at the initial stage. The type, shape and position of an intake are in fact not only dependant on flow physics aspects, but also on the performance, the internal fuselage structure and the available space. In addition, today's requirements are very stringent and generally lead to compact and curved intake ducts, more prone to heavy flow separation and distortion. Therefore, understanding the sources of intake distortion and being able to quantify it through the distortion descriptors is of paramount importance.

Two main parameters are used to assess the intake performance:

1. The total pressure recovery, defined as

$$\eta = \frac{\bar{p}_{tAIP}}{p_{t0}} \tag{2-2}$$

that is the mean value of the total pressure at the AIP divided by the total pressure of the freestream flow.

2. The amount of the distortion, that is function of some distortion descriptors, that will be described later.

2.2.1 S-ducts

The stringent requirements of the last years about cost and weight are forcing the aircraft designs to move towards very compact intakes, increasing their exposure to distortion problems. Curved S-ducts, like the one shown in Figure 2-5, are prone to more heavy flow separations, whose magnitude depends upon the intake mass flow [15]. The change in the direction of the flow between the intake and the engine face tends to produce strong and complex swirl distortion, together with strong total pressure distortion at the engine entrance.

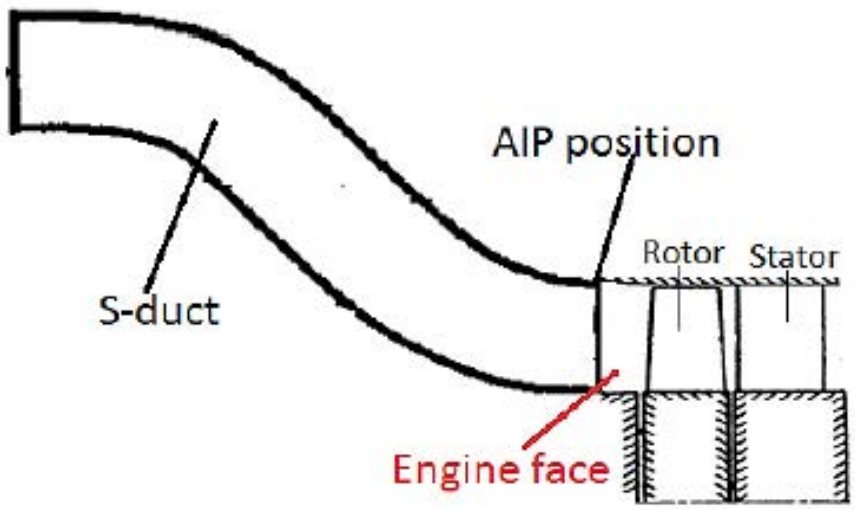

Figure 2-5: S-duct with AIP and engine face schematic [21].

Previous experimental work done at Cranfield University has clearly shown that high-offset duct generates greater levels of swirl distortion [4]. For example, the work of Zachos et al. [4] presents the study of the distortion at the Aerodynamic Interface Plane (AIP) of two S-ducts at different flow boundary conditions through the Stereoscopic Particle Image Velocimetry technique. The geometrical parameters of the two studied ducts are reported in Table 2-1, and for the aim of this work only the cases regarding an inlet flow Mach number of 0.27 are considered. Figure 2-6 shows the levels of distortion in the two ducts, and from the comparison it is evident that high-offset ducts suffer of greater flow distortions. Moreover, secondary flows are enhanced, and result in stronger swirl distortions [4].

Table 2-1: Design parameters for two different S-duct configurations [4].

Duct type	Offset-to-diameter ratio	Length-to-diameter ratio	Overall area ratio
Duct 1	H/D_{in}= 1.34	L/D_{in}= 5.0	$A_{out}/A_{in} = 1.52$
Duct 2	H/D_{in}= 2.44	L/D_{in}= 4.95	$A_{out}/A_{in} = 1.52$

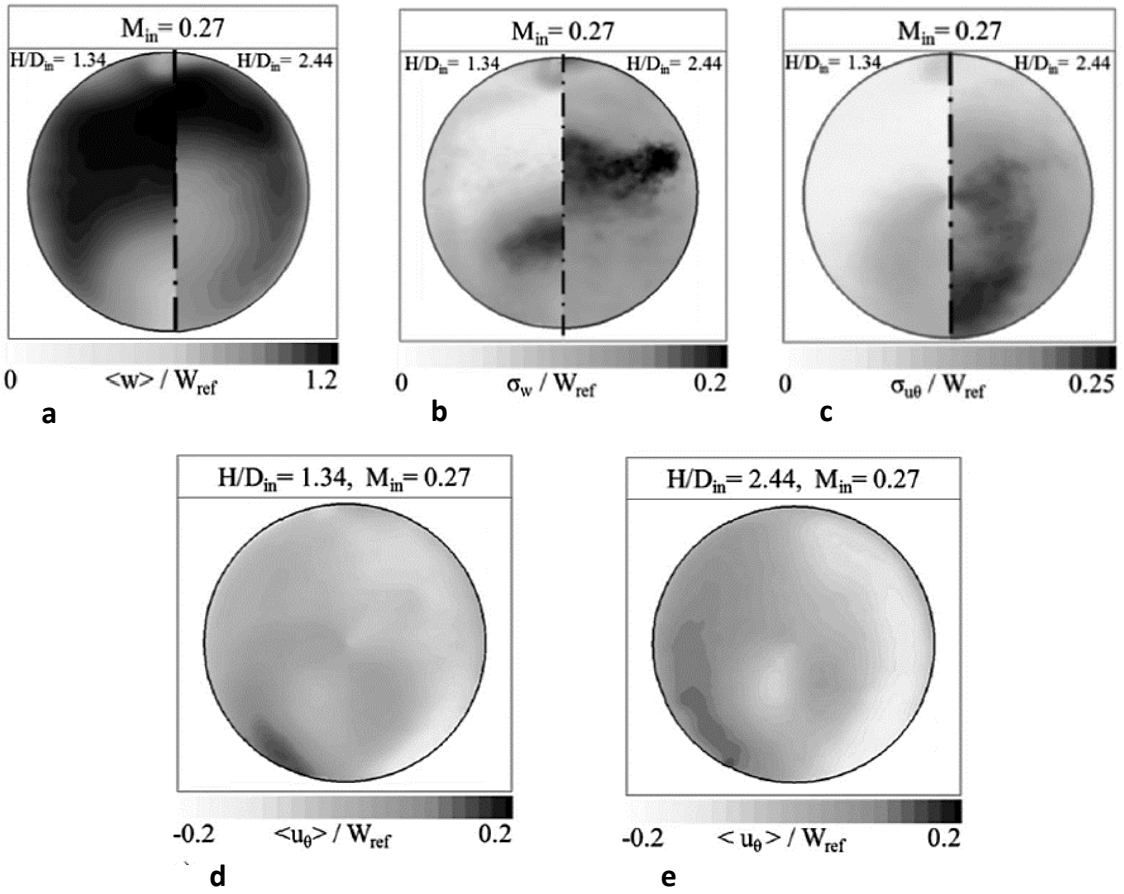

Figure 2-6: Comparison of the results at the AIP between the two S-duct configurations. a) Nondimensional time-averaged out-of-plane velocity, b) Nondimensional out-of-plane velocity fluctuation, c) Nondimensional circumferential velocity fluctuation, d) Nondimensional time-averaged cicumferential velocity in the low-offset duct e) Nondimensional time-averaged cicumferential velocity in the high-offset duct [4].

2.2.2 Aerodynamic Interface Plane (AIP)

In the study of intake distortions and flow behaviour inside an S-duct, the Aerodynamic Interface Plane (AIP) is of paramount importance. The AIP is an engine entry plane, arbitrarily located between the intake exit plane and the engine, used to define distortion and performance at the interface between the two parts. This plane is generally kept invariant through the test cycles of the propulsion system.

Society of Automotive Engineers [22] provides some guidelines for the definition of the AIP location:

- The AIP should be located along the duct, in a circular or annular section.
- The AIP should be located as near as possible to the fan/engine face, defined by the first blade row.
- The AIP should be invested by the entire engine airflow, and only by it. Its distance with the auxiliary air systems should be such that the measurements carried at the AIP include the distortion caused by the auxiliary air systems.
- The location of the AIP should be such that the interface instrumentation does not interfere with the engine performance and stability.

2.3 Flow Distortion

So far it has been seen that embedded engines, together with coreless fans in turbo-electric distribution propulsion architectures, are susceptible to intake flow separation and flow distortion [6]. Inlet distortion can be particularly severe for unconventional intakes, and it has to be taken into account in the design phase. Convoluted aeroengine intakes generate unsteady flow fields that are sources of instabilities, and can greatly affect the performance of the downstream turbomachinery [4].

Within the intake's curve, flow separations could generate total pressure and swirl distortions. This may result in low-momentum flow regions or swirling, with contra or co-rotating flow with respect to the compression system. Obviously, this affects the incidence angle of the flow onto the blade. The flow separation in the first bend of the S-

duct interacts with the associated secondary flows, generating two vortical structures at the Aerodynamic Interface Plane, and large unsteady flow perturbations that affect the pressure rise, the flow capacity and the surge margin of the compression system [4], [8].

2.4 Types of distortion

The main types of uniformities that can be found at the AIP are about total pressure, static pressure, total temperature and swirl distortion. Among them, total pressure and swirl distortion are the most important distortion parameters. Static pressure distortion results from vortices entering the intake, that mainly depend on the engine mass flow. Therefore, it can be partially prevented by engine handling procedures [23]. Total pressure distortion is instead caused by flow separation and wakes, and intake lip and/or separations in the sidewall region are particularly frequent in thin and drag optimized shapes. The phenomenon is present especially in agile aircrafts, with envelopes that experience high angles of attack.

2.4.1 Previous work

As previously mentioned, the presence of total-pressure and swirl distortion at the AIP greatly affects the performance of the compression system, lowering the surge margin and increasing the possibility of stall inception [7], [8].

Figure 2-7 shows simulated time-averaged total pressure and swirl angle distributions across the AIP, as an example of the flow uniformities that can be found at the Aerodynamic Interface Plane [24]. In the simulation performed by Chiereghin, N. et al. [24], a steady Reynold-averaged Navier-Stockes method was used on a S-duct. The geometrical parameters of the duct are an area ratio of $\frac{\mathrm{A_{in}}}{\mathrm{A_{out}}}$ = 1.52, a vertical offset-to-inlet diameter ratio of $\frac{H}{D_{in}}$ = 1.34, and a length-to-inlet diameter ratio of $\frac{L}{D_{in}} = 5.0$. The experiment highlighted that the flow inside curved ducts is subjected to flow separation and distortion (Figure 2-7a). In-plane secondary vortices are therefore enhanced, and vortical regions characterised by a twin swirl pattern are observed at the S-duct exit, with quite high swirl angles (Figure 2-7b, Figure 2-7c) that result in total pressure distortion profiles such as the one shown in Figure 2-7d.

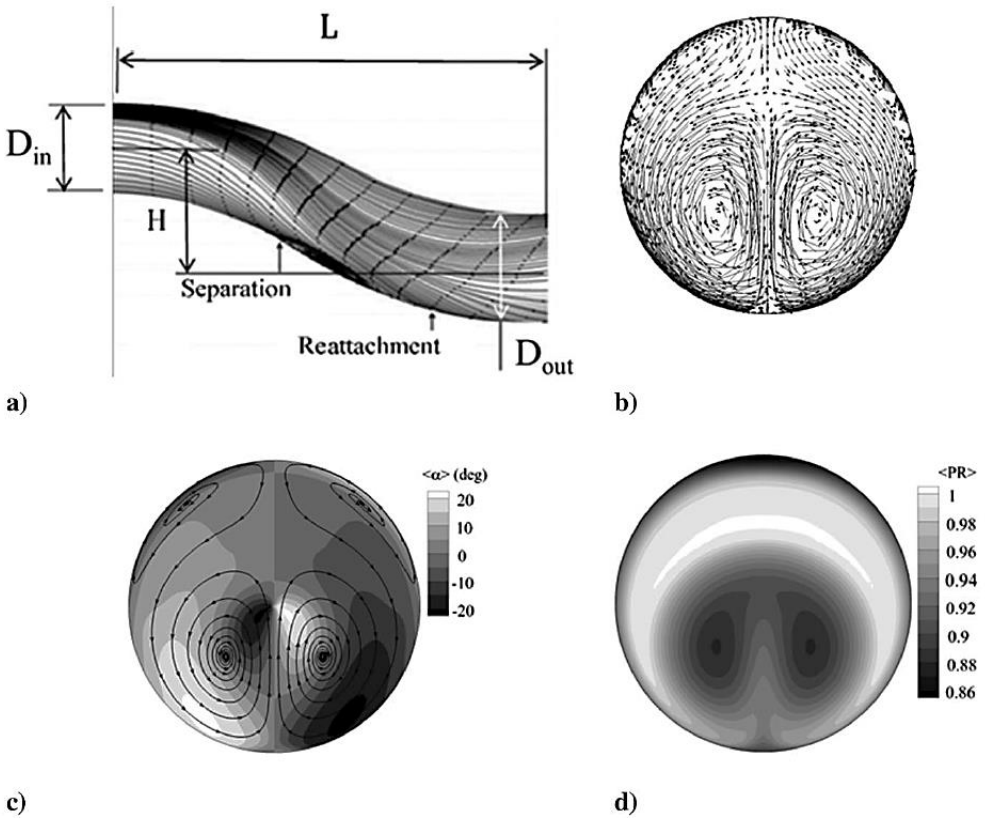

Figure 2-7: Example of S-Duct flow fields and flow non-uniformities at the AIP. a) streaklines, b) velocity vectors, c) swirl angle, and d) total-pressure ratio at AIP [4], [24].

The same results were previously obtained by Wellborn et al. [25] for the same duct configuration.

It is known that the presence of a co-rotating swirl slightly decreases the stability margin compared to the total pressure distortion alone. However, in an S-duct both pressure distortion and swirl distortion are present: the combination of the two effects can consume the stability margin consistently [7]. Swirl is related to vortices and secondary flows, and it affects the incidence angle of the flow onto the compressor blade with the risk of unexpected stall [26]. In the work of Meyer et al. [27] twin vortices were generated through a delta wing with a variable angle of attack. It was observed that an increase in the average vortex swirl angle was the responsible of a major loss of surge margin. An average swirl angle of 13 deg. was in fact observed to cause a reduction of 16% in the surge margin, as well as a reduction of 7% of compressor efficiency.

Despite large part of the measurements are taken for steady-state flows, unsteady aspects of the flows are also important, and need to be considered. Previous work underlined in fact that the engine stall can be a consequence of distortion fluctuations. Moreover, studies on dynamic distortions insisted on the importance of instantaneous distortion and, in particular, on the local peak values [26]. In the work of Zachos et al. [4], Stereo Particle Image Velocimetry (SPIV) was applied for the first time to measure the unsteady, three-component velocity field at the AIP, with approximately 250 times more data points compared with conventional experimental techniques based on 40 pressure transducers. The results presented important advancements in the methods used to quantify distorted flow fields in complex intakes.

It is evident that the minimization of the distortion is one of the design drivers for embedded engines, in order to decrease its effect in the engine stability and operation. All the previous works reported above underline that spatially and synchronous measurements techniques are needed to be able to better assess the unsteady nature of the total pressure and swirl distortion.

Despite this, industry practice still mainly relies on low-spatial resolution rakes, that are intrusive and unable to capture the complex nature of the flows with a good spatial and temporal resolution.

2.4.2 Swirl distortion

Swirl is defined as the portion of the flow directed circumferentially at the engine face. Axial flow therefore has zero swirl. Past experience shows that swirl-distortion can be observed during ground and flight conditions and can be originated by a number of sources. Consequently, a variety of swirl characteristics is expected. Despite inlet swirls have been grouped in dozen different categories, four fundamental categories are identified, based on swirl patterns [7]. According to SAE, these are:

(1) Bulk swirl
(2) Paired swirl
(3) Tightly-wound vortices
(4) Cross-flow-swirl

The last two swirl types are of no interest for this work, since they form in short and straight inlet ducts, during operations on ground or in lift fan configurations [7]. Furthermore, paired swirl can be divided in one-per-revolution and two-per revolution paired patterns, as depicted in Figure 2-8 [28]. Bulk swirl consists in a flow that is all rotating in the same or opposite direction of the compressor rotation. Paired swirl instead consists in two or more paired vortices that rotate in opposite directions, that can be either twin swirls or have different magnitudes. The swirl pattern is a sinusoidal wave when plotted at constant radius.

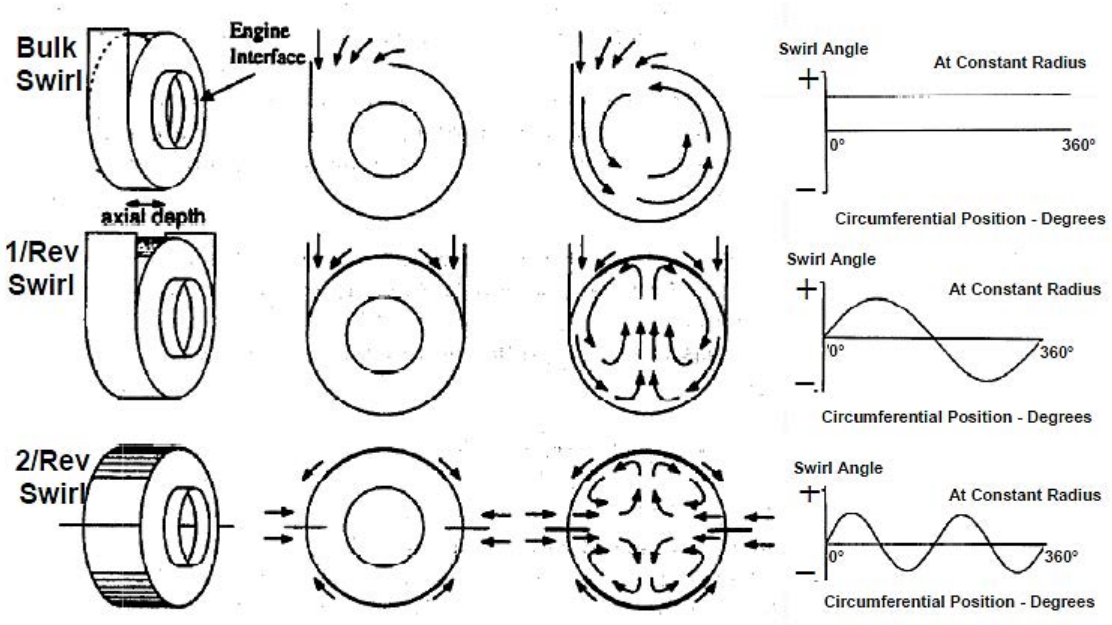

Figure 2-8: Common swirl distortion patterns [28]**.**

If the flow is contra-rotating, it can reduce the stability level of the engine [20]. In addition, if it is combined with total pressure distortion, the engine can be more unstable than in case of total pressure distortion alone [20]. In general, the engine sensitivity is linked to the bulk swirl at a constant tip radius. At the moment, swirl is considered to be steady-state, and almost no literature exists about dynamic swirl investigations [20] .

Different inlet configurations generate different types of swirl, that are described in terms of the swirl angle α.

The swirl angle α is defined as:

$$\alpha = \tan^{-1}(\frac{U_\theta}{U_x}) \quad \textbf{(2-3)}$$

And as already mentioned it is the circumferential angle of flow from the axial direction at a point (Figure 2-9).

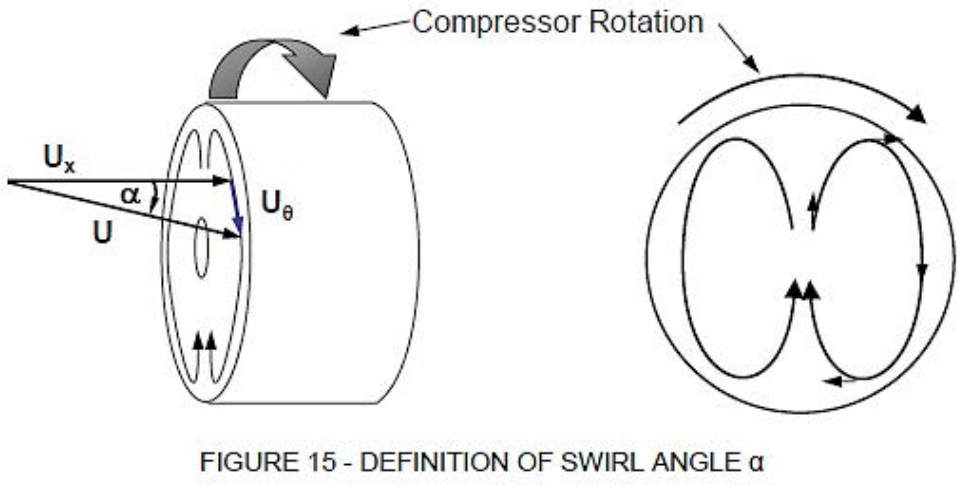

Figure 2-9: Swirl angle definition [7].

Bulk swirl

Swirl is referred to as bulk swirl when the flow enters the compressor with the entire flow field rotating in one direction with respect to the rotational axis of the compressor. If the flow and the compressor rotate in the same direction, the swirl is known as co-rotating bulk swirl. If their rotation is opposite, the swirl is known as counter-rotating bulk swirl. Generally, bulk swirl can be external or internal, and it can be generated through different and numerous mechanisms (use of inlet guide vanes, by a scrolled duct that leads to the compressor, etc.). The internal distortions are usually a result of the geometry of the air-induction system and the conditions of the flow at the inlet.

In S-ducts, bulk swirl can originate when the flow at the inlet has a non-axisymmetric total-pressure gradient normal to the plane of the turn, that interacts with the static-pressure gradient of the bended flow inside the duct. The total-pressure gradient responsible of the origin of S-duct bulk swirl is a consequence of the inlet flow separation.

The presence of vorticity associated with the pressure gradient normal to the plane of the turn is a necessary condition too.

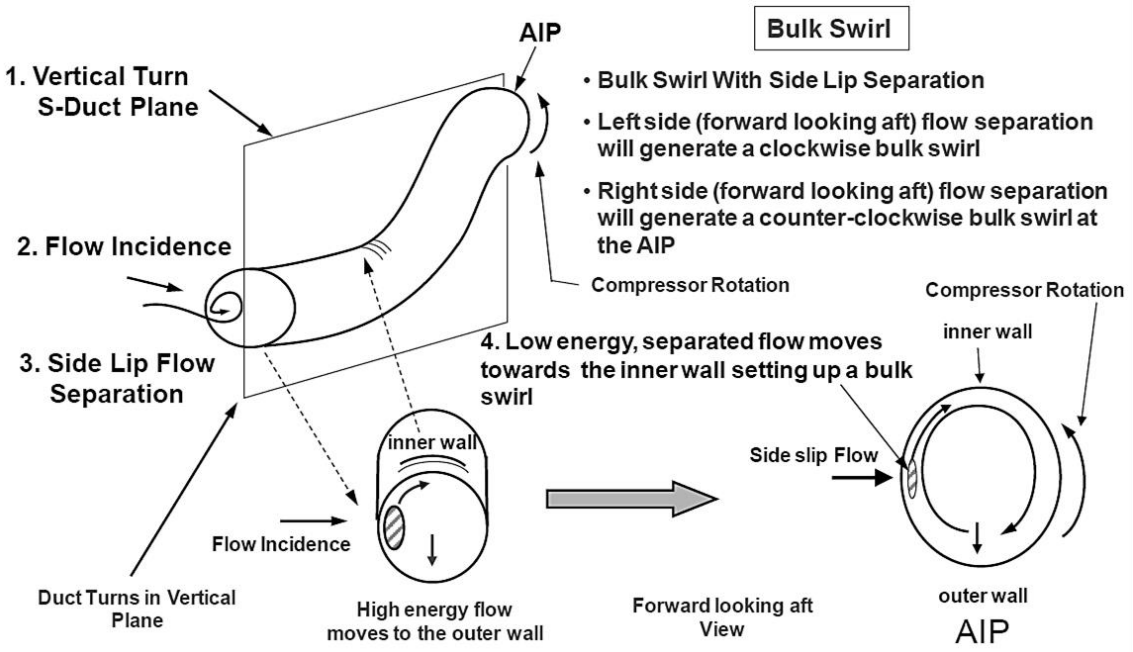

Figure 2-10: Example of bulk swirl patterns generated in a S-duct [7].

Figure 2-10 shows a schematic of a vertical S-duct in sideslip. Sideslip separation is responsible of the creation of a low-pressure region, that induces the low-energy flow to move circumferentially towards the inside radius of the duct turn. This flow movement initiates a clockwise bulk swirl (looking forward aft), as shown in the bottom right of the Figure. Likewise, a counter-clockwise bulk swirl would be the consequence of a sideslip in the opposite direction. For this reason, depending on the direction of rotation of the engine, one of the sideslips would be the responsible of the stability margin reduction, generating a counter/rotating bulk swirl.

Paired Swirl

It is the most common type of swirl, and in S-ducts it is usually connected to the presence of vorticity or pressure-gradients. If there are two vortices with equal magnitude and opposite direction, these are known as twin swirl (Figure 2-11). However, the vortices might not have the same magnitude, and one or more vortices can dominate the others [28]. If the magnitude of the two vortices is different, that happens when the BL at the

inlet is not symmetric, their pattern is called offset or non-symmetrical swirl pair, and it is shown in Figure 2-12.

The paired swirl pattern is more likely to be generated by the presence of curves in the duct or complex shapes.

As a consequence of vorticity, paired swirl is a flow containing vorticity normal to the flow direction enters the duct inlet. Because of the S-duct shape, the flow is turned out of the vorticity plane. Figure 2-11 and Figure 2-12 show the concept. The vorticity vector (1) at the inlet, caused by the velocity gradient in the wall (presence of boundary layer), is turned by the duct-turning vector (2) that is normal to it. This interaction is responsible of the flow rotation, depicted with the number three. As shown at the duct outlet, two counterrotating vortexes on the two sides of the duct are created. The flow vortexes rotate from the outside to the inner side of the turns, creating two paired swirls. If the magnitude of the opposite rotating vortices is equal, they are twin swirl. These swirls are characterized by zero circumferential average around the annulus [7].

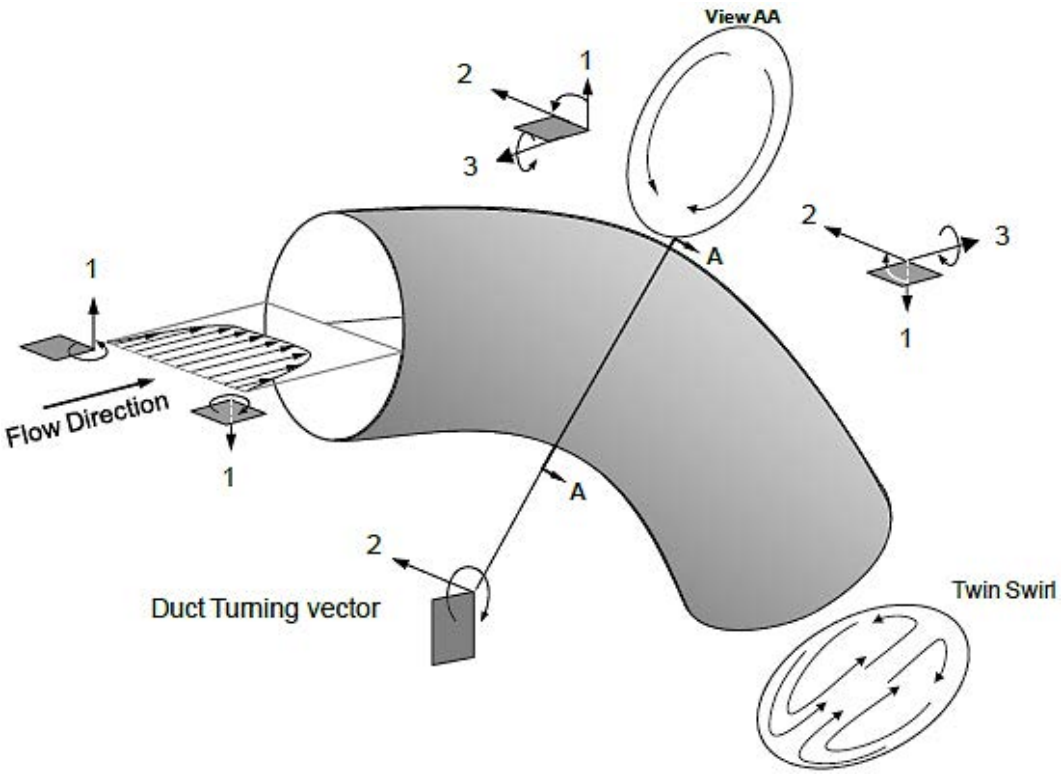

Figure 2-11: Paired Swirl formation at the exit of an S-duct [7].

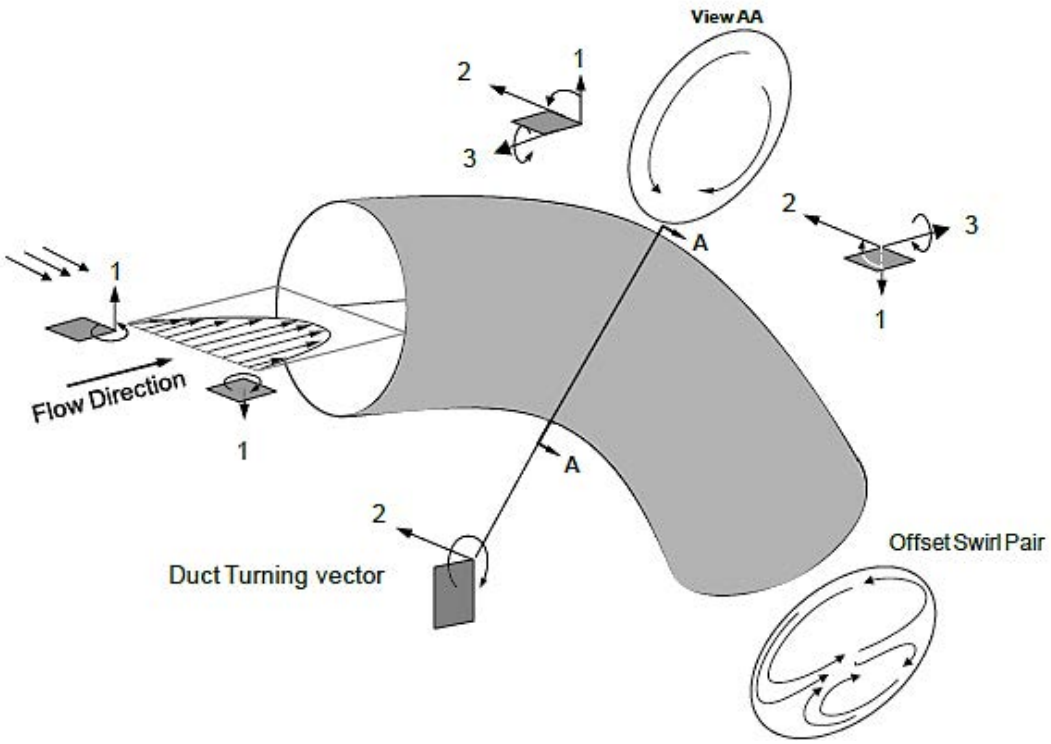

Figure 2-12: Offset swirl pair, consequence of a non-symmetric flow at the S-duct entrance [7].

As previously said, paired swirl can also be a consequence of pressure-gradients and momentum. D.S. Miller [29] explains the concept (Figure 2-13). An ideal flow with uniform energy distribution passes through a bend (A). The static pressure is observed to increase with the turn radius to balance the centrifugal forces towards the outer wall, while the velocity decreases. Conversely, the velocity increases as the static pressure lowers in the inner wall.

Momentum distribution is involved, since the velocity varies from zero (at the wall) to its maximum value at the core. Where the velocity is higher, centrifugal and pressure forces deflect the core towards the outer part of the bend. As a consequence, the fluid that is approaching this outer region has to face the adverse pressure gradient described in the upper part of Figure 2-13 (case A). The fluid, not able to pass through the adverse pressure-gradient, is obliged to move around the wall and towards the inner part of the bend. This movement, together with the core deflection of the high velocity region, causes the formation of two vortices, as shown in the bottom part of Figure 2-13 (case B).

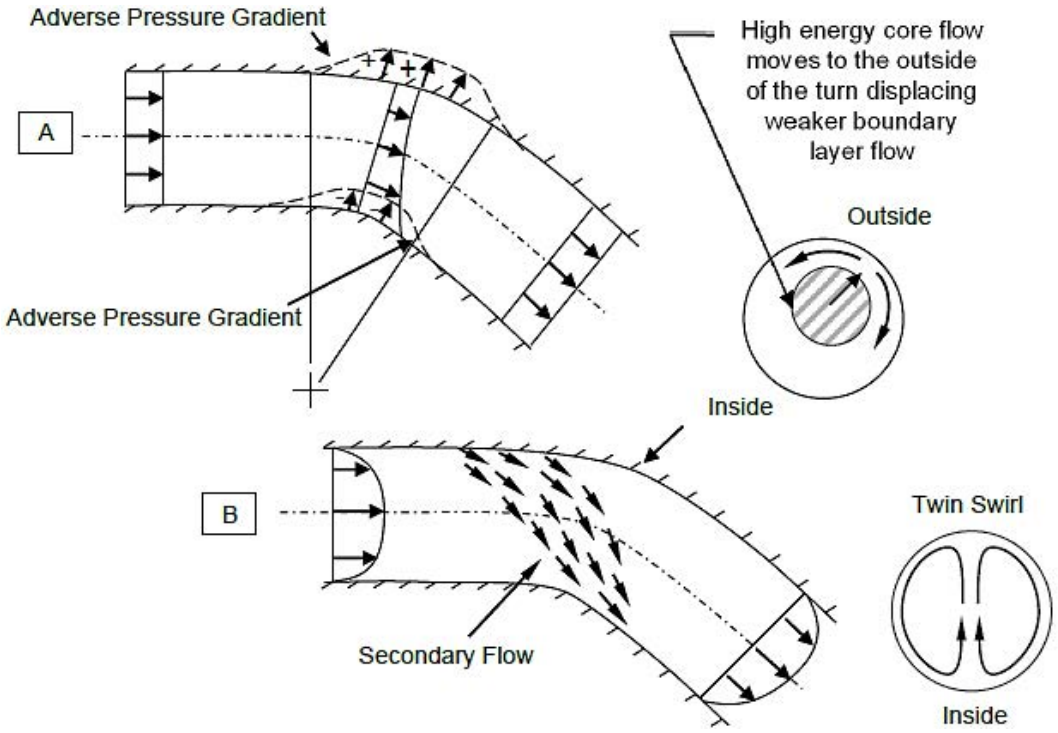

Figure 2-13: Paired Swirl formation [29]**.**

Finally, paired swirl can be classified as one-per-rev or single paired, if the fluid flows through a single turn. It is defined as two-per-rev or two swirl pairs if the flow passes through two turns. The difference between the two is shown in Figure 2-14.

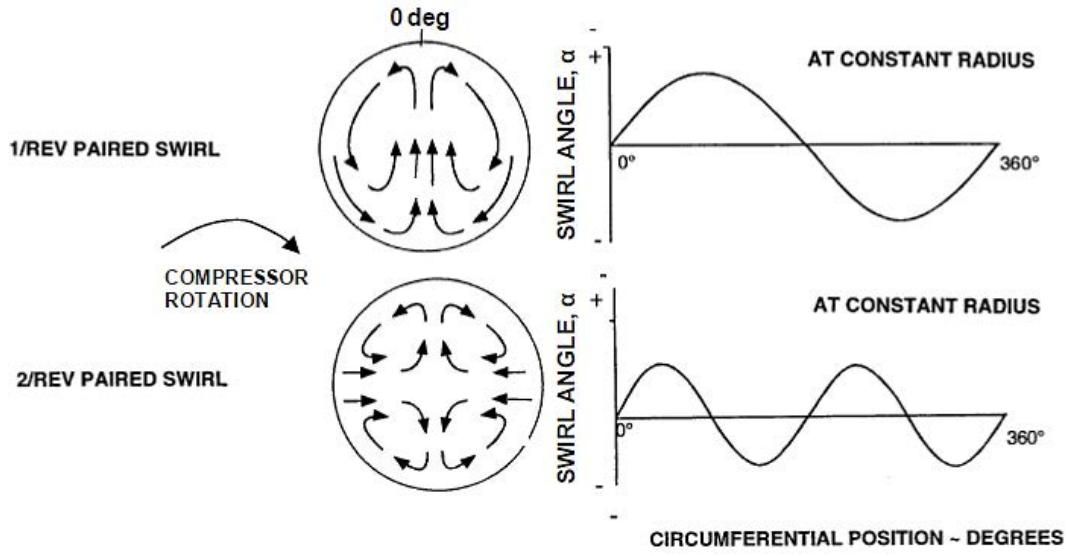

Figure 2-14: Difference between 1/rev and 2/rev paired swirls [7].

2.4.3 Effects of Bulk Swirl on Compression Systems

Distortion, and so swirl, has a negative influence on the compression system. The impact of swirl onto the rotor blade can be studied through its incidence angle at constant axial velocity [7]. The incidence angle is defined as the angle between the blade chord line and the vector of the upstream flow relative to the blade. In case of a counter-rotating bulk swirl with respect to the rotation of the rotor there is an increase in incidence, thus higher loading on the blade row and reduced margin stability. On the contrary, with a co-rotating bulk swirl the incidence is reduced, and the stability margin is increased. The positive and negative swirl rotations are defined with respect to the compressor rotation, for simplicity. They are used to assess the performance and the stability of the compressor; the swirl incidence is important to determine the effect into the compressor performance. Therefore, a co-rotating swirl is defined as positive, and a counter-rotating swirl with respect to the compressor rotation direction is defined as negative. Co-rotating swirl usually have a positive effect on compressor performance since it reduces the flow impacting the compressor and the pressure ratio and increases the efficiency and the stall margin. On the other hand, counter-rotating swirl increases the flow and the pressure ratio, contributing in reducing the compressor efficiency and the stall margin, with risk for the engine to surge [28]. The concept is shown in Figure 2-15.

Figure 2-16 shows the response of a compressor or a fan to an axisymmetric swirl at the inlet. for a given inlet swirl the compressor adjusts the flow to meet the exit throttle settings, as depicted in the figure. A counter-rotating bulk swirl will cause the fixed speed line to move towards higher pressure ratios and flow, and to lower stability boundary. On the opposite, a co-rotating swirl will move the fixed speed line to lower values of flow and pressure ratios, and the stability to higher values.

Measurements of combined total pressure and swirl distortion are usually carried out by means of intrusive probes and rakes. This provides values at different circumferential locations at different radial location at the AIP. In general, at least two radial locations are required to define swirl at the hub and tip of a compressor fan [28].

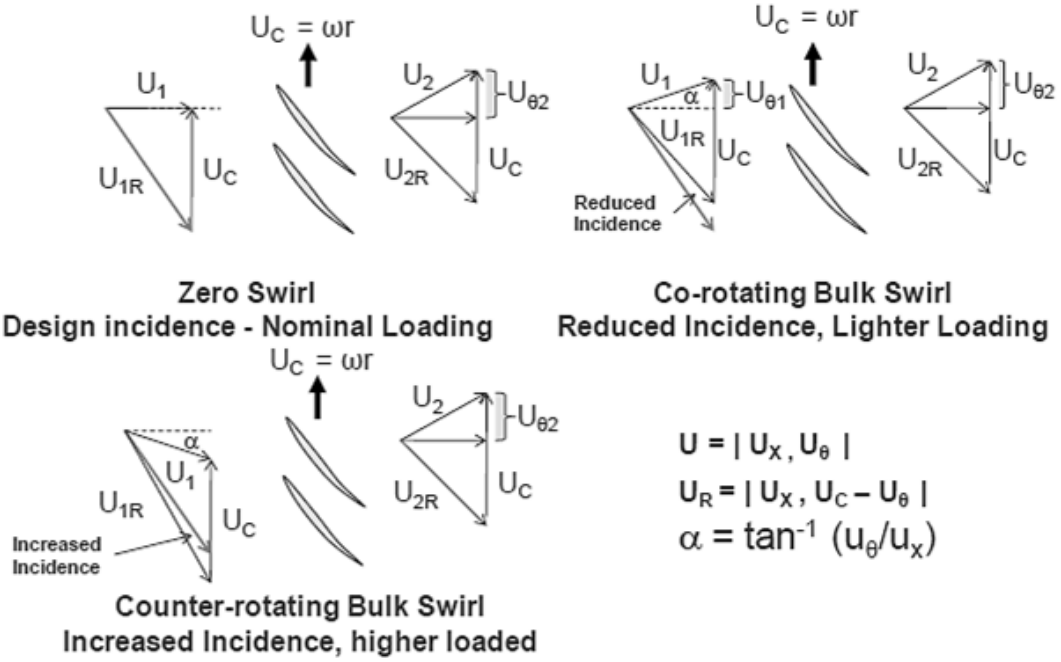

Figure 2-15: Incidence angle of bulk swirls on rotor blades at constant axial velocity [7].

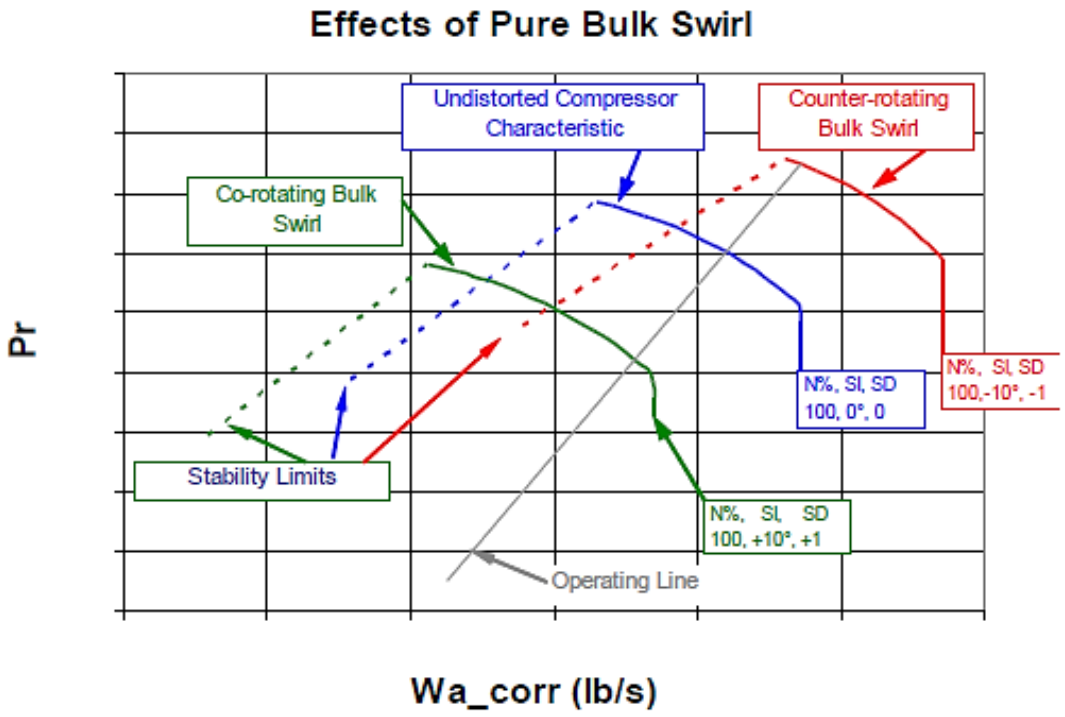

Figure 2-16: Effect of bulk swirl on compression system performance [7].

2.5 Swirl descriptors

Swirl descriptors correlate the swirl distortion with the characteristics of operability of the fan or the compressor [7]. With them, comparison between difference engine systems are possible. Swirl descriptors are: Sector Swirl (SS), Swirl Intensity (SI), Swirl Directivity (SD) and Swirl Pairs (SP). They require three elements to be able to completely define the swirl at the engine face: the intensity of the swirl, its direction and its pattern. Swirl Intensity (SI) describes the magnitude of the predominant swirl angle, expressed in degrees; Swirl Directivity (SD), that varies between -1 and 1, captures the rotational direction with respect to the compressor rotation direction of the predominant swirl intensity. A +1 value indicates a co-rotating pure bulk swirl with an average incidence angle of SI degrees. 0 indicates a symmetrical multiple per revolution swirl; a SD value of -1 indicates instead a counter-rotation bulk swirl with and angle of SI degrees of incidence. The third swirl descriptor considered in this work is the Swirl Pairs (SP), also known as Multiple-Per-Revolution parameter (SMPR), that indicates the number of pairs of positive and negative swirl direction changes [28]. Finally Sector Swirl (SS), which is defined at a specific radial sector, gives the value of the average positive swirl content (co-rotating) and negative content (counter-rotating) of the distortion.

Unlike pressure-distortion descriptors, swirl descriptors are defined only for steady-state swirl conditions. They are defined from swirl-angle experimental data that have been obtained at the Aerodynamic Interface Plane, and are relative to the direction of the engine rotation [7]. The swirl intensity, directivity and multiple-per-revolution elements are obtained through a linear interpolation of the swirl, in a given ring. In the following paragraph, the definitions of the main swirl distortion descriptors are first introduced for the one-per-rev pattern, and subsequently they are extended to a more generic multiple-per-rev concept. The analysed descriptors will allow to describe any type of swirl induced by different and various types of inlets, and to model the swirl effects on the compressor performance [28]. Moreover, one of their most important attributes is that they can be easily combined with the industrial standard total pressure distortion descriptors [28].

2.5.1 Swirl distortion elements for bulk or one-per-rev patterns

Figure 2-17 shows a paired swirl pattern measured on a i-th instrumentation ring for a complete 360° revolution at the AIP. θ_i^+ indicates the circumferential extent of the co-rotating (positive) swirl region, while θ_i^- indicates the circumferential extent of the counter-rotating (negative) swirl region. The region extent is defined by the intersection of the zero-swirl axis with the connecting line that joints the points, that indicate a change from positive to negative swirl angles or vice versa. In the Figure, swirl changes direction at three circumferential locations: $\theta 1_i = 0°$, $\theta 2_i = 180°$, and $\theta 3_i = 360°$. Therefore:

- $\theta_i^+ = \theta 2_i - \theta 1_i$ defines the "theta plus" extent
- $\theta_i^- = \theta 3_i - \theta 2_i$ defines the "theta minus" extent

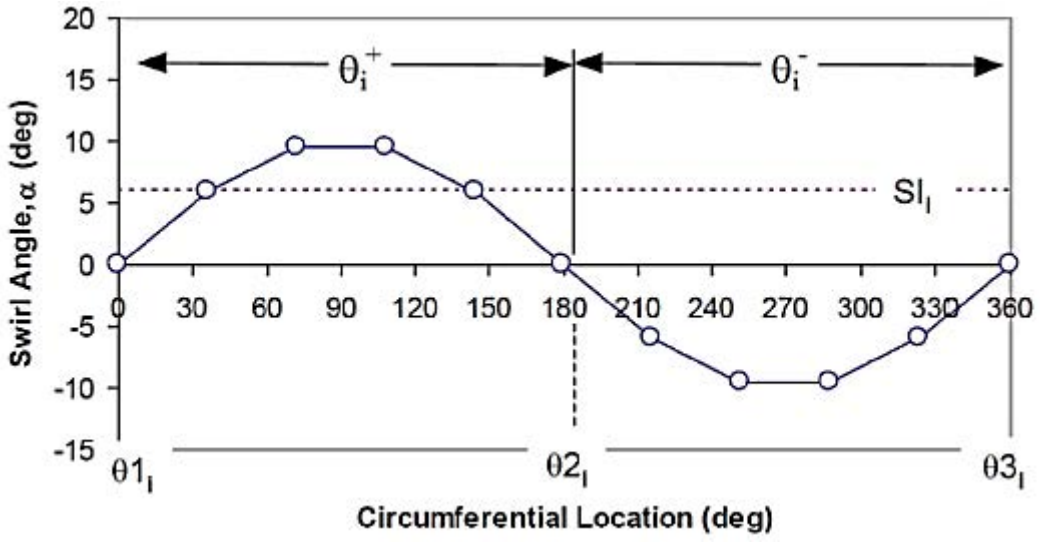

Figure 2-17: One per-rev symmetric swirl pattern [7].

2.5.1.1 Sector Swirl (SS)

It integrates the swirl angle over the positive/negative θ_i extent, therefore quantifies the amount of average negative (SS_i^-) and positive (SS_i^+) swirl at a given radial ring. It is defined as:

$$SS_i^{+/-} = \frac{1}{\theta_1^{+/-}} \int_{\theta_i^{+/-}} \alpha(\theta)_i d\theta \qquad \textbf{(2-4)}$$

where $\alpha(\theta)_i$ is the swirl-angle, function of the circumferential location.

2.5.1.2 Swirl Intensity (SI)

It is an average of the circumferential swirl angles expressed in degrees, also defined as the "extent" weighted absolute swirl [28]. This for each ring and at the AIP.

$$SI_i = \frac{SS_i^+ * \theta_i^+ + |SS_i^-| * \theta_i^-}{360} \quad \textbf{(2-5)}$$

2.5.1.3 Swirl Directivity (SD)

It indicates the direction of the distortion due to the swirl, with respect to the rotation of the compressor. Its value is in the range of +/-1.

$$SD_i = \frac{SS_i^+ x * + SS_i^- * \theta_i^-}{SS_i^+ * \theta_i^+ + |SS_i^-| * \theta_i^-} \quad \textbf{(2-6)}$$

In case of a sinusoidal distribution the Swirl Directivity is zero, since in one revolution there is only an equal and opposite swirl. If SS_i^- or SS_i^+ are zero, in the case of a co-rotating or a counter-rotating swirl respectively, the Swirl Directivity is one.

A spectrum of patterns is shown in Figure 2-18:

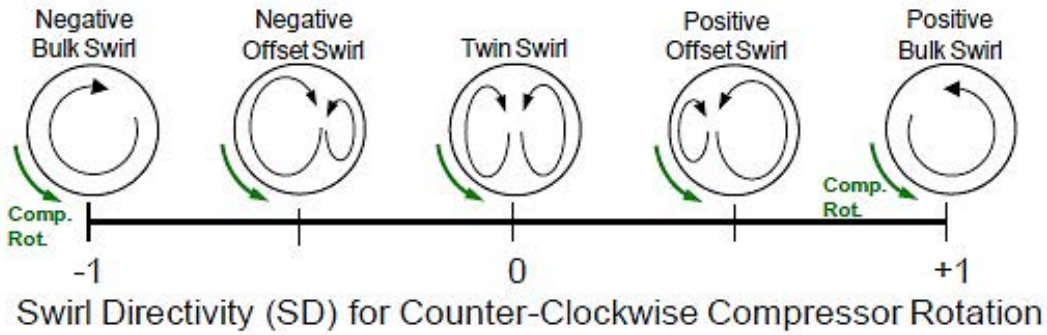

Figure 2-18: Swirl Directivity spectrum [7].

2.5.1.4 Swirl Pairs (SP)

It indicates the pairs number of positive and negative swirl changes in direction in the measured swirl, at the given i-th ring.

$$SP_i = \frac{SS_i^+ * \theta_i^+ + |SS_i^-| * \theta_i^-}{2 * Max\ of\ \{[SS_i^+ * \theta_i^+] or [|SS_i^-| * \theta_i^-]\}} \quad \textbf{(2-7)}$$

It can be described also as the range between one-per-rev swirl and bulk-pattern swirl.

These swirl descriptors can also be used to describe bulk swirls. In a pure bulk swirl, the swirl angle α(θ) is constant along the ring. In an offset bulk swirl instead the swirl angle may vary, remaining either positive or negative for a full revolution, and SS_i^- and SS_i^+ may go to zero. In this case SI_i becomes the average ring bulk swirl angle, and the swirl directivity SD_i assumes a value of +1 or -1 (for co-rotating or counter-rotating swirl). The swirl pairs is 0.5 for any type of pure or offset bulk swirl. Figure 2-19 shows a spectrum of patterns for the Swirl Pairs.

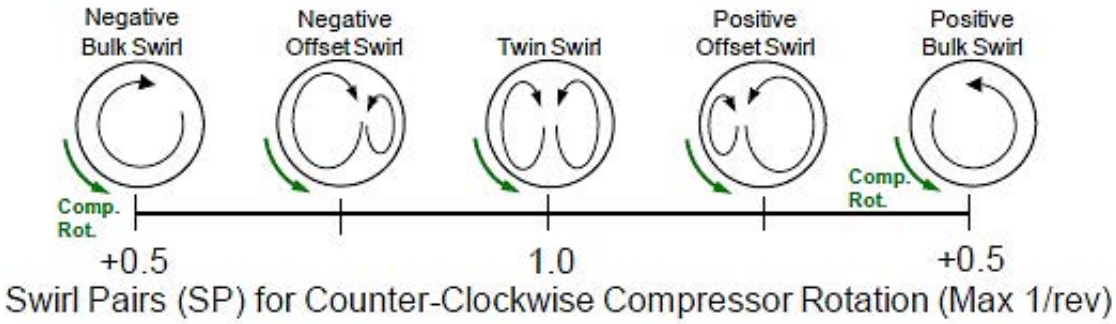

Figure 2-19: Swirl Pairs (SP) spectrum [7].

2.5.2 Swirl distortion descriptors for multiple-per-rev patterns

The definitions of the main descriptors described above will here be extended to characterize swirl distortion with a multiple-per-rev pattern, measured on a given i-th ring. Pairs of positive to negative adjacent regions are indicated as *k* swirl patterns. Two pairs of "theta-plus" and "theta-minus" areas are identified in Figure 2-20, indicated with k=1 and k=2.

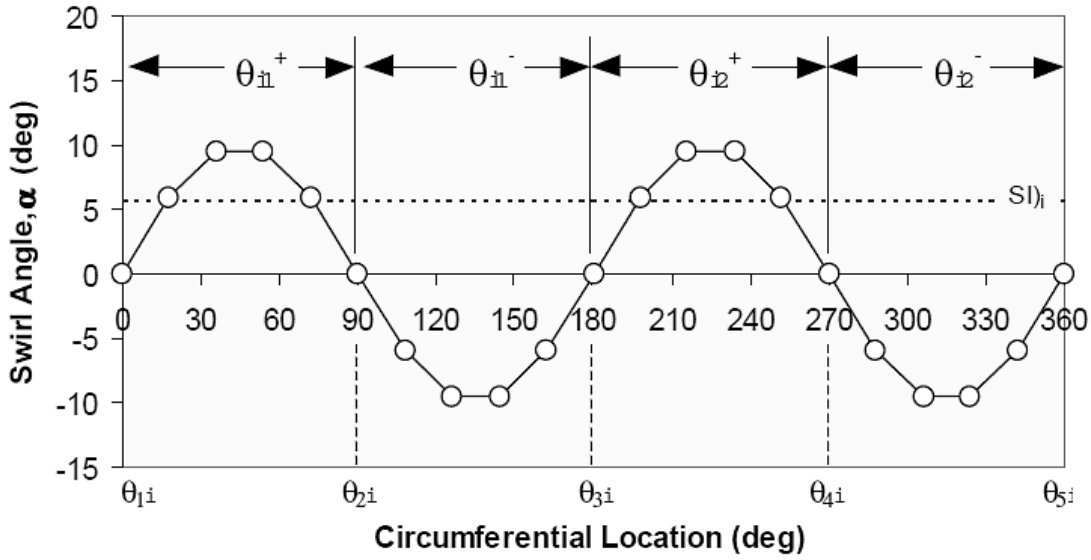

Figure 2-20: Two-Per-Rev Paired Swirl Pattern example [28]**.**

2.5.2.1 Sector Swirl (SS)

As before, is the average swirl on the positive/negative region of the k-th pair of swirl on the i-th ring. It is defined as the integral of the swirl angle over the $\theta_{i,k}^{+/-}$

$$SS_{i,k}^{+/-} = \frac{1}{\theta_{1,k}^{+/-}} \int_{\theta_{i,k}^{+/-}} \alpha(\theta)_{i,k} k d\theta \quad \textbf{(2-8)}$$

2.5.2.2 Swirl Intensity (SI)

Swirl intensity is the extent weighted swirl along the i-th ring:

$$SI_i = \frac{\sum_{k=1}^{m} SS_{i,k}^{+} * \theta_{i,k}^{+} + \sum_{k=1}^{m} |SS_{i,k}^{-}| * \theta_{i,k}^{-}}{360} \quad \textbf{(2-9)}$$

Where m is the total number of pairs of swirl regions.

2.5.2.3 Swirl Directivity (SD)

The swirl directivity with m pairs of paired swirl regions on a given i-th ring is:

$$SD_i = \frac{\sum_{k=1}^{m} SS_{i,k}^{+} * \theta_{i,k}^{+} + \sum_{k=1}^{m} SS_{i,k}^{-} * \theta_{i,k}^{-}}{\sum_{k=1}^{m} SS_{i,k}^{+} * \theta_{i,k}^{+} + \sum_{k=1}^{m} |SS_{i,k}^{-}| * \theta_{i,k}^{-}} \quad \textbf{(2-10)}$$

Figure 2-21 shows a spectra comparison between multiple and one-per-revolution patterns for the SD descriptor.

2.5.2.4 Swirl Pair (SP)

Swirl pairs indicates the number of multiple-per-rev patterns that are present at the i-th ring (Figure 2-22).

$$SP_i = \frac{\sum_{k=1}^{m} SS_{i,k}^{+} * \theta_{i,k}^{+} + \sum_{k=1}^{m} |SS_{i,k}^{-}| * \theta_{i,k}^{-}}{2 * Max\ of\ \{[\sum_{k=1}^{m} SS_{i,k}^{+} * \theta_i^{+}]\ or\ [\sum_{k=1}^{m} |SS_{i,k}^{-}| x \theta_i^{-}]\}} \quad \textbf{(2-11)}$$

Stability and performance assessments are done in industry procedures to provide technical visibility relative to target levels. The loss in stability margin due to distortion during the engine performance is computed based on the distortion descriptors [22].

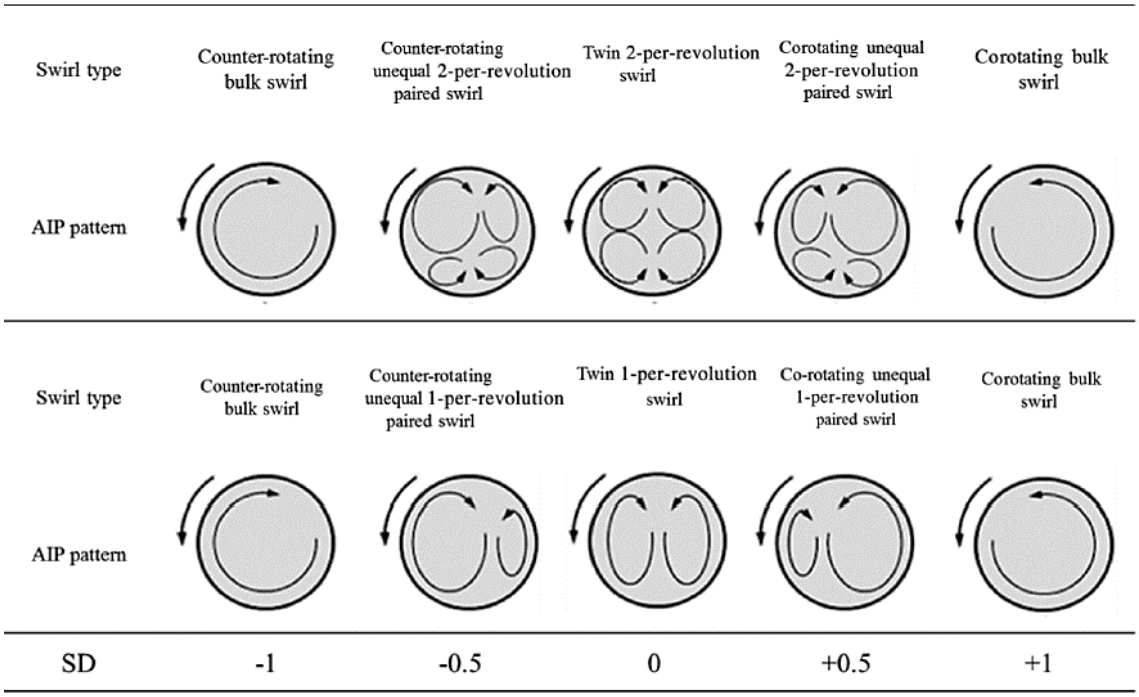

Figure 2-21: Multiple and one-per-revolution spectrum comparison for the SD descriptor.

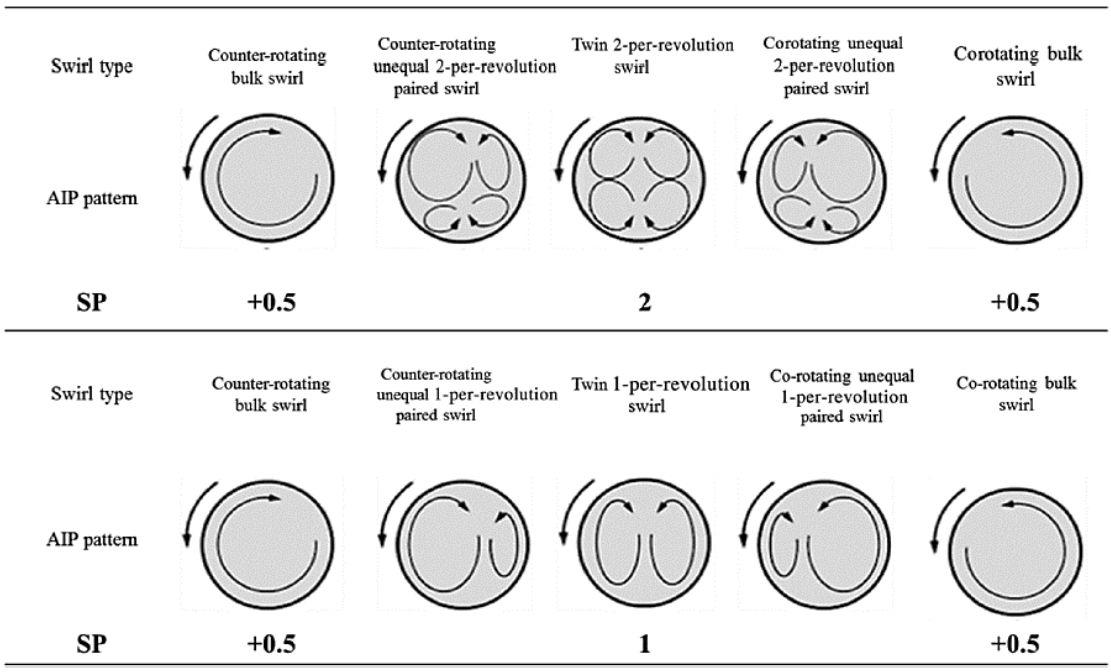

Figure 2-22: Multiple and one per revolution spectrum comparison, SP swirl descriptor.

2.6 Particle Image Velocimetry (PIV)

In the last decades, the growing number and quality of numerical calculations has widely increased the demand for high quality experimental results regarding flow structures, as well as for quantitative flow measurements. This to be able to validate and verify codes and models. For an experimental result to be adequate, a high resolution in time and space is required.

A conventional measurement technique for engine intakes is based on total-pressure rakes at the AIP, comprising an array of eight spokes with five probes each [7]. A similar approach, but with less spatial resolution, is also adopted for total temperature and swirl nonuniformities. Unfortunately, although these techniques can be supplemented with a subset of unsteady pressure measurements, they are not suitable to describe a detailed unsteady behaviour of the flow [7], [31].

In this context, Particle Image Velocimetry (PIV) distinguishes among the others as an appropriate experimental tool that provides higher spatial resolution across the AIP. PIV is a whole flow field technique that provides instantaneous velocity vector measurements,

and it is reliable, with a history that begun in the eighties of the last century. In the last years its applications have widely increased and PIV is now used in many different fields like aerodynamics, biology, space applications, combustion, micro devices and systems [31].

Due to the variety of its applications, the PIV technique has consistently changed along the years, mostly because of the scientific and technical progress in fields such as lasers, optics, computer techniques and videos. This has allowed to move from qualitative to quantitative flow visualisations and measurements of complex instantaneous velocity fields. In the aerodynamics field, PIV is of particular interest since its instantaneous image capture and high spatial resolution allow the detection of large and small-scale structures in unsteady flow fields [31].

Instabilities caused by convoluted aero engine intakes are still not completely clear, and need further study. To do so, there is a need for synchronous high-spatial-resolution measurements applied at S-duct intakes, that might allow a better understanding of the aerodynamics. In this context, PIV appears to be a suitable technique.

Although PIV is a mature technique, there is few work regarding the flow distortion across the crossflow plane of an intake, and no work at all considering a non-uniform mass flow at the inlet.

Particularly relevant for the purpose of this thesis is the work of P. Zachos et al. [4], that successfully demonstrated that it is possible to utilize the Stereo Particle Image Velocimetry (S-PIV) technique to determine the flow field at the exit of embedded engines. Moreover, the work states that a higher spatial resolution with respect to more common pressure measurements is achieved. The experimental results are particularly relevant, since they demonstrate that the swirl distortion level is underestimated by the conventional assessments based on time-averaged data.

2.6.1 PIV principle

The PIV principle is shown in Figure 2-23.

The flow under study is seeded with tracer particles and is illuminated in a target plane twice with a light sheet produced by a laser. It is assumed that the tracer particles move with the local flow between the two pulses, while the time delay (Δt) between them depends on the flow velocity and the magnification at imaging. The illuminated particles scatter the light, that is recorded via a high-quality lens either on a single frame or on two separate frames on special cross-correlation digital cameras. The camera sensor is able to capture each light pulse in separate image frames. Once the two light pulses are recorded, the images are divided into small squared subsections, called interrogation areas. The local displacement vector of the seeding particles is determined through statistical methods (auto- and cross-correlation) applied to these interrogation areas. A signal peak is later produced, that identifies the average particle displacement Δx. Sub pixel interpolation allows than to achieve an accurate particle (thus velocity) displacement. The projection of the velocity vector into the illuminated plane is calculated considering the time delay between the two light pulses and the magnification and images [31].

$$\overline{\mathrm{v}} = \frac{\overline{\Delta \mathrm{x}}}{\Delta \mathrm{t}} \qquad \textbf{(2-12)}$$

Repeating the cross-correlation for each interrogation area, an accurate velocity vector map of the target area can be obtained (Figure 2-24).

Some general features of PIV are [31]:

- **Non-intrusive velocity measurement.** Being an optical technique, the flow is not disturbed. This contrasts with techniques employing probes, pressure tubes, hot wires etc.
- **Indirect velocity measurement.** The measure is indirect thanks to the velocity measure of the particles within the flow.
- **Whole field technique.** A large part of the flow field is captured (i.e. large spatial resolution), which is a unique feature of the PIV technique.
- **Instantaneous image capture**

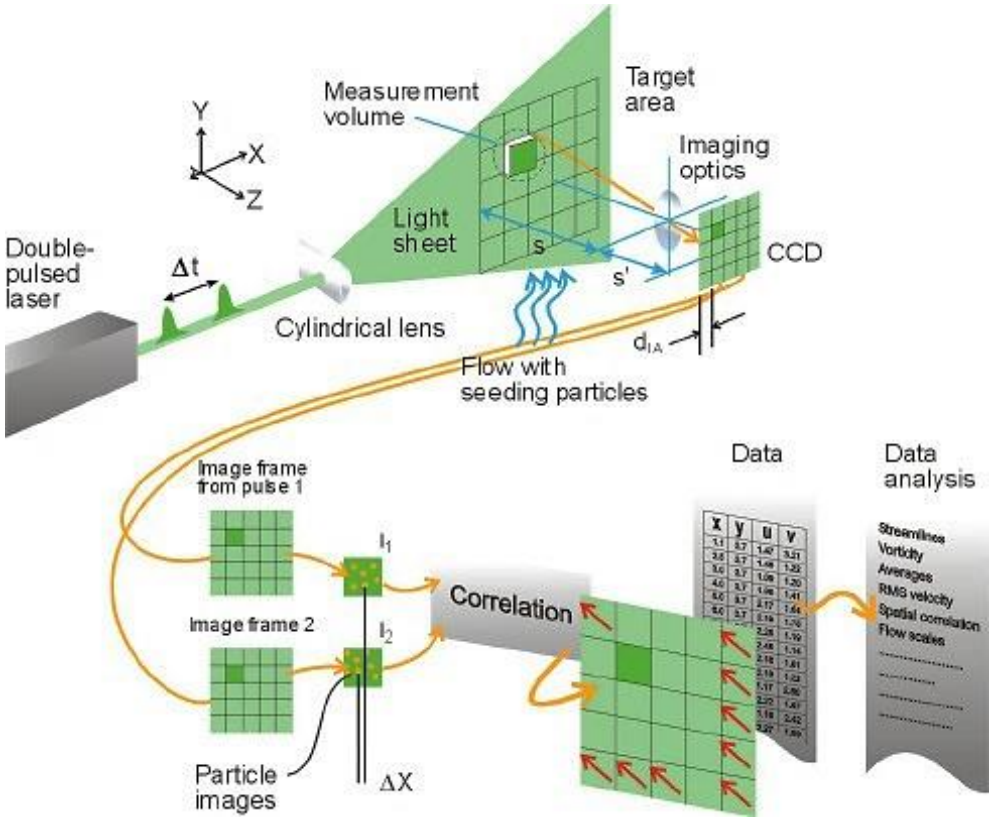

Figure 2-23: Experimental arrangement for particle image velocimetry in a wind tunnel. (Image courtesy: Dantec Dynamics)

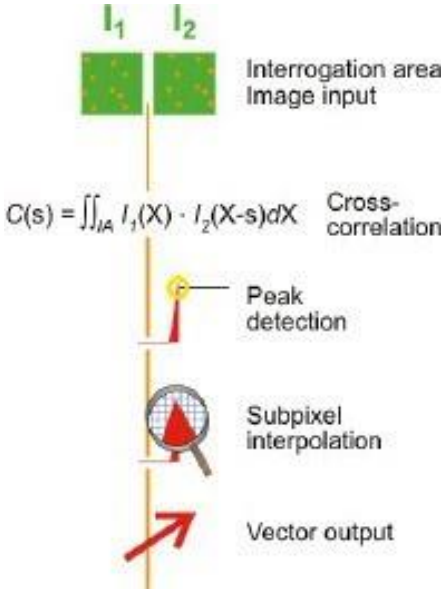

Figure 2-24: The correlation of the two interrogation areas, I_1 and I_2, results in the particle displacement Δx, represented by a signal peak in the correation C(Δx). (Image courtesy: Dantec Dynamics)

2.6.2 Stereoscopic PIV

The main disadvantage of the 'classical' 2D PIV method is that it only records the projection of the velocity vector in the light sheet plane, while the out of plane component cannot be measured [32]. Therefore, for highly three-dimensional flows, another approach to recover the complete velocity components set is suggested. In normal PIV methods the third velocity component is "invisible" due to the geometry of the imaging. If the flow is highly three-dimensional, this can lead to great errors in the measurement of the local velocity vectors. To overcome this limit, a new technique was developed: the Stereoscopic Particle Image Velocimetry technique (S-PIV). The main advantage of S-PIV is that it can provide an instantaneous 3D velocity vector map by using two cameras in a stereoscopic arrangement, as displayed in Figure 2-25. The three-component velocity vector is reconstructed from the perspective distortion of a displacement vector viewed from different directions. S-PIV is able to provide 200-300 times higher spatial resolution than typical rakes used in industry [8], and it can be successfully applied at the exit of complex intakes across a range of Mach numbers, as shown by Zachos et al. [4].

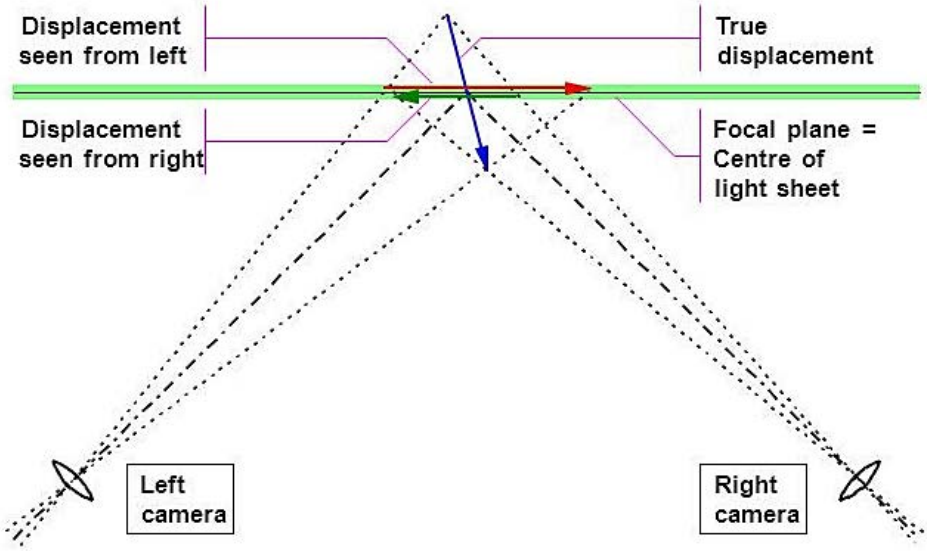

Figure 2-25: True 3D displacement is estimated from a pair of 2D displacements as seen from the right and left camera respectively. (Image courtesy: Dantec Dynamics)

Two different viewing angles allow to obtain the velocity vector projection in two planes, from which it is possible to extract all three velocity components

Unfortunately, S-PIV provides only velocity measurements, thus there is still need for total pressure distortion characterization [8].

2.6.2.1 Procedure for Stereo Vector Calculation in Davis software ©

To record S-PIV data, Davis software © was used.

To compute stereo vectors, the 2D2C- vector fields are computed for each camera, and through a stereoscopic reconstruction, a 2D3C-vector field is consequently computed. The procedures to do so are mainly three, and the method used by Davis software © is to first dewarp the images, and later to compute the 2D2C-vectors at the correct world grid position. The flow chart of stero PIV vector field computation is shown in Figure 2-26.

As depicted in the Figure below, the first step dewarps and evaluates the first vector computational pass of the four camera frames (two per camera, at t and t+dt). This first step already provides vectors at the correct position in the coordinate system, but the interrogation windows have different size and shape. This means that, if the light sheet has zero thickness, the correlation is done on the same particles. After this, a first 3C reconstruction is operated, removing the vectors in the 2C-vector fields that have a too large reconstruction error. After the spurious vector are removed, missing vectors are interpolated, and the resulting vector field is smoothed for stability reasons. The result is used as a reference for the subsequent passes, where the windows' sizes are different, resulting in a deformed image with half of the displacement in backward direction (assigned to the first image), and the other half in forward direction (assigned to the second image). The deformation of the image is later combined with the dewarping of the initial image, and usually 3 or 4 passes the 2D2C-vector fields converge successfully. After each pass, a 2D3C reconstruction takes place to eliminate the 2D2C-vectors with a reconstruction error above some threshold value. The 3C-reconstruction follows and consists in solving a system of four linear equations with three unknowns, that are the three velocity components. To solve it, the normal equation is used, that distributes the error over the three components. This is useful because it allows to reject the false vectors that produce a large reconstruction error. Finally, the reconstructed 2D3C-vector field is validated by a filter [32].

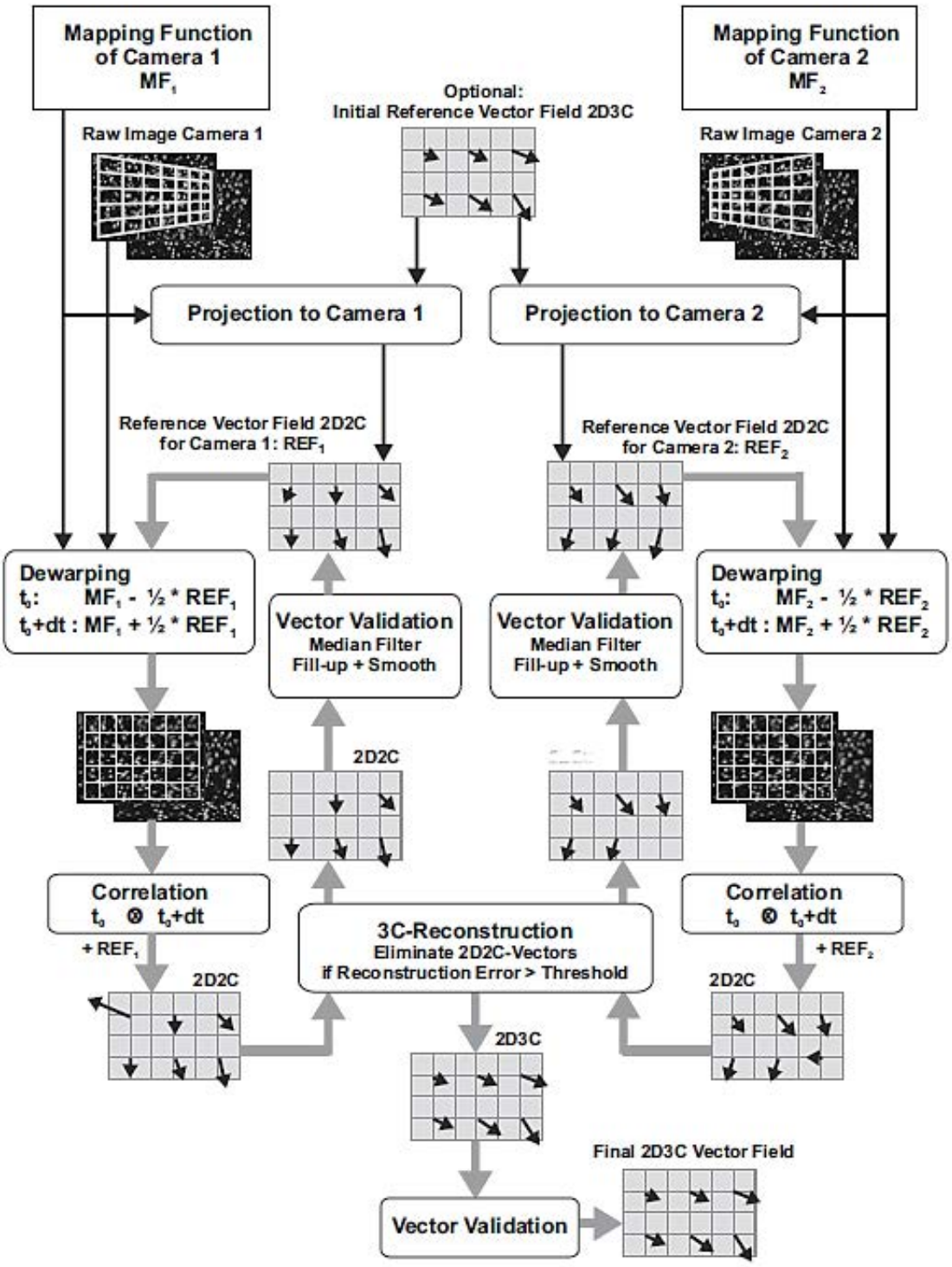

Figure 2-26. Flow chart of S-PIV vector field computation [32].

3 METHODOLOGY

In this chapter the experimental methods and procedures to measure and assess the velocity field at the Aerodynamic Interface Plane with the S-PIV technique are introduced. The experimental facility and the pieces of equipment, data acquisition, image processing and settings are reported, as well as the S-duct geometry and the flow conditions.

3.1 Experimental equipment and settings

3.1.1 Cranfield experimental facility

The experiment took place in a bespoke facility at Cranfield University, modularly designed to host a range of different S-ducts and to allow good optical access to enable S-PIV measurements at the Aerodynamic Interface Plane (AIP).

In Figure 3-1 the main pieces of equipment of the test rig are shown, numbered in order of appearance along the flow path. Figure 3-2 instead shows a facility schematic with the main locations used for the measurements, where the distances are calculated with reference to the duct inlet $D_{in} = 121.6\ mm$ and exit $D_{out} = 150\ mm$ diameters. The two main planes used for the experimental measurement are the reference plane location, distant $1.45D_{in}$ ahead the duct inlet, and the Aerodynamic Interface Plane (AIP), located at $0.41D_{out}$ after the S-duct exit.

In the facility, the flow first enters a seeding chamber (1), where oil particles (called seeding), characteristic of the Stereo Particle Image Velocimetry technique, are sprayed and pre-mixed into the air-stream. A bell-mouth intake (2) allows a smooth entrance of the fluid-flow into the facility, followed by a flow conditioning section (Figure 3-3). This part, with a diameter of $200\ mm$, contains a honeycomb mesh with a length of $100\ mm$ and $6\ mm$ hexagonal cells, whose function is to suppress the formation of large-scale structures in the fluid.

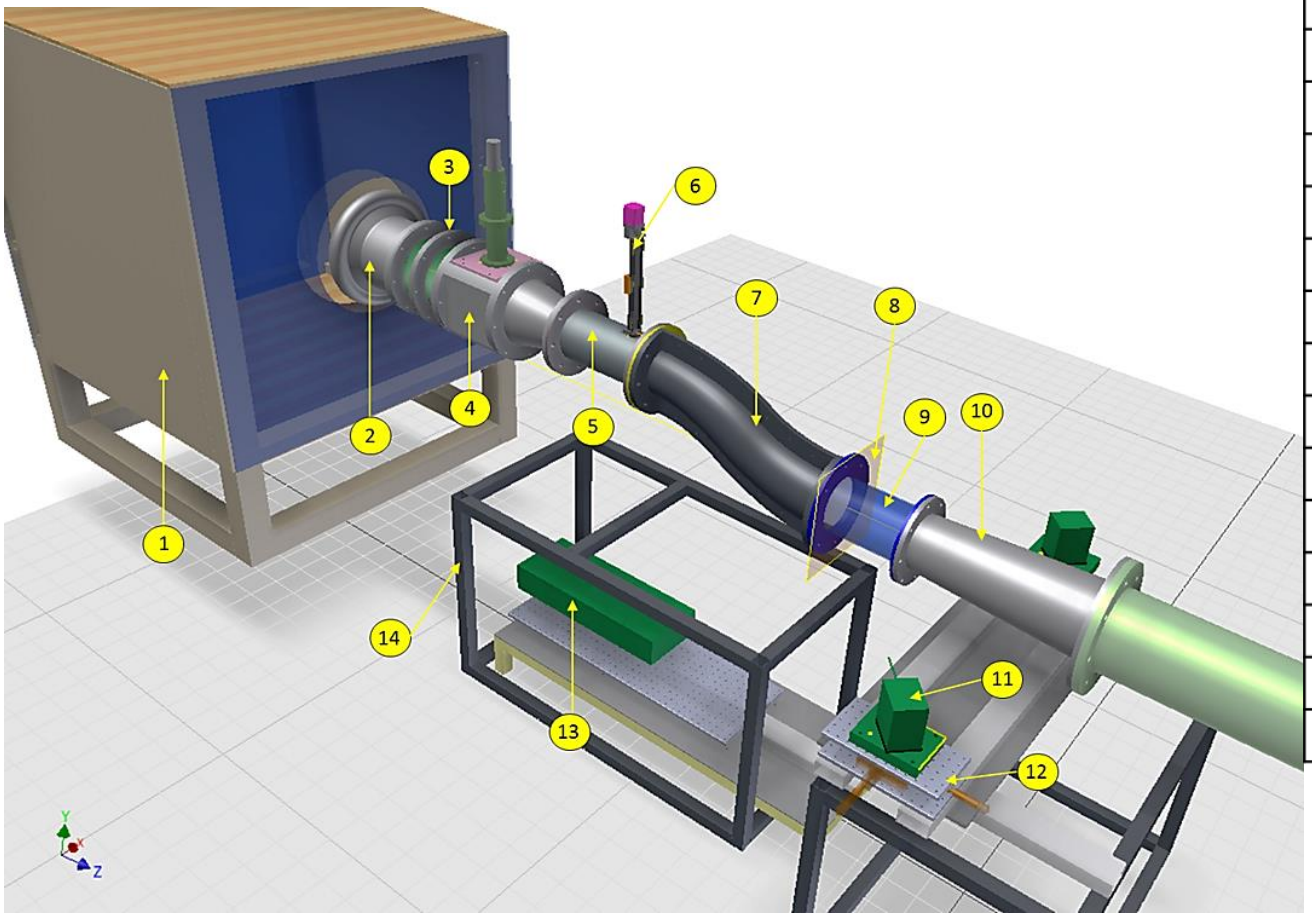

Legend	
1	Seeding chamber
2	Intake
3	Flow measurement section
4	Vortex generation section
5	Straight section
6	Inlet traverse station
7	S-duct
8	Measurement plane
9	Optical working section
10	Suction system
11	PIV camera
12	Camera traverse system
13	Laser
14	Support system

Figure 3-1: Cranfield test rig.

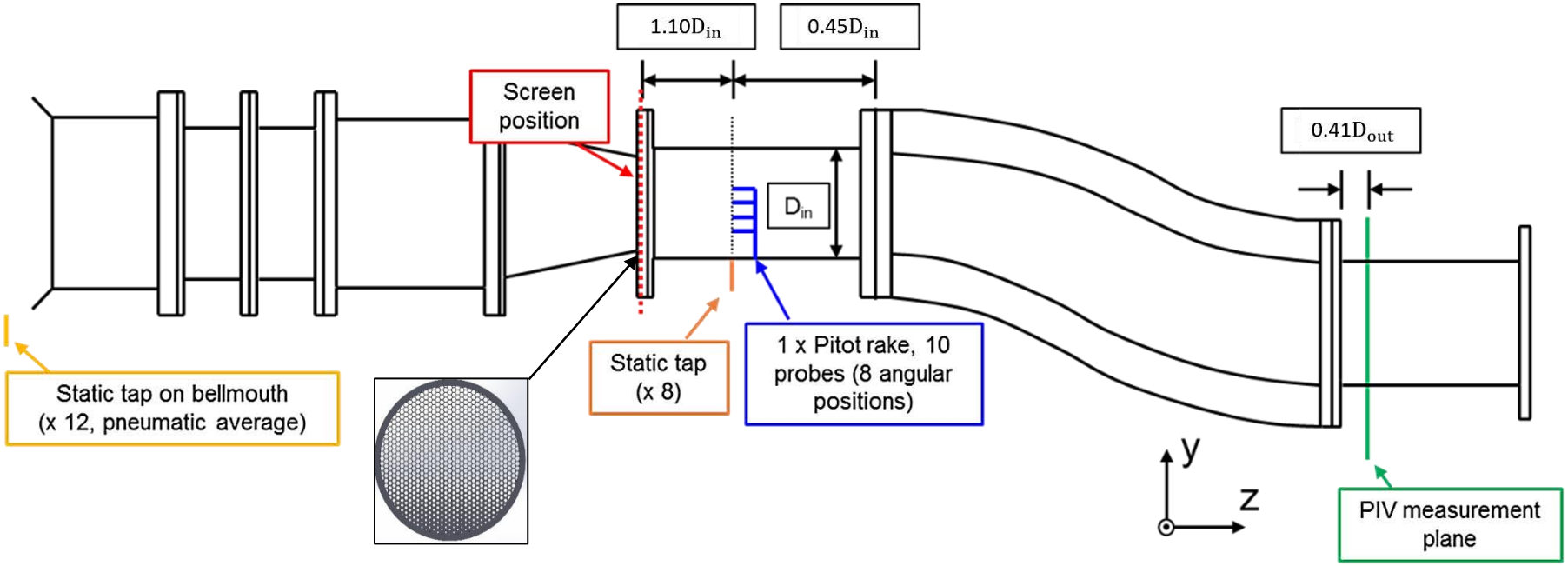

Figure 3-2: Cranfield test facility schematic.

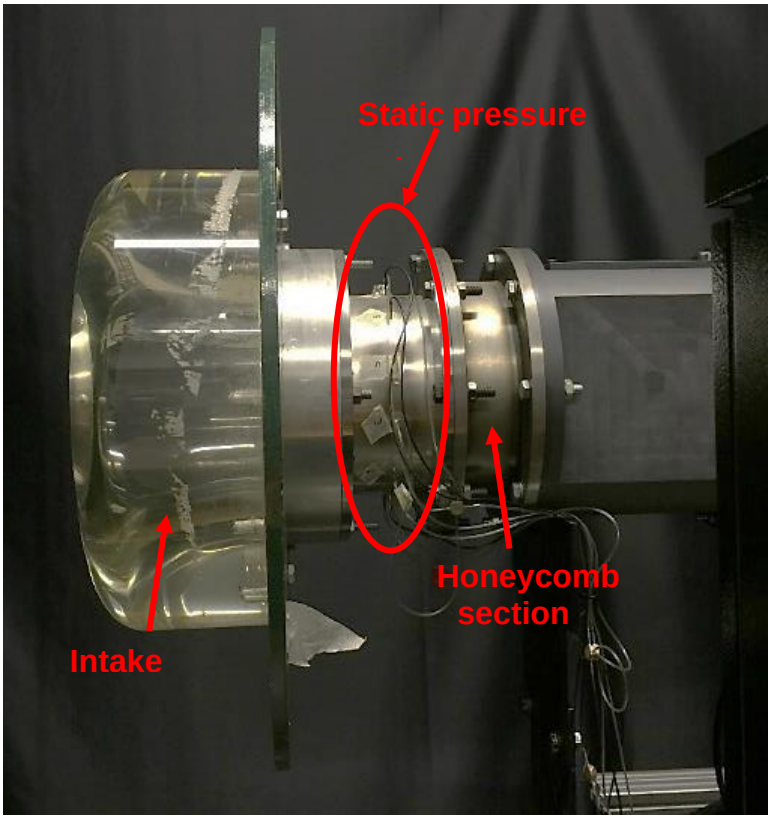

Figure 3-3: Intake throat and honeycomb section, with 12 static pressure tappings in between.

Twelve static pressure tappings, circumferentially equispaced, are placed between the intake throat and the honeycomb section (3). A constant diameter section of 200 mm follows (4), with the possibility to host a swirl distortion generator. At its end, a conical nozzle with a length of 200 mm reduces the fluid-flow area of the upstream components from a diameter of 200 to 121.6 mm, the latter being the same dimension of the S-duct inlet diameter (D_{in}). The conical component (Figure 3-4) provides a favourable pressure gradient to limit the growth of the boundary layer. At its end, a movable section allows to place a distortion screen into the flow field, to modify the ingestion of the boundary layer thickness. The S-duct entrance is connected to the nozzle through a constant-diameter straight section of 121.6 mm (5), that can accommodate pressure measurement instrumentation to determine the flow condition and to measure the boundary layer at a (calibration) reference plane located $1.45D_{in}$ upstream the duct inlet. The S-duct (7) progressively increases its diameter from $D_{in} = 121.6\ mm$ to $D_{out} = 150\ mm$.

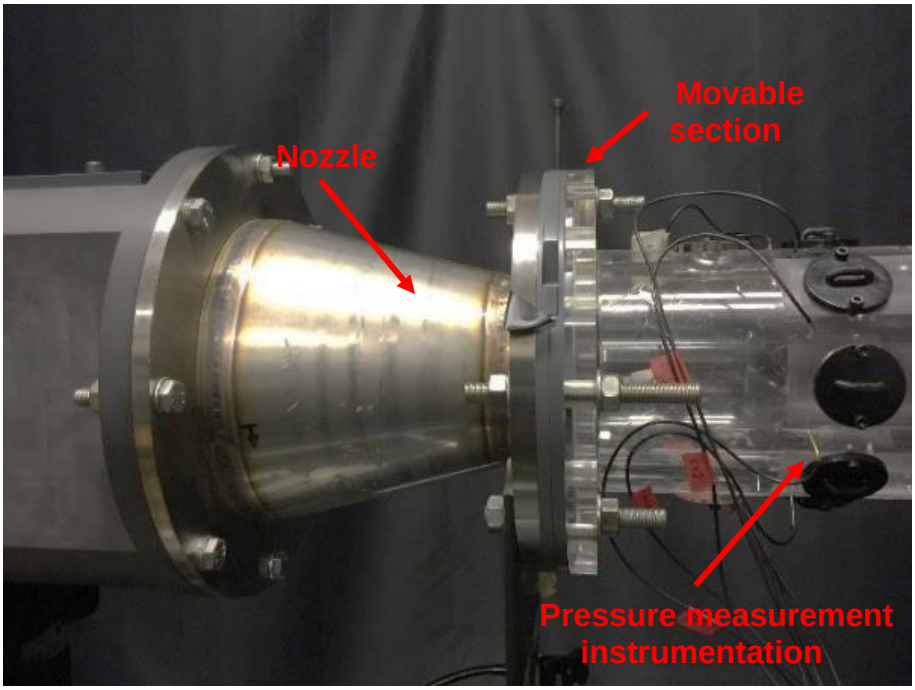

Figure 3-4: Nozzle section.

Another transparent straight section with constant diameter (9) is placed downstream the S-duct exit plane. This borosilicate glass working section, with a thickness of 5 mm, provides optical access for the laser (13) and the cameras (11) used in the S-PIV measurement, and hosts the reference measurement plane for the S-PIV technique (8), also called Aerodynamic Interface Plane (AIP). The plane is located at $0.41D_{out}$ from the S-duct outlet plane ($D_{out} = D_{AIP} = 0.150\ mm$). At the end of the facility, a retractable exhaust diffuser allows the air-stream to be ingested by a single-stage centrifugal fan (10), that drives the air through the facility.

3.1.2 S-duct geometry

For the purposes of this work, a high-offset duct with a simple circular cross-sectional area was chosen (Figure 3-5).

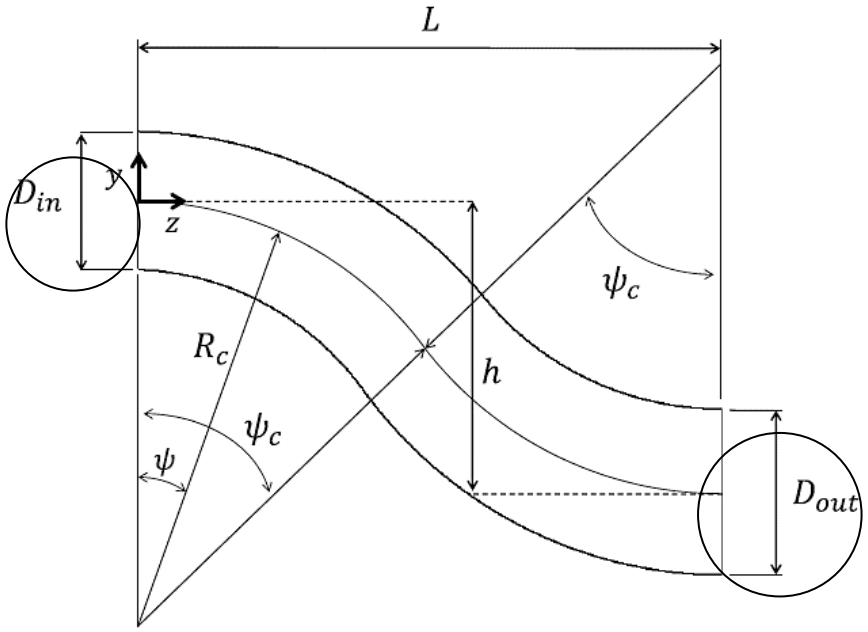

Figure 3-5: S-duct geometry [33].

The cross-sectional area progressively increases along the duct, from a diameter of $D_{in} = 121.6\,mm$ to $D_{out} = 150\,mm$ (Eq. (3-1)), and the diameter of the duct exit plane (D_{out}) equals the diameter of the Aerodynamic Interface Plane (D_{AIP}), located at $1.41D_{out}$.

$$\frac{R(\Psi)}{R_{in}} = 1 + 3\left(\frac{R_{out}}{R_{in}} - 1\right)\left(\frac{\Psi}{\Psi_c}\right)^2 - 2\left(\frac{R_{out}}{R_{in}} - 1\right)\left(\frac{\Psi}{\Psi_c}\right)^3 \quad \textbf{(3-1)}$$

The duct, with an S shape, is designed with the same non-dimensional geometry investigated by Wellborn et al. [25] and Garnier [34]. The centreline is the union of two consecutive arcs of radius R_c and angle Ψ_c, of length L_s, governed by the following equations (Eq. 3-2, Eq. 3-3):

$$z_{cl} = \begin{cases} -R_c \sin\Psi & 0 \le \Psi \le \Psi_c \\ 2R_c \sin(\Psi_c|2) - 2R_c \sin(\Psi_c - \Psi) & \Psi_c < \Psi \le 2\Psi_c \end{cases} \quad \textbf{(3-2)}$$

$$y_{cl} = \begin{cases} R_c(\cos\Psi - 1) & 0 \le \Psi \le \Psi_c \\ 2R_c \cos(\Psi_c|2) - R_c(1 + \cos(\Psi_c - \Psi)) & \Psi_c < \Psi \le 2\Psi_c \end{cases} \quad \textbf{(3-3)}$$

Table 3-1 resumes the main geometrical parameters of the duct, where A_{out} and A_{in} are the areas of the inlet and exit cross-sectional areas.

Table 3-1: High-offset S-duct geometrical parameters.

Parameter	Value
$\boldsymbol{A_{out}/A_{in}}$	1.52
$\boldsymbol{L/D_{in}}$	4.95
$\boldsymbol{h/L}$	0.49
$\boldsymbol{R_{in}/R_c}$	0.16
$\boldsymbol{\Psi_c}(°)$	52.55
$\boldsymbol{L_s/D_{in}}$	5.72
$\boldsymbol{D_{out}}$ $\boldsymbol{(mm)}$	150
$\boldsymbol{D_{AIP}}$ $\boldsymbol{(mm)}$	150
$\boldsymbol{h/D_{in}}$	2.44

3.1.3 Rig operating point and tunnel calibration

The operating condition of the rig is quantified with the Mach number (M_{ref}) calculated at the calibration reference plane, located $1.45D_{in}$ upstream the duct inlet (Figure 3-2). A certain amount of pressure loss across the flow straightener and the distortion screen must be taken into account, since it modifies the reference Mach number value (and flow velocity) downstream their positions. While the pressure loss across the flow straightener is known, the pressure loss across the distortion screen depends on many different parameters, like geometry and material composition. When the screen is installed, the rig calibration ensures $M = 0.27$ upstream the screen location, as the dedicated control system relies on the ratio p_{static}/P_{amb} to derive the Mach number at the bell-mouth intake exit. p_{static} is the static pressure measured by the twelve static pressure tappings ahead the honeycomb section (Figure 3-3), while P_{amb} is the total ambient pressure. However, this first tunnel calibration only fixes M_{ref} upstream the distortion screen location, but the presence of the screen introduces a pressure loss that affects both the magnitude and the uniformity of the Mach number distribution. Since the desired reference Mach number (M_{ref}) needed to be ensured downstream the screen at the reference plane, a second calibration was needed. For the second calibration, eight equi-spaced static-pressure tappings on the duct wall of the reference plane (Figure 3-4) provide the average static pressure value (p_{ref}). p_{ref}, together with the total pressure (P_{ref}) calculated at the centre of the reference plane by means of a Pitot pressure probe,

allows to calculate the rig operating condition at the reference plane (Eq. 3-4). The compressor is run at a higher rpm until the desired Mach number is achieved.

$$\boldsymbol{M_{ref} = \sqrt{\frac{2}{\gamma-1}\left[\left(\frac{P_{ref}}{p_{ref}}\right)^{\frac{\gamma-1}{\gamma}} - 1\right]}} \quad \textbf{(3-4)}$$

However, the introduction of a pressure probe into the flow field is quite an intrusive measurement technique, that modifies the flow field downstream the calibration reference plane. Therefore, this type of calibration can be used only prior the PIV measurements. For the PIV measurement, the reference Mach number M_{ref} is calculated again through the static-to-total pressure ratio (p_{static}/P_{amb}) at the plane located between the bell-mouth inlet section and the honeycomb mesh (Figure 3-3), with the value of p_{static} being imposed from the second calibration. Four operating points at Mach numbers $= 0.2, 0.22, 0.24, 0.26$ were considered during the PIV measurement calibration, and the values found interpolated. A pre-existing Spreadsheet was used to find the necessary constant values to insert into a 3rd order polynomial function, that finally expresses the required M_{ref} as a function of p_{static}/p_{amb} (Eq. 3-5).

$$\boldsymbol{M_{ref} = A\left(\frac{p_{static}}{p_{amb}}\right)^3 + B\left(\frac{p_{static}}{p_{amb}}\right)^2 + C\left(\frac{p_{static}}{p_{amb}}\right)^4 + D} \quad \textbf{(3-5)}$$

After the operating condition is met, it is automatically set and maintained by a dedicated control system, that acts on the rotational speed of the fan to match it with the p_{static}/p_{amb} ratio obtained from the second calibration of the rig. The control system consists in a proportional-integral closed loop able to provide the required DC voltage to a monitor, that controls the fan speed. The ratio p_{static}/p_{amb} is sampled at a frequency of 100Hz, and the control loops uses a moving average value that is calculated through a 250 samples moving-window.

3.1.4 Non-uniform flow profile, cases studied and flow condition

For this work, a distortion screen in polylactic acid (PLA) was placed at a distance $L_{screen} = 2.55D_{in}$ from the duct inlet (Figure 3-2) to simulate the ingestion of a non-uniform inlet flow profile. The screen used for the experimental measurements was 3D-printed, designed in order to provide the same pressure profile investigated by Giuliani

[9] (Figure 3-6), that consists in a non-uniform flow profile with a thickness of $\delta/D_{in} = 0.336$.

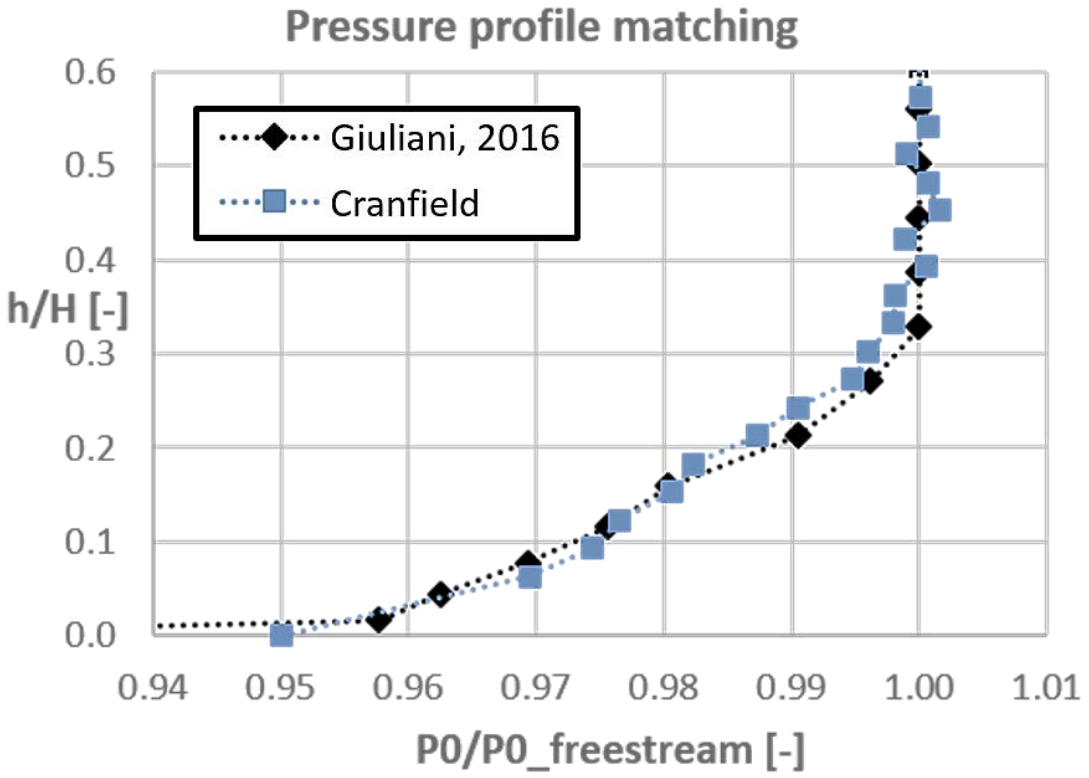

Figure 3-6: Pressure profile matching between the experimental and Giuliani's pressure profile [9].

The distortion screen used during the experimental measurements had a thickness in the flow direction of 3.8 mm, a constant pitch value of 4 mm and a minimum wall thickness of 0.3 mm in the freestream area. The wall thickness of the entire screen had been experimentally calculated through a calibration between a loss coefficient and the wall thickness itself during previous experimental work (Figure 3-7). The presence of the screen introduces a pressure loss in the freestream zone of $\Delta P = 1.569 kPa$.

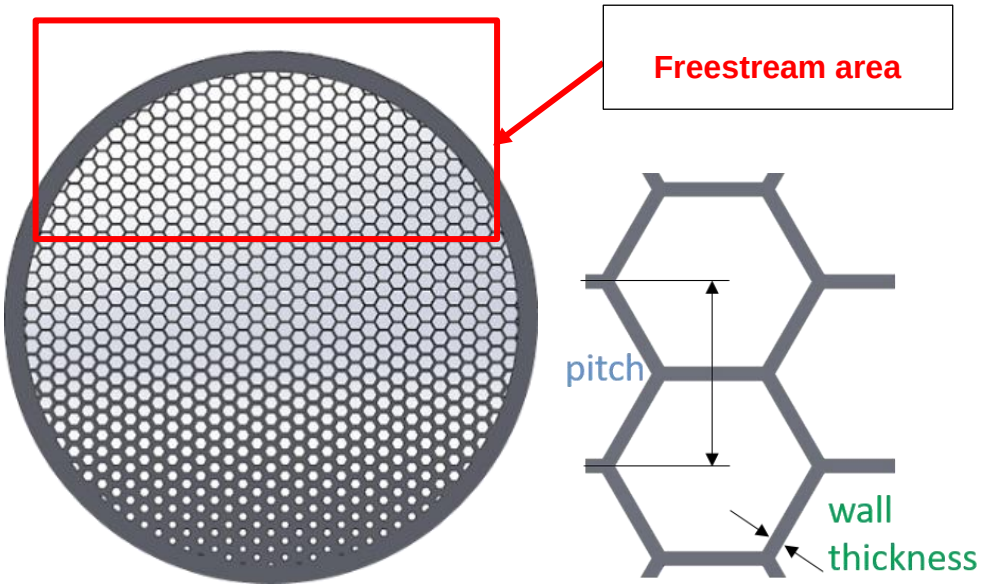

Figure 3-7: Screen geometry. Entire screen view (left) and cells particular (right).

The cases studied with the PIV measurements were in total six. A baseline case with a uniform inlet profile of $\delta/D_{in} = 0.04$ thickness was first measured to be used as a reference case. The thickness of the baseline case inlet flow profile, caused by the friction of the flow against the S-duct wall, was previously calculated by Gil-Prieto at the reference plane located $0.9D_{in}$ upstream the duct inlet [33]. For the sake of ease, as in the work of Gil-Prieto [33] the static pressure across the BL was assumed uniform for the calculation of the BL thickness. Five cases were later measured with the distortion screen. To simulate the ingestion of a non-uniform flow profile at different inlet locations, four rotations of 45 degrees were applied to the distortion screen. The final studied cases were therefore: $\theta = 0°, 45°, 90°, 135°$ and $180°$, with θ being the angle between the vertical axis of symmetry of the S-duct inlet plane and the local vertical axis of symmetry of the distortion screen, as seen from a downstream point of view (Figure 3-8). The test matrix is resumed in Table 3-2. The flow condition was set to $M_{ref} = 0.27$, with a Reynolds number of 7.48e+5. The incoming boundary layer was assumed to be fully turbulent.

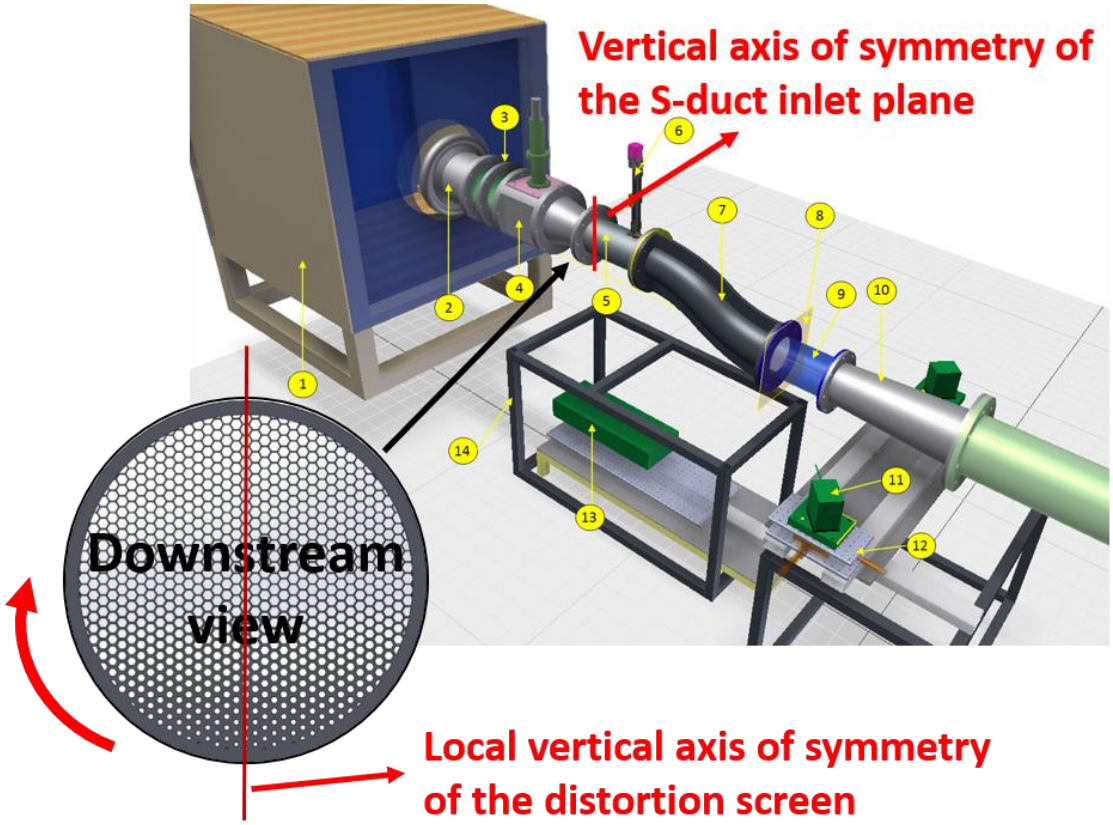

Figure 3-8: Screen rotation particular with respect to the vertical axis. Downstream view.

Table 3-2: Test matrix for S-PIV tests at $M_{ref} = 0.27$.

Case	Boundary layer thickness
Baseline	$\partial/D_{in} = 0.04$
Distortion screen at $\theta = 0°$	$\partial/D_{in} = 0.336$
Distortion screen at $\theta = 45°$	$\partial/D_{in} = 0.336$
Distortion screen at $\theta = 90°$	$\partial/D_{in} = 0.336$
Distortion screen at $\theta = 135°$	$\partial/D_{in} = 0.336$
Distortion screen at $\theta = 180°$	$\partial/D_{in} = 0.336$

Table 3-3: Distortion screen parameters.

Parameter	Value
δ/D_{in}	0.336
H (mm)	121.6
Mach	0.27
Pitch value (mm)	4
Material	Polylactic acid (PLA)
Minimum wall thickness (mm)	0.3
Pressure loss (kPa)	1.569

3.2 Time-Resolved Stereo Particle Image Velocimetry measurement

The experimental method used to measure the velocity field at the exit plane of a complex duct was the Time-Resolved Stereo Particle Image Velocimetry technique. The measurements were taken at the Aerodynamic Interface Plane (AIP) located $0.41D_{AIP}$ downstream the S-duct exit plane. The two cameras, that pointed at the AIP, were used to reconstruct the out-of-plane component. The description of the main devices to implement the PIV technique follows.

3.2.1 Laser

A high-speed Nd:YAG laser DM100-532-DH manufactured by *Photonics Industries International* [35] was used to illuminate the AIP. The laser beam was converted into a $1.5\ mm$ thin light sheet by means of an articulated laser arm, that contains a series of optical lenses. Generally, the laser can operate at a wavelength of 532nm, with a nominal energy output of 10mJ/pulse and a pulse duration of 130ns, at a nominal repetition rate of 10kHz.

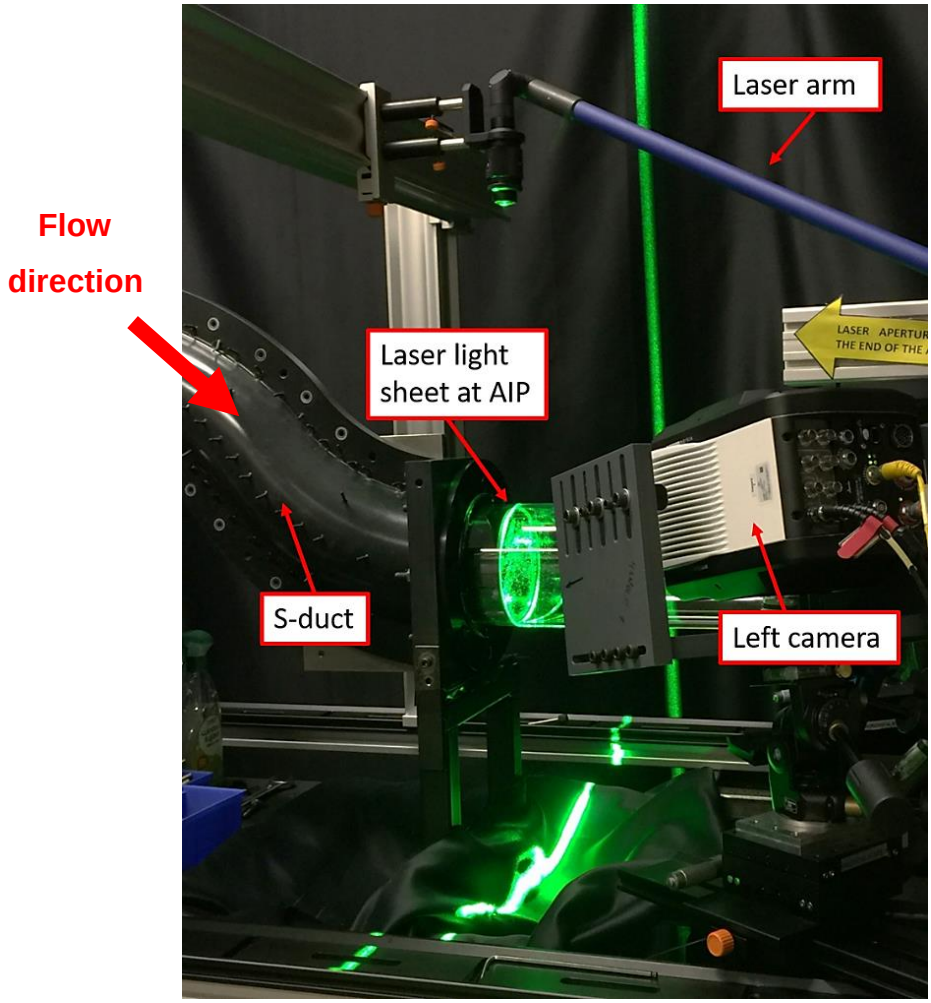

Figure 3-9: Laser configuration, image captured during a TR S-PIV measurement.

Table 3-4: Nd: YAG laser main parameters.

Parameter	Value
Type	High speed Nd:YAG laser DM100-532-DH
Manufacturing company	Photonics Industries International
Year	2018
Wavelength	532nm
Energy output	10Mj/pulse
Pulse duration	130ns
Pulse repetition rate	4kHz
Time delay between the pulses	4μs

3.2.2 S-PIV cameras

Two high speed 1MP CMOS cameras *Phantom v1612* [36] manufactured by *Vision Research* were used. The cameras have a CMOS sensor of rectangular shape, which can acquire up to 16,000 frames per second. This means that velocity fields can be acquired for frequencies up to 8.3 kHz. The cameras were positioned backward forward scattering, on the same side of the light sheet (Figure 3-10). In such a configuration, one camera records the light scattered in forward direction, while the other camera records the light scattered in the backward direction.

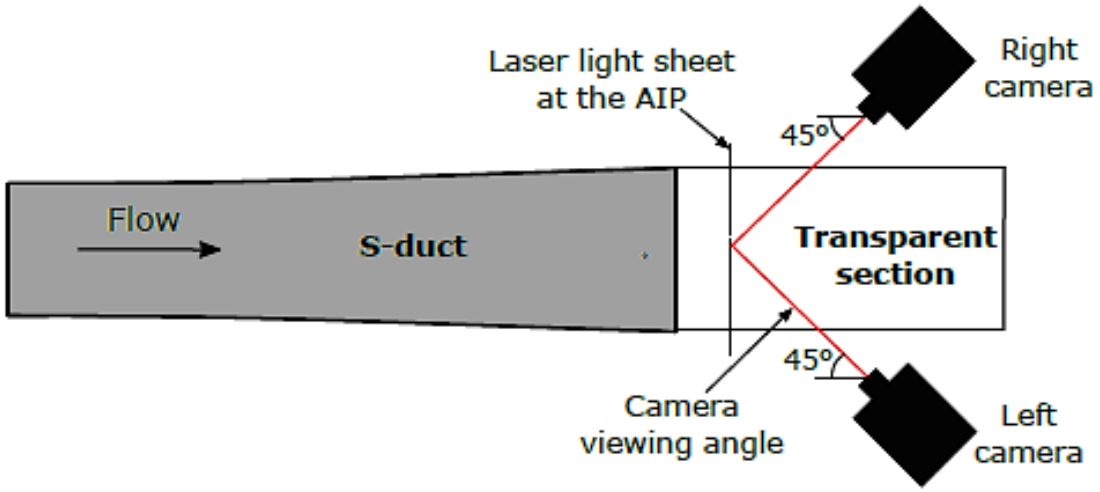

Figure 3-10: Backward forward scattering camera positioning [33]**.**

The cameras were symmetrically arranged to increase the accuracy in the calculation of the vectors. For the experimental measurements, a camera portrait view was used (Figure 3-11), that means that the cameras were rotated of 90 deg each, for the sensor to provide a resolution of $800x1280$ pixels instead of the usual $1280x800$ pixels, typical of the landscape configuration. With this view, higher spatial resolution and less sensor waste were expected. The positions and the focus of the cameras were manually adjusted to provide a homogeneous vertical and horizontal focus of the AIP (Figure 3-12).

After this procedure, the cameras had approximately a viewing angle of 45° (Figure 3-13), and a tilt angle of 15° (Table 3-5). Their stand-off distance, i.e. the distance from the AIP plane, was of 350 mm (Table 3-5). With such configuration, a spatial resolution of approximately $2.1x.\,2.1\ mm$ was finally achieved.

Table 3-5: Cameras parameters.

Parameter	Value
Cameras' view	Portrait mode (Figure 3-11)
Camera viewing angle	45 deg. ca.
Camera rail angle	30 deg. ca.
Camera tilt	15 deg. ca.
Handle position	External for both sides
Stand-off distance	350 mm ca.
Lenses	60 mm
Scheimpflug correction	3D
Cameras resolution	800x1280

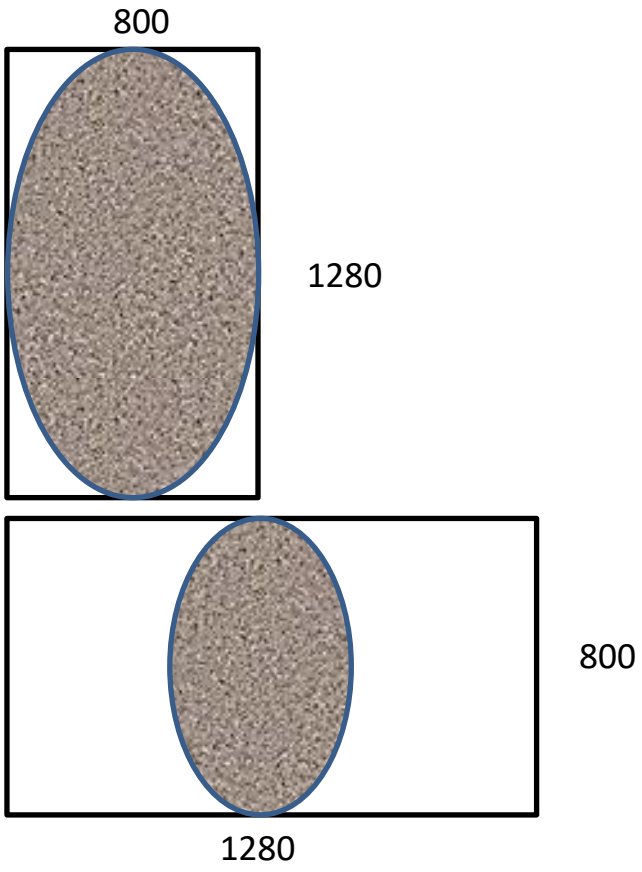

Figure 3-11: Landscape (above) and Portrait (below) camera views.

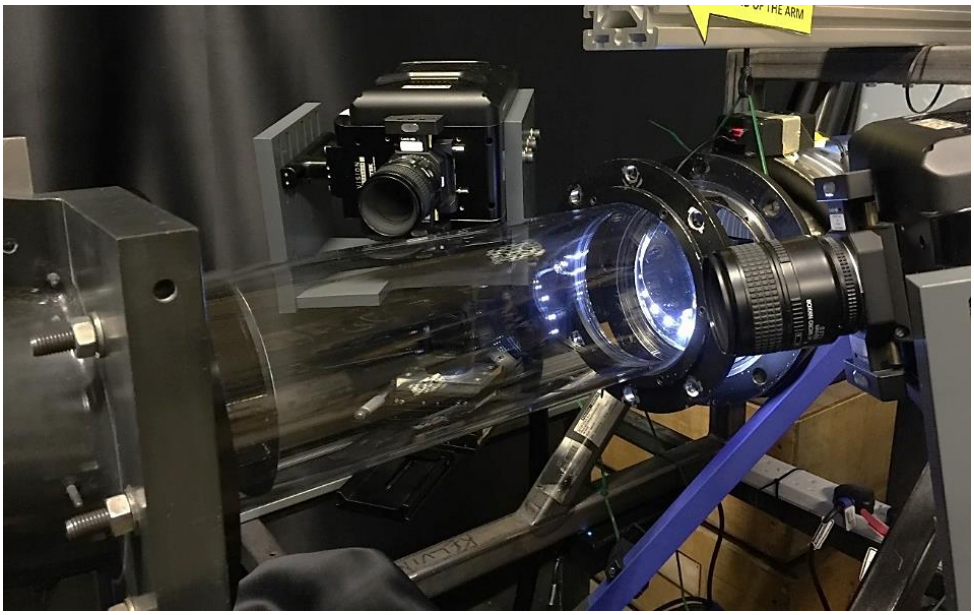

Figure 3-12: Camera configuration, Cranfield rig.

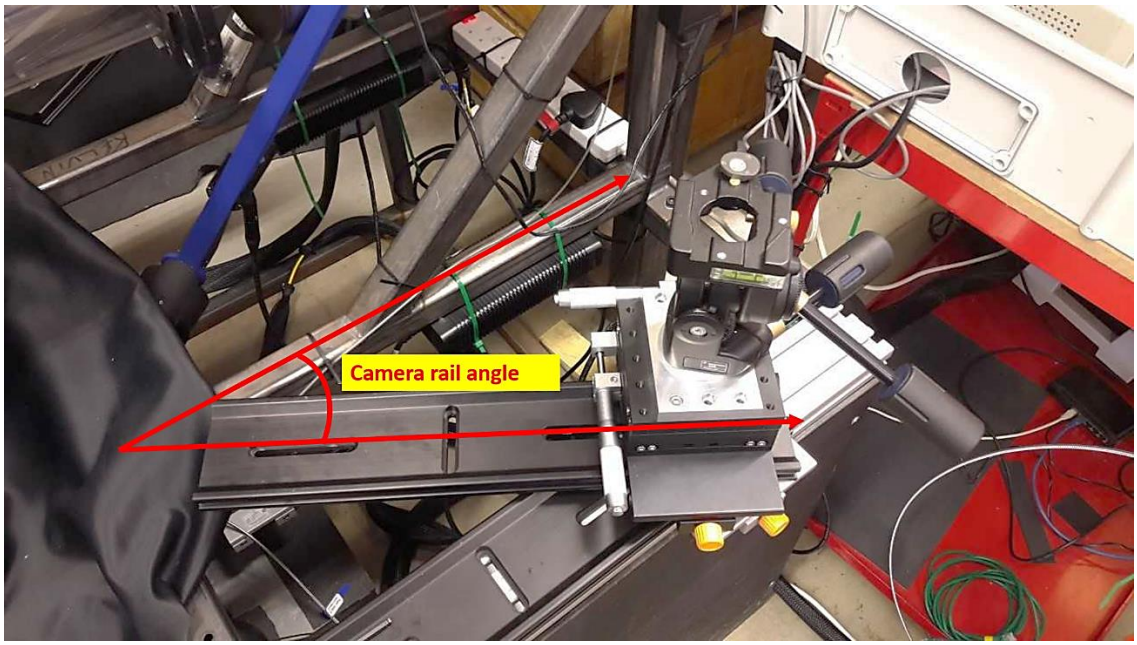

Figure 3-13: Camera rail angle.

The acquisition frequency for the experiment, for $M_{ref} = 0.27$, was set to 4kHz, approximately 10 times higher than the greatest dominant flow frequency of around $S_t = 1.0$, as predicted by DDES results previously computed by Gil-Prieto [33]. At that

frequency, the cameras saturated their capacity after $t_{experiment} = 5s$, with the acquisition of 20,000 snapshots per studied case. During the experiment, each camera took two frames at each snapshot, separated by a time delay corresponding to the two laser pulses (Figure 3-14).

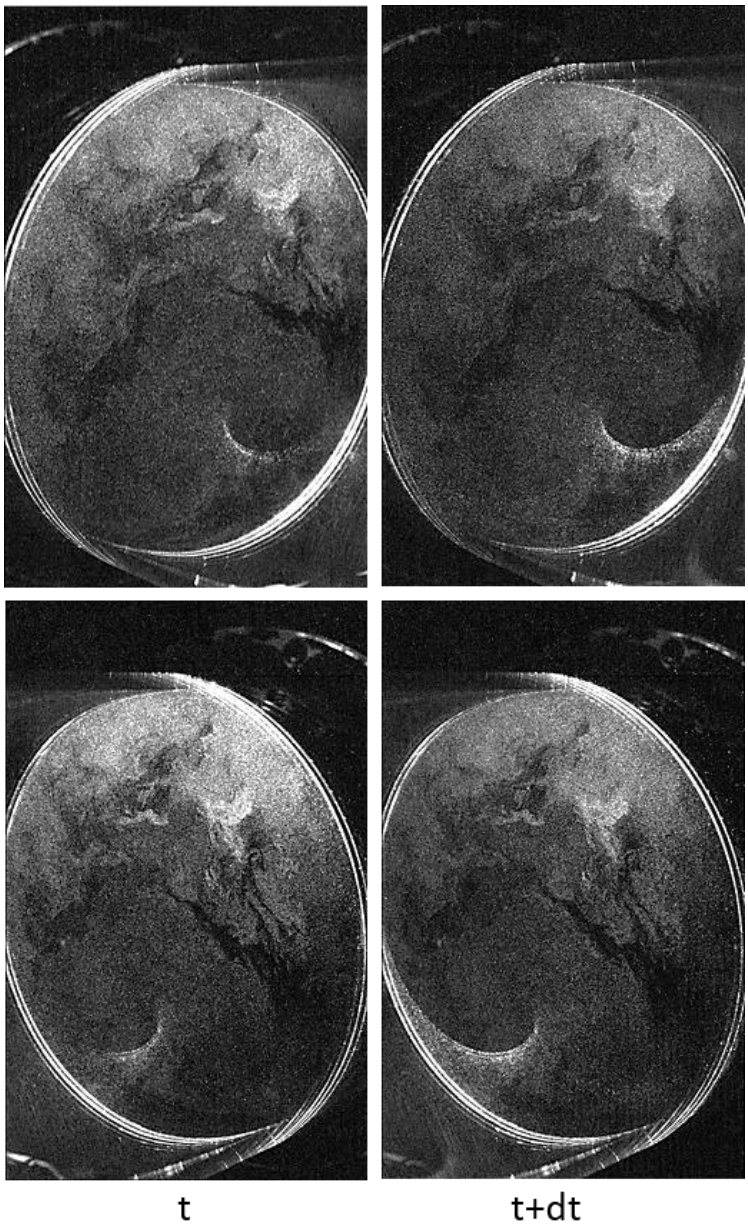

Figure 3-14: Right (above) and left (below) camera pair of frames.

The time difference between each snapshots was of $\Delta t = \frac{Experiment\ duration\ [s]}{Total\ number\ of\ snapshots} = \frac{5}{20000} = 2.5 * 10^{-4} s$. A pair of AF 1.8/D Nikkor lenses with 60 mm focal lengths was

used. A 3D Scheimpflug correction was achieved by tilting the cameras (and sensors) within the horizontal plane, to ensure a uniform focusing across the AIP by the intersection in a common line of the image, lens, and object planes.

The cameras were set to stereo-cross correlation, double-frame camera mode.

3.2.3 Seeding particles

The seeding particles have an important role in the Stereoscopic Particle Image Velocimetry technique, that relies on their ability to follow the instantaneous airflow. The dimension of the particles is a compromise between their flow tracking capability and the characteristics of the light scattering [31]. The seeding particles, with a dimeter of $1\ \mu m$, were provided by a *PivPart160* Laskin nozzle particle generator manufactured by *PIVTEC*. Both the flow tracking capability and the light scattering characteristics were found to be reasonable for this work. The air-flow was seeded with the seeding particles while passing through the seeding chamber (Figure 3-1), that ensured an appropriate distribution of the seeding. The ability of the particles to follow the flow field within the range of frequencies of interest was studied by Gil-Prieto [33], and it was based on Melling's work [37].

The time delay between the two pulses of the laser corresponds to the two different frames recorded by each camera (Figure 3-14). To evaluate which time delay provides the best displacement, three initial measurements were taken at $\Delta t = 3, 3.5, and\ 4\ \mu s$. According to Davis' manual [38], the Δt value has to be chosen for the particle image shift ds to be in the interval given by the resolution of the system, and by the maximum allowable particle shift, the latter being approximately a quarter of the interrogation window size (0.1 pixel < ds < ¼ interrogation window size). The particle shift can be observed in the raw images obtained from the measurements, while toggling between the frames taken at t and $t + \Delta t$ (Figure 3-14). The time delay between the two laser pulses selected for this work was $\Delta t = 4\ \mu s$. With a spatial resolution of $2.1x2.1$ mm, this allowed to detect 3095 velocity vectors at the AIP.

3.2.4 Cameras spatial calibration

The spatial calibration of the cameras is needed to convert the displacement of the seeding particles from pixels, output of the processing of the S-PIV images, into meters. For this work, a 6 mm thick target plate was used, characterised by a rectangular grid with dots of 1.75 mm in dimeter, equi-spaced of 5 mm. In the process, particular attention needs to be paid to the alignment of the measurement plate with the light-sheet. The calibration plane is placed exactly at the AIP, 61 mm after the S-duct exit plane. To be able to host the calibration plate, the duct was manufactured in two symmetrical parts. For the calibration to be accomplished, the right part of the duct was removed to mount the calibration plate, later removed during the experiment measurement. Since the calibration target must be imaged at different axial positions across the light-sheet, the measurement plate was mounted on a traverse system, that allows to shift its position. Three different equi-spaced planes at a traverse distance of 1.5 mm were chosen along the light-sheet thickness, for a total displacement of 3 mm. During the calibration process, the lights of the test room were switched off, while the calibration plate was illuminated with an array of LEDs (Figure 3-15). The light intensity contrast between the black background and the illuminated markers was therefore enough to enable *Davis 8.3.1* commercial software to identify the markers of the calibration plate based on a light-intensity threshold. For the calibration, a third order polynomial function was used in the in-plane direction, while a second-order calibration polynomial was used in the out-of-pane direction. These polynomials were computed with a least-square fit of all the markers position to convert at any position across the image from image to physical units.

3.3 Processing of the Time Resolved S-PIV images

The images acquired during the experiment were processed with *Davis 8.3.*1 commercial software, that offers extensive tools for the acquisition of data, and the visualization and evaluation of flow fields. The images were processed through a list of operations, selected among others to provide the best output.

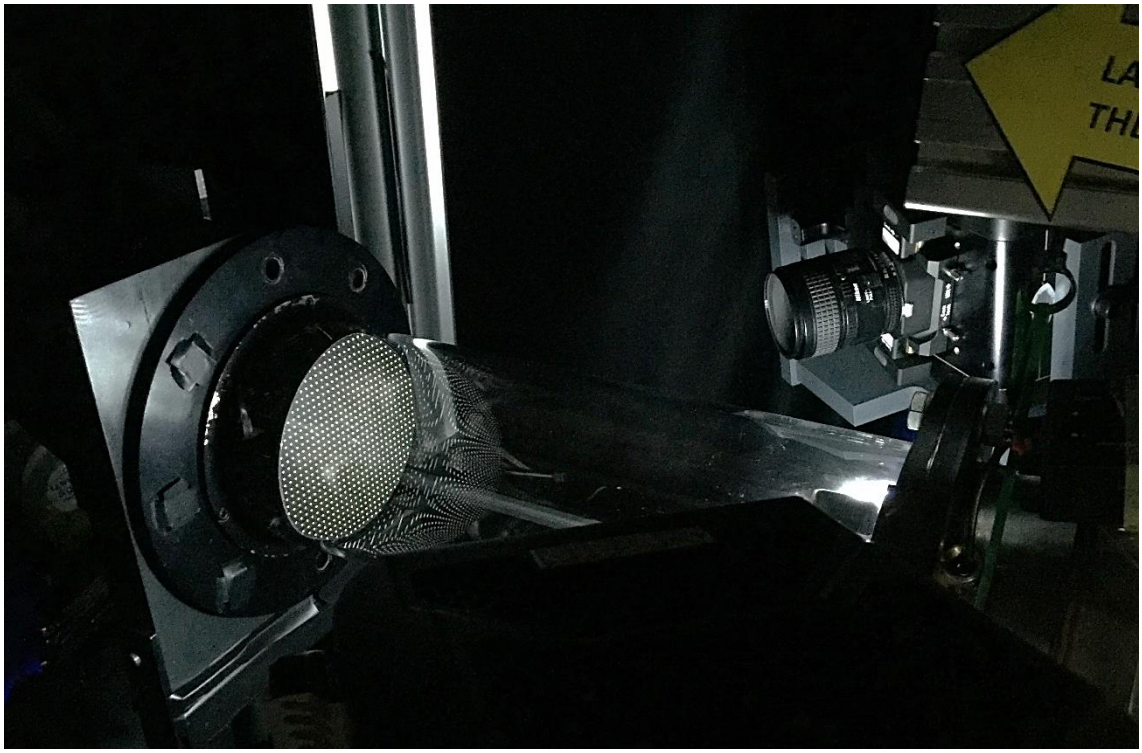

Figure 3-15: Calibration plate illuminated by an array of LEDs.

3.3.1 Frame extraction and merge

Unlike previous experiments, the cameras were positioned in portrait view for the first time. During the experiment measurements, the data were downloaded from the camera in landscape mode. Therefore, the additional step of rotating the data had to be added to the processing list. The procedure consisted in the extraction of each frame, in the frame rotation (of $\vartheta = 90°$ for the frames of the left camera, and $\vartheta = -90°$ for the frames of right camera), and in their merge. This additional process took between $5h$ and $7h$ per case studied.

3.3.2 Stereoscopic calibration

Before the processing, some considerations about the raw data collected were made:

- Quite high levels of background noise affected the raw data at the top of the AIP (Figure 3-16);
- The seeding level was particularly low in the bottom-right region (Figure 3-16);
- The level of particle illumination and light reflection was satisfactory;

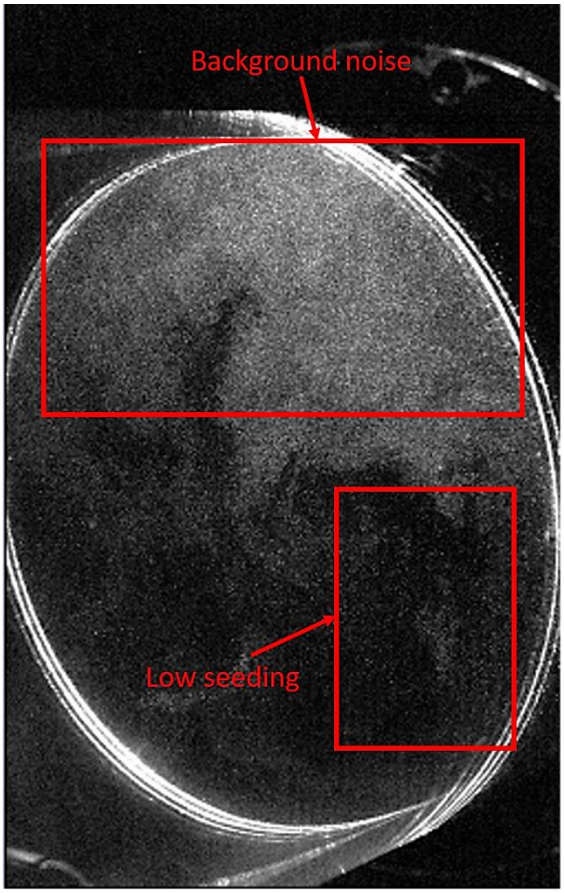

Figure 3-16: Example of raw image. The background noise and low seeding regions are highlighted in red.

During the snapshots processing, some choices were taken bearing the three above considerations in mind.

First of all, prior the processing, the stereoscopic calibration needs to be implemented. According to Davis' manual *Imaging Tools* [38], the stereoscopic calibration allows to scale the results in units representing true dimensions, and to resolve the images and camera lens' distortions related to the perspective projection connected to the presence of curved glass. In addition, stereo measurements need an internal representation for the geometrical setup of both cameras relative to the sample. As for the camera calibration, three calibration planes were identified at 1.5 mm of distance, for a total of 3 mm.

To implement the stereoscopic camera calibration in *Davis 8.3.1* some choices were made. The experimental setup was set to "2 cameras mapping e.g. stereo", that is the camera setup to perform the calibration in case of an S-PIV experiment technique and a

2D calibration plate. It allows to extract 3D vectors by translating the images on a single plane [38]. A generic polynomial 3rd order function was selected as the mapping function, that is the ideal function to work with since the optical access to the fluid is blocked by the glass, that adds some extra distortion. To calibrate a volume with this function, at least two or more equidistant coplanar planes need to be used [38]. Therefore, three positions of the calibration plate were used, for a total of 6 images (three per camera). As before, the first view of the calibration plate was at $z = -1.5$, and the plate was moved twice of $1.5\ mm$, for a total covered area of $3\ mm$. The calibration plate used at this point had the same geometrical characteristics of the calibration plate used to calibrate the cameras. As output of the process, the mapping function provided the average deviation of the dewarped mark positions with respect to an ideal grid, together with an image where all the corrected images are overlapped at the plane $z = 0$, and it is possible to visually determine if the corrected images coincide. Figure 3-17 shows the image output for this work. The ideal grid is shown in red.

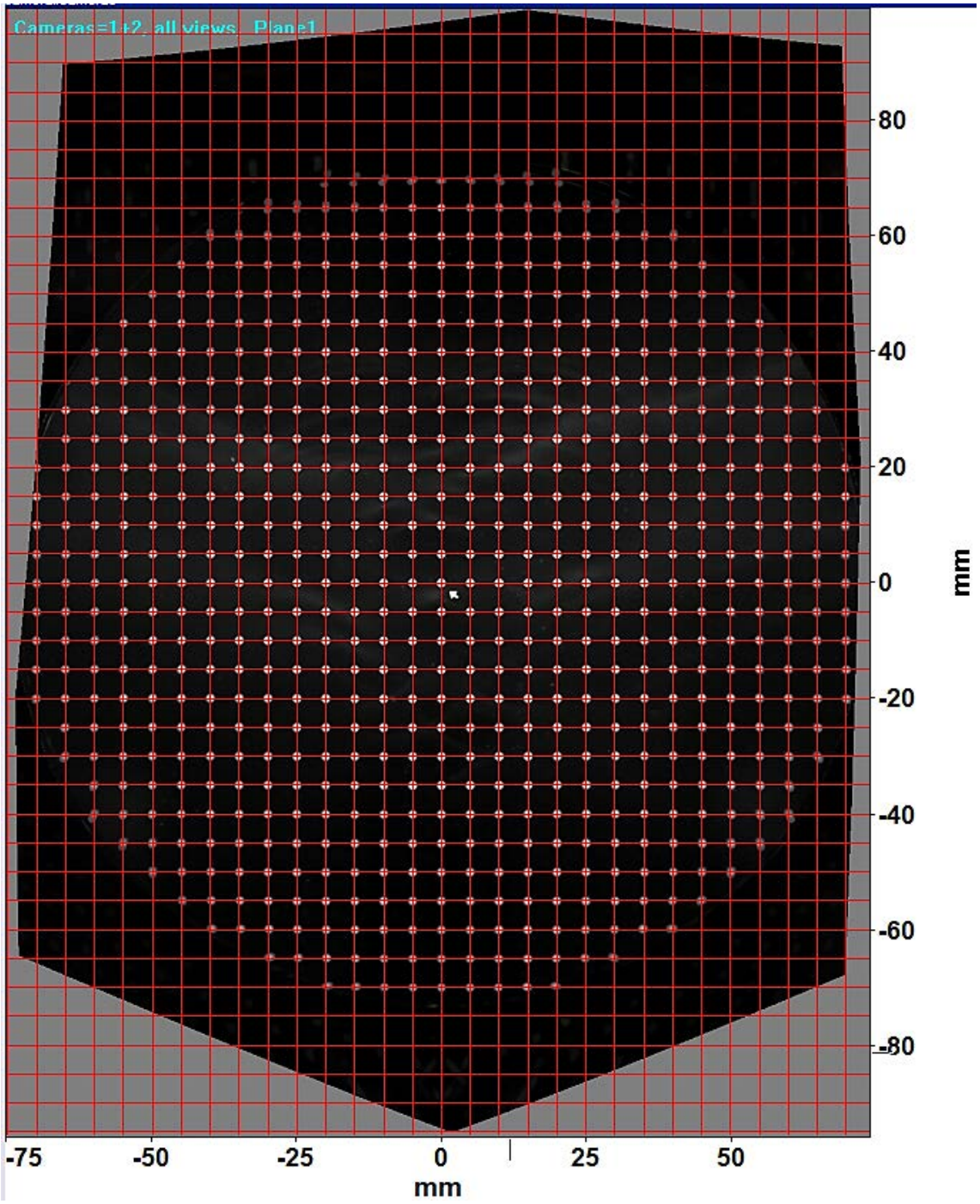

Figure 3-17: Corrected images plus ideal regular marks grid superimposition.

As a result, the general correction was satisfactory. Only in the upper part of the grid the images correction was less accurate (Figure 3-18), and this was almost certainly due to the fact that the cameras were tilted, and there was more glass to go through, therefore more distortion.

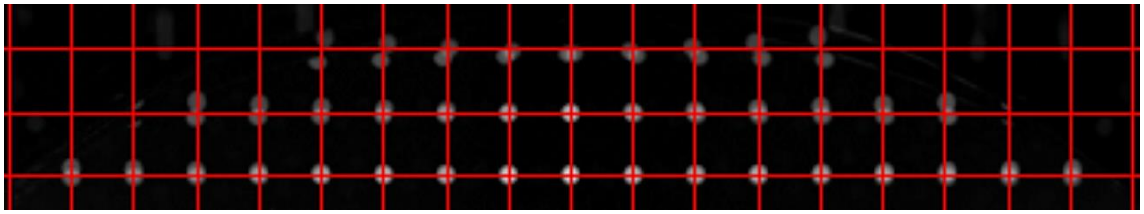

Figure 3-18: Corrected images plus ideal regular marks grid superimposition particular.

3.3.3 Self-calibration

In the experimental setup, it might happen that the calibration plate is not perfectly aligned with the light sheet, with the risk to have a bias in the final velocity field [32]. Therefore, prior the real images processing and after the stereoscopic calibration, the self-calibration was done. The process relies on the iterative applications of calibration polynomials to eliminate the errors due to the misalignment of the calibration plate and the light sheet. If some misalignment is found, the self-calibration process provides a disparity map which represents the relative displacement between the two objects. The displacement can therefore be reduced increasing the number of the process iterations. If the cameras are perfectly aligned, no disparity vector is present (Figure 3-19). The basic assumption to judge the quality of the image correction is that images taken at the same time instant by both cameras should have the same information, therefore no displacement.

The self-calibration is done in three main steps:

- Set up initial disparity map
- Calculate disparity map/update calibration
- Refine new calibration

For this work, interrogation windows of $128x128$ pixels were used in the process, with a window overlap of 50%. According to Davis' manual, these values are quite standard, and work for most of the applications [32]. Since the bigger the image range the better the fit of the camera calibration into the light sheet [32], the entire image range of snapshots ($20{,}000$) was selected for the process.

For the calculation of the disparity map, Davis' 'sum of correlation' method [32] was implemented, that first calculates a correlation map for each image pair, and later sums al

the correlation maps in a final map, from which the disparity vectors are calculated. The method was selected since, according to the manual [32], this is the most robust method against noise, and in general it provides better results. Three iterations were performed to obtain a satisfactory self-calibration (Figure 3-20).

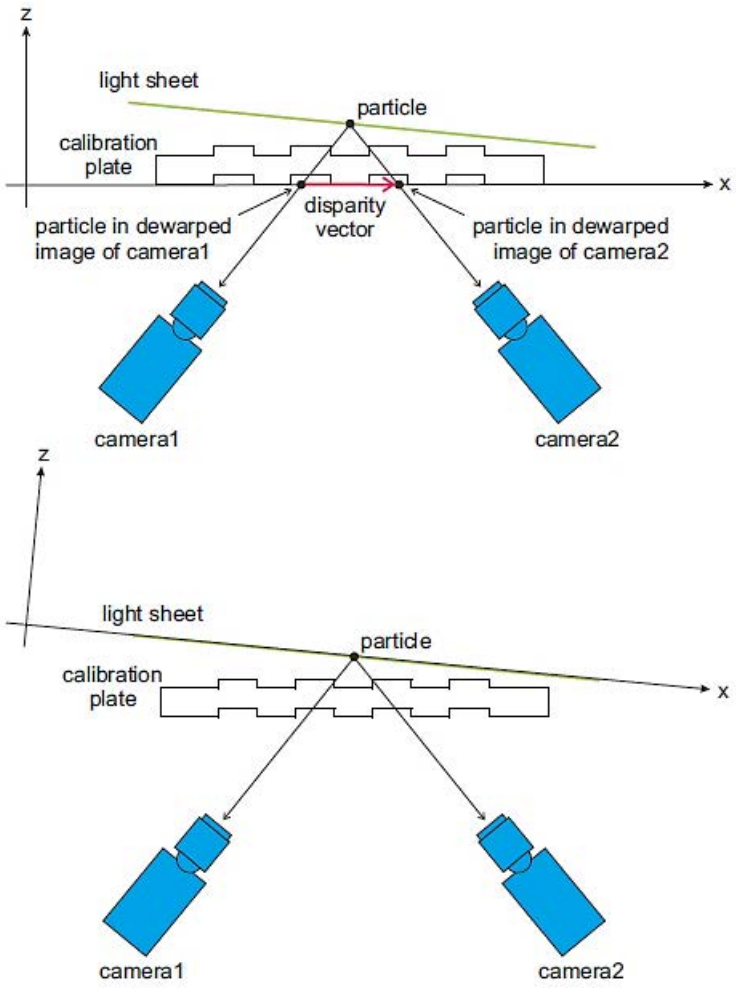

Figure 3-19: Self-calibration of the cameras.

In the image above, the laser light sheet and the calibration plate are not aligned. If the dewarping is done at z=0 position, the particle is mapped in different positions for the two cameras, and the difference is the disparity vector. The image below shows instead a perfect alignment between the calibration plate and the laser sheet, with no presence of the disparity vector [32].

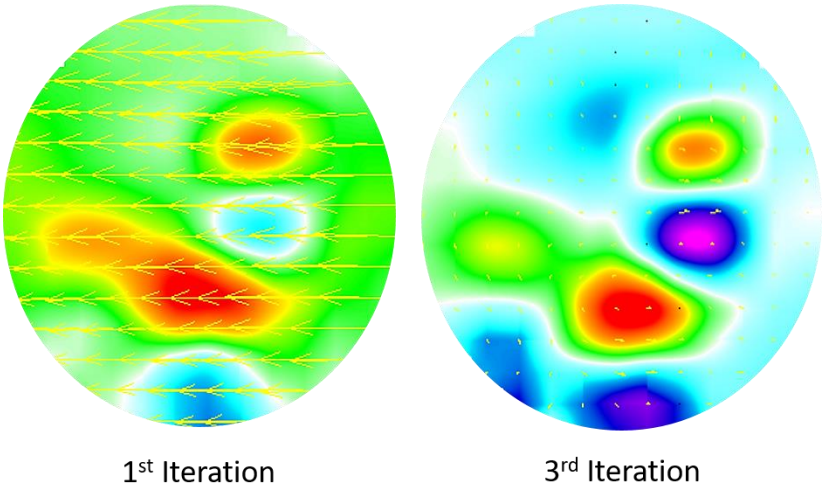

Figure 3-20: Self-calibration, comparison between the first and the third iteration.

In Figure 3-21 the velocity vectors' displacement is depicted in yellow. The colour scale represents the out-of-plane vorticity [s]. The vorticity range goes from $-\mathbf{0.05}$ to $\mathbf{0.05}$ for the first iteration, and from $-\mathbf{0.035}$ to $\mathbf{0.035}$ for the third.

Table 3-6: Self calibration iterations and respective calculated parameters.

Parameter	1st Iteration	2nd Iteration	3rd Iteration
Computed average disparity	4.4989 mm (31.656 px.)	0.1979 mm (1.3928 px)	0.1966 mm (1.3833 px)
Allowed residual triangulation error	Of 1 pixel: 29%	Of 2 pixels: 3%	Of 2 pixels: 3%
Rotation angle x-axis (deg)	-0.6299	-0.0108	-0.0027
Rotation angle y-axis (deg)	-0.1975	-0.0127	0.0009
Translation in z-direction (mm)	2.7487	0.0017	0.0001
Average deviation from plane (px)	0.9007 px. (0.1279 mm)	0.7813 px. (0.1110 mm)	0.7842 px. (0.1115 mm)
Average deviation (px)	0.0158	0.0004	9.88 e-005

3.3.4 Processing

For the processing to be implemented software *Davis 8.3.1* was used, and a new processing tree was defined. New settings were tested and compared with those previously used for the measurements taken with the Cranfield facility. More details can be found in Appendix A.1. The average filter was chosen as the best filter to be applied to the dataset. The average background intensity was first calculated in the entire range of $20{,}000$ images, and later subtracted before the calculation of the cross-correlation. The vector calculation was done in double frames. A sliding background with a scale length of two pixel was used to pre-process the images before the vector calculation. After the vector pre-processing and before the cross-correlation, the common region of both cameras was manually delimited with the use of a geometric polygonal mask, defined and applied to the entire range of images. The processing algorithm was based on a GPU cross-correlation method, applied to the masked source of data coming from the cameras. Since the correlation mode to utilize depends on the camera mode during the experimental acquisition, the stereo cross-correlation mode was selected for this work. The stereo cross-correlation was applied with multi-pass decreasing windows' size. To find out the ideal windows' size, overlap and number of passes for this experiment, comparative studies were performed (see Appendix A.1). Consequently, the total number of passes was set to 7, and no weighting function was applied. For the first window pass, a window size of $128x128$ pixels, with 50% overlap and a maximum shift of 4 pixels was used, where maximum shift defines the sized in pixel unit of the resulting correlation function, in which the peak of the correlation is searched [32]. For the second pass, a window of $64x64$ pixels, an overlap of 50% and a maximum change in shift of 3 pixels was chosen. For the third, fourth and fifth pass, a window of $32x32$ pixels with an overlap of 50% was used, and the maximum change in shift was set to 3 pixels. For the image reconstruction, the initial window shift was set constant, and the maximum reconstruction error for the 3D vector validation was chosen to be equal to three pixels. A multi-pass postprocessing was used to validate each vector field before it was used as a reference for the next pass. During the procedure, spurious vectors were removed with a threshold value bigger than twice the standard deviation of the neighbour vectors. At the same time, the spaces left by the removed vectors through a data interpolation, and a smoothing with a $3x3$ filter was used. After the vector field was calculated, the real vector postprocessing

took place. First, a range was defined to restrict the vectors to filter, and the vectors outside the range were deleted. For this work, the range was between 0 and 20 pixels for the three velocity components. Subsequently, vectors with a peak ratio $Q < 1.2$ were deleted. As a third postprocessing step, a median filter was applied. The threshold for the vector removal was set twice the standard deviation. After the median filter was applied, the group of vectors with less than 5 vectors were removed, and the empty spaces filled up with interpolated vectors. Finally, the final vector field was smoothened by a $3x3$ smoothing filter to further reduce the noise. As already mentioned, the final spatial resolution for this work was of $2.1x2.1\ mm(0.14D_{AIP})$.

4 RESULTS AND DISCUSSION

In this chapter, the unsteady flow distortion at the Aerodynamic Interface Plane (AIP) of a high-offset S-duct is analysed, based on measurements taken with the Stereoscopic Particle Image Velocimetry technique. During the flow measurements, a distortion screen was used to simulate the ingestion of a boundary layer profile with a thickness of $\delta/D_{in} = 0.336$, a profile similar to the one studied by Giuliani [9]. Five different locations of the distortion screen were tested, to quantify the impact of the boundary layer ingestion on the flow distortion characteristics at the S-duct exit. One additional case was tested without the distortion screen presence, to be used as a reference case. For the reference case (baseline) a boundary layer caused by the friction of the flow with the S-duct wall of $\delta/D_{in} = 0.04$ thickness was considered. The value was calculated by Gil-Prieto in the same facility and for the same S-duct with the aid of total pressure measurements based on a traversing flattened boundary-layer Pitot probe [33]. The flow condition was set to $M_{ref} = 0.27$, and 20'000 flow snapshots were taken per case to ensure a statistically converged sample. The time-averaged and standard deviation results are first introduced and discussed, to identify the main characteristics of the unsteady flow field at the AIP. The unsteady swirl distortion is later investigated with the use of the distortion descriptors provided by the Society of Automotive Engineers (SAE). The main steady and unsteady swirl distortion characteristics are first studied through a comparison of the area-averaged swirl distortion metrics. Subsequently, the swirl intensity swirl distortion descriptor is investigated at different radial positions. Finally, the most common and rare swirl patterns are identified at different radial positions, as well as the patterns that promote the highest levels of swirl intensity.

During the results discussion, two aspects are considered: the raw data collected during the experiment show a region of low seeding at the bottom right of the AIP (Figure 3-16), which might result in not reliable levels of velocity and unsteadiness components locally. Even though the problem was partially mitigated through the processing performed with the software *Davis 8.3*, locally noisy results are still evident in the affected region. The second aspect to be considered is that some mis-calculated vector maps were found in the dataset after the processing. The problem, already experienced in past experiments performed in the same facility, is connected to the laser timing stabiliser device, which is

part of the time-resolved PIV system. Due to the device malfunctioning greater particle displacements are detected, hence the values of axial velocity and standard deviation increase in the mis-calculated vector maps. Figure 4-1 shows a comparison between a snapshot (a) with normal values of axial velocity and a mis-calculated vector map (b) in which the levels of out-of-plane velocity are higher, due to the malfunctioning of the laser timing stabiliser device.

Table 4-1 reports the percentage of distorted snapshots for each studied case. The discussion that follows will be made considering both aspects: on one side, the region that corresponds to the low seeding area will be ignored; on the other side, higher values of axial velocity and relative unsteadiness are expected, due to the presence of the mis-calculated vector maps in the dataset. In particular,

Table 4-1 clearly indicates that the higher the percentage of mis-calculated vector maps per case, causes the area-averaged, time-averaged out of plane magnitude w_{ref} to slightly increase.

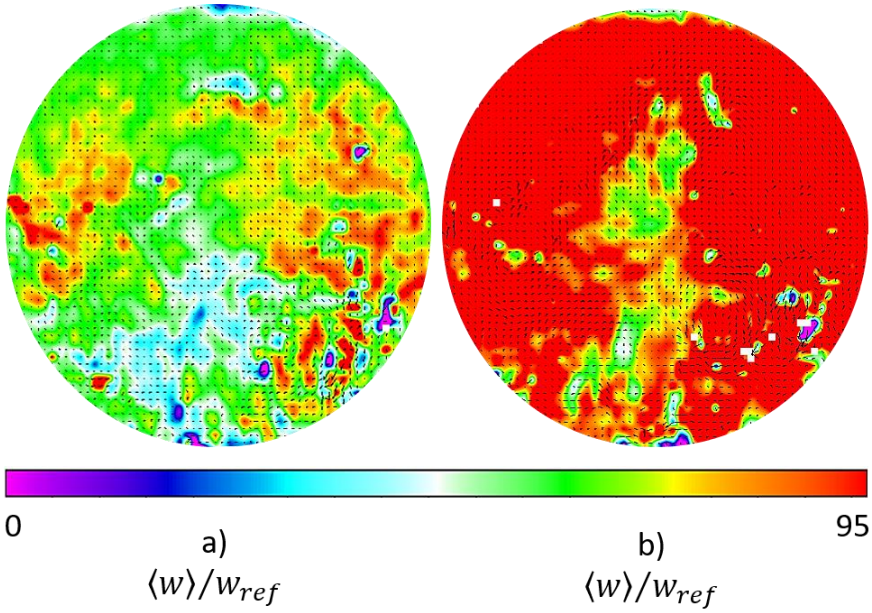

Figure 4-1: Example of normal (a) and mis-calculated (b) vector maps, baseline case.

Table 4-1: Percentage of mis-calculated vector maps and relative axial velocity calculated over the entire range of 20000 images for each case.

Case	Percentage of mis-calculated vector maps	Area-averaged time-averaged out-of-plane reference velocity (w_{ref})
Baseline	4.37	$w_{ref} = 63.391$
Distortion screen at $\theta = 0°$	8.22	$w_{ref} = 62.374$
Distortion screen at $\theta = 45°$	14.59	$w_{ref} = 64.756$
Distortion screen at $\theta = 90°$	6.13	$w_{ref} = 61.732$
Distortion screen at $\theta = 135°$	12.91	$w_{ref} = 64.837$
Distortion screen at $\theta = 180°$	18.44	$w_{ref} = 66.279$

While in the baseline and in the cases with BL ingestion at $\theta = 0°$ and $90°$ the percentages of mis-calculated vector maps are acceptable, in the other cases the percentages shown in Table 4-1 are quite high, and particularly distorted peak values of unsteadiness and axial velocity are expected. However, since all the cases are affected by the problem, a quite reliable comparison can be carried out in this work. Despite the presence of the lower percentage of mis-calculated vector maps, increased values of out-of-plane velocity and standard deviation are instead expected in the baseline case when compared to the findings of previous works.

4.1 Flow field at the Aerodynamic Interface Plane

4.1.1 Time-averaged flow field

First, the time-averaged distributions of the velocity components and swirl angle at the S-duct exit plane are examined, to identify the main characteristics of the velocity flow field. The data presented were first processed with the software *Davis 8.3*, and then post-processed with *CUData-PRO*. Finally, they were plotted with the software *TecPlot*. Since

the data near the duct wall are usually spurious due to light reflections and seeding oil accumulation, the data at $^{r}/_{R_{AIP}} > 0.90$ have been removed to avoid unwanted effects on the final results. The duct wall is indicated with a solid black circle. The test matrix is shown in Table 3-2. A comparison between the baseline and the case with ingestion of a boundary layer of $\delta/D_{in} = 0.336$ thickness at $\theta = 0°$ is first introduced, to highlight the effect of the boundary layer ingestion on the flow distortion. Subsequently, the same analysis is applied to all the other cases, to investigate the effect of the boundary layer ingestion at different duct inlet locations. All time-averaged values presented in the section are non-dimensionalized by a reference area-averaged time-averaged out-of-plane velocity calculated at the AIP (Equation 4-1), where A is the masked area defined during the data processing in Davis 8.3 and ω is the axial velocity at a certain position (r, θ polar coordinates) and time (where t=0 corresponds to the first snapshot, and with a time difference of $\Delta t = 2.5 * 10^{-4} s$ between each snapshot).

$$\boldsymbol{w_{ref} = \frac{1}{A}\int_A \langle \omega(r,\theta,t)\rangle \, dA} \qquad \textbf{(4-1)}$$

The reference out-of-plane velocity values for each studied case are reported in

Table 4-1.

4.1.1.1 Baseline and $\delta/D_{in} = 0.336$ with $\theta = 0°$ case time-averaged flow field comparison

The flow field at the AIP of embedded or semi-embedded engines is characterised by a region of main loss in the central-lower part of the cross-sectional area. This is shown in Figure 4-2a and Figure 4-2e, considering as in all the other cases a-h that only the data at $^{r}/_{R_{AIP}} < 0.90$ are shown, and the S-duct wall is indicated with a solid circle. The extent shown by the baseline case, with values of approximately $\langle w\rangle/\langle \overline{w}\rangle_{ref} = 0.827$, matches with the results provided by previous studies ([4], [25], [34], [39]), and it is typical of high-offset ducts. The increased area of loss associated with low axial velocities is a consequence of both stronger secondary flows, typical of the high-offset configuration, and greater duct curvature, that is responsible for the flow separation in the inner side of the duct. The high-offset duct secondary flows are also responsible for a shift of the loss region from the bottom of the AIP to a more central location, as studied by Zachos, P. et

al. (2016) [4] and confirmed in Figure 4-2a. The results shown are important, since both the conventional flow distortion descriptors and the compression systems depend on the radial position of the flow distortion [7]. In the case with boundary layer ingestion at $\theta = 0°$ the loss region appears in a more extended region, that covers both the centre and the lower part of the AIP, with low magnitudes of axial velocities as low as $\langle w \rangle / w_{ref} = 0.652$. The presence of the boundary layer ingestion therefore affects the axial velocity magnitude, with presence of lower values in the loss region and higher values in the freestream zone. A small secondary loss region is noticeable near the wall at the top of the AIP in both Figure 4-2a and Figure 4-2e, with values as low as $\langle w \rangle / w_{ref} = 0.569$ and 0.481 in the baseline and in the case with BLI at $\theta = 0°$ respectively. Above the loss region, a freestream zone characterised by high values of out-of-plane velocity is observed in both Figure 4-2a and Figure 4-2e. The pattern, mainly concentrated in the upper part of the cross-sectional area, is symmetrical in both cases. While in the baseline case the maximum values are of about $\langle w \rangle / \langle \overline{w} \rangle_{ref} = 1.18$, in the boundary layer ingestion case the peak values are spread in a wider area, and reach values of $\langle w \rangle / \langle \overline{w} \rangle_{ref} = 1.337$. To ensure the desired boundary conditions downstream of the distortion screen, the compressor is operated at a higher speed, to overcome the increased pressure loss introduced by the distortion screen. The upper part of the AIP, that coincides with the freestream area of the boundary layer created by the distortion screen, is subsequently characterized by higher magnitudes and a wider distribution of axial velocities with respect to the baseline case. The curved geometry of the intake is also responsible for the presence of in-plane secondary flows (Figure 4-2b, Figure 4-2c, Figure 4-2f, Figure 4-2g).

With respect to the baseline case, the ingestion of boundary layer stresses both the pattern and the range of the horizontal velocity at the bottom of the AIP, with values as low as $\langle u \rangle / \langle \overline{w} \rangle_{ref} = -0.145$ in the bottom right region and as high as $\langle u \rangle / \langle \overline{w} \rangle_{ref} = 0.201$ in the bottom left region. For the baseline case the values are $\langle u \rangle / \langle \overline{w} \rangle_{ref} = -0.109$ and $\langle u \rangle / \langle \overline{w} \rangle_{ref} = 0.116$ respectively.

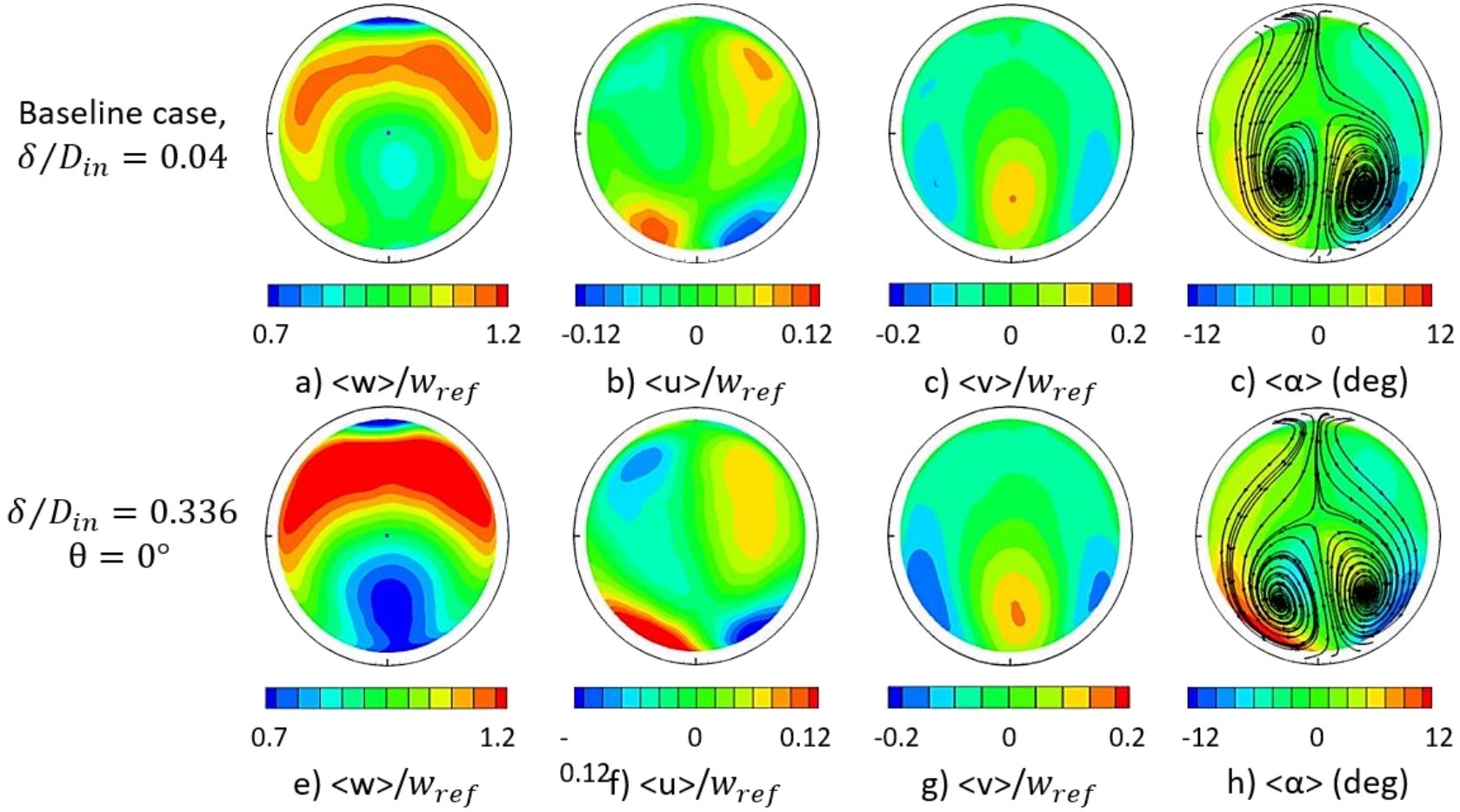

Figure 4-2: Time averaged flow field at the AIP, baseline (top) and $\delta/D_{in} = 0.336$ with $\theta = 0°$ (bottom) cases.

Moreover, the case with the distortion screen at $\theta = 0°$ also shows a wider region of lower axial velocities in the upper left region (Figure 4-2f) and lower high horizontal velocities at the top-right (Figure 4-2b). Since the AIP is positioned near the exit of the S-duct, the flow field is still affected by the duct curvature. The downward pitch of the flow is evident in the antisymmetric distribution of the horizontal velocity, in both cases. The time-averaged vertical velocity is shown in Figure 4-2c and Figure 4-2g. Although the BLI case shows areas of lower values especially at the bottom left of the AIP, the velocity distributions in the two cases are generally similar. For the case with boundary layer ingestion, the minimum values of vertical velocity are about $\langle v \rangle / \langle \overline{w} \rangle_{ref} = -0.195$, while they are of $\langle v \rangle / \langle \overline{w} \rangle_{ref} = -0.15$ in the baseline case. The secondary flows are consequently stronger if a thicker boundary layer flow profile is ingested, which results in stronger swirl angles. In both Figure 4-2d and Figure 4-2h an approximately symmetric twin swirl pair patterns is evident, despite in the BL ingestion case the tendency to move towards a bulk swirl pattern is observed . Compared to the baseline case, where the swirl range is in the range of $\langle \alpha \rangle (deg) = -8.8 \div +7.5$, both the magnitude and the extent of the swirling regions are enhanced by the ingestion of BLI, with magnitudes of $\langle \alpha \rangle (deg) = -11.5 \div 14.6$. Due to the use of a high-offset duct, the downward pitching flow is not only confined to the lower region of the AIP, but it is extended to the upper region [4].

Overall, the results obtained confirm that higher distortion levels are to be expected with the use of a high-offset duct, in line with the previous study carried out by Zachos [4]. The comparison between the baseline and the case with a $\partial / D_{in} = 0.336$ thick BL ingestion at $\theta = 0°$ shows that even more distortion is generated at the AIP with the ingestion of a thick boundary layer. This results in a greater and wider area of loss in terms of axial velocity distributed not only in the centre, but also at the AIP bottom. Moreover, higher peaks of axial velocities in more extended areas, as well as lower values of out-of-plane velocity in the secondary loss region are observed. The ingestion of boundary layer also enhances in-plane velocities, with lower magnitudes in the vertical component and higher and lower values of horizontal velocity. The stronger secondary flows do not affect the swirl pattern, that still presents a pair of twin swirls, but result in increased swirl angles and swirling regions. Despite the presence of mis-calculated vector

maps connected to the faulty laser timing stabilizer device, the results found for the baseline case are in good accordance with previous studies that took place in the same facility, with the same reference Mach number $M_{ref} = 0.27$ and S-duct geometry [4], [33], [40].

4.1.1.2 Time averaged flow field comparison between the cases with $\delta/D_{in} = 0.336$ and screen rotation of $\theta = 45°, 90°, 135°$ and $180°$

The comparison between the cases with the distortion screen rotated by different angles enables to understand how the ingestion of boundary layer at different inlet locations affects the flow field distortion at the AIP and consequently the downstream machine. Figure 4-3 shows the time-averaged results of the cases with ingestion of a $\partial/D_{in} = 0.336$ thick boundary layer at $\theta = 45°, 90°, 135°$ and $180°$, with θ being the clockwise angle between the vertical axis of symmetry of the duct inlet plane and the local y axis of symmetry of the distortion screen, as seen from a downstream point of view (Section 3.1.4). As previously, only the data at $r/R_{AIP} < 0.90$ are reported, and the S-duct wall is indicated with a solid circle. Figure 4-3 shows that the ingestion of boundary layer at different inlet positions modifies both the distortion levels and the flow pattern at the S-duct exit. The region of main loss in the central-lower part of the AIP, associated with low axial velocities, can be identified in all the cases (Figure 4-3a, Figure 4-3b, Figure 4-3c, Figure 4-3d), but with some differences. As the boundary layer ingestion region moves in the clockwise direction, from small to high values of θ, the loss region tends to shift toward the right-central area, with axial values as low as $\langle w \rangle / \langle \overline{w} \rangle_{ref} = 0.8$ in the case with ingestion at $\theta = 45°$. At $\theta = 90°$ location, the tendency inverts, and the loss region spreads from the central area to the bottom-right region near the wall, with the minimum deficit in axial velocity of about $\langle w \rangle / \langle \overline{w} \rangle_{ref} = 0.758$ for the ingestion at $\theta = 135°$. The small secondary loss region, still present in the case with the distortion screen placed at $\theta = 45°$, disappears progressively when the BL ingestion region approaches the upper part of the AIP. A quite different case is represented by the ingestion of boundary layer at $\theta = 180°$. In Figure 4-3d the loss region is consistently reduced, with values of about $\langle w \rangle / \langle \overline{w} \rangle_{ref} = 0.882$, and it is concentrated in the central area of the AIP. The secondary loss region is instead enhanced, with values as low as $\langle w \rangle / \langle \overline{w} \rangle_{ref} = 0.491$. Such low values are expected since the two phenomena of thick boundary layer ingestion

and secondary loss region are superimposed. In general, the loss region, characterized by a deficit in axial velocity, appears in the same area of the boundary layer presence when the ingestion is along the vertical axis of symmetry (Figure 4-2a, d and Figure 4-3d), but tends to move in the opposite side of the boundary layer ingestion location for the other studied cases. Moreover, the case with BL ingestion at $\theta = 180°$ shows the presence of two distinct areas of high out-of-plane velocity confined near the duct wall, at each side of the central loss region, while in all the other cases the high axial velocity values are observed in the more classical pattern above the region of loss. Despite the different locations of boundary layer ingestion along the wall of the duct inlet, the high axial velocity values are generally concentrated in the upper region of the AIP, while the loss region is concentrated in the central-bottom area for all the studied cases. The patterns and the ranges of the secondary flows are also affected by the ingestion of a thick boundary layer. Figure 4-3e, f and g are an example. High values of lateral velocities are found near the wall, at the AIP bottom, with maximum values of $\langle u \rangle / \langle \overline{w} \rangle_{ref} = 0.362, 0.316 \text{ and } 0.271$ for the cases with BL ingestion at $\theta = 45°, 90° \text{ and } 135°$ respectively. The values are up to three times higher than in the baseline case. In contrast, the secondary region of high lateral velocities in the upper-left area reduces consistently. The variation in BL ingestion location also affects the deficit area of horizontal velocity at the AIP bottom, which moves from an area near the wall at the bottom-right towards the AIP centre, uniting with the other region of low velocity located at the upper-left of the AIP. Again, the tendency inverts after the case with BLI at $\theta = 45°$, and a similar pattern to the baseline case is shown in Figure 4-3h.

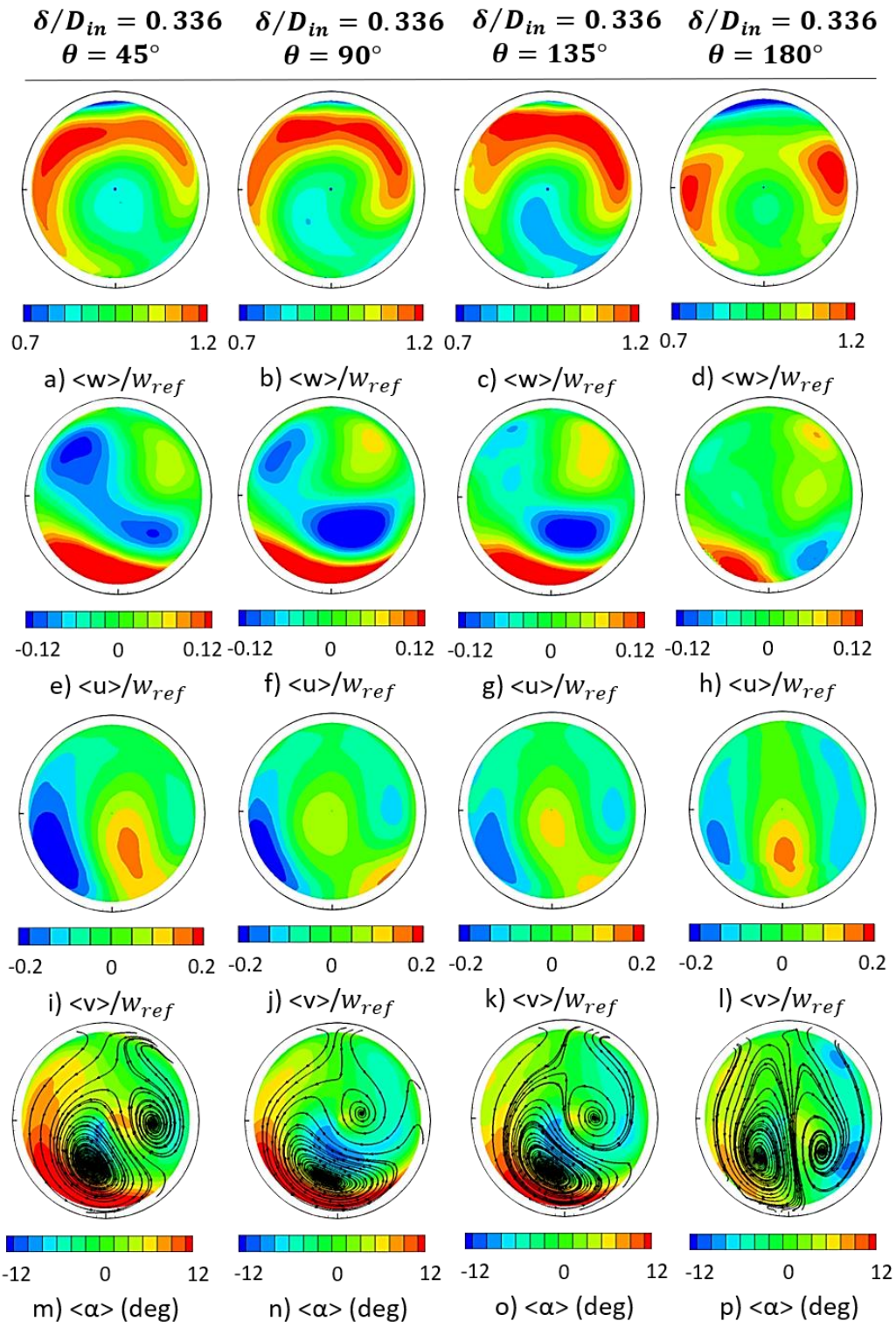

Figure 4-3: Time-averaged flow field at the AIP for the cases with the ingestion of a boundary layer of $\delta/D_{in} = 0.336$ thickness at $\theta = 45°, 90°, 135°$ and $180°$.

The lowest values of horizontal velocities are reached in the case with BL ingestion at $\theta = 90°$, where values as low as $\langle u \rangle / \langle \overline{w} \rangle_{ref} = -0.193$ are observed in the central-right area. The antisymmetric distribution of the secondary flows typical of the baseline case and the cases with BL ingestion along the vertical axis of symmetry is therefore lost as the region of BL ingestion moves. Finally, coherently with what was observed in Section 4.1.1.1, the change in BLI ingestion location enhances the formation of a deficit area of vertical velocities on the left side of the AIP. Again, the phenomenon reaches its apex for the case with BL ingestion at $\theta = 45°$, with minimum values of about $\langle v \rangle / \langle \overline{w} \rangle_{ref} = -0.273$. The magnitudes of the high vertical velocities are also affected and while the pattern at the central-bottom part of the AIP is approximately maintained also in the case of BLI at $\theta = 45°$, with the highest peak values of about $\langle v \rangle / \langle \overline{w} \rangle_{ref} = 0.167$, it changes in Figure 4-3j and in Figure 4-3k. In the two cases with boundary layer ingestion at $\theta = 90°$ and $135°$ the values of vertical velocities sink to $\langle v \rangle / \langle \overline{w} \rangle_{ref} = 0.158$ and 0.123 respectively, with the pattern that divides into two areas, one located in the AIP centre and one in its bottom-left region. As expected, the presence of such distorted and strong secondary flows results in strong swirling regions. While in the case with BL ingestion at $\theta = 180°$ the common twin swirl pair is observed (Figure 4-3p), in Figure 4-3m a bulk swirl pattern dominates, with swirl angles up to $\langle \alpha \rangle (deg) = 20.3°$. The presence of a non-symmetrical swirl pair is observed also in the cases with BL ingestion at $\theta = 90°$ and $135°$, with maximum swirl angles up to $18.568°$ and $17.412°$ respectively.

Overall, the ingestion of a thick boundary layer greatly affects the flow distortion if the location is outside the vertical axis of symmetry, both in terms of peak values and distortion patterns. For the cases with BL ingestion at $\theta = 0°$ and $180°$ the same behaviour is observed in the out-of-plane velocity distribution for the cases, while only the ranges of the secondary flows and swirl angles are affected, not the patterns. The observed trends are that the deficit in out of plane velocity tends to concentrate in the opposite area of the BL ingestion, with a shift towards the central area that inverts after the BLI location at $\theta = 45°$. The same trend is shown by the region of low horizontal velocities and the secondary flows are generally enhanced, with a deficit of vertical velocity on the left of the AIP, and intense regions of high horizontal velocities near the wall at the AIP bottom. Compared to the baseline, strong swirling regions appear, with

increased swirl angles and patterns that tend toward bulk swirl pairs. An exception to the general trend is represented by the cases with BL ingestion along the vertical axis of symmetry, where no particular changes in the in-plane velocities and swirling regions patterns are observed.

The area-averaged values of time-averaged distributions have also been calculated and reported in Table 4-2. Due to the faulty laser timing stabiliser device, the averaged values of axial velocity and relative standard deviation are not considered completely reliable.

Table 4-2: Area-averaged values of the flow field axial velocity and swirl angle at the AIP.

	$\langle w \rangle / \langle \overline{w} \rangle_{ref}$	std$\langle w \rangle / \langle \overline{w} \rangle_{ref}$	$\langle \alpha \rangle (deg)$	std$\langle \alpha \rangle (deg)$
Baseline	63.391	0.211	0.085	9.324
Distortion screen at $\theta = 0°$	62.374	0.271	0.523	11.104
Distortion screen at $\theta = 45°$	64.756	0.299	4.210	11.466
Distortion screen at $\theta = 90°$	61.732	0.231	2.267	9.579
Distortion screen at $\theta = 135°$	64.837	0.271	1.983	8.796
Distortion screen at $\theta = 180°$	66.279	0.303	-0.068	11.183

It is worth mentioning that the time-averaged results of the flow unsteadiness do not reveal how complex and unsteady the flow field is. Figure 4-4 provides an example of some consecutive sample snapshots of the out-of-plane velocity extracted from the baseline case before the time-averaging process. Substantial variations can be noticed in the flow field in a time period of only 0.001 s. This also highlights the limitations of the conventional 40-probe rake method usually used to measure the flow distortion, that become even more evident for the measurement of the unsteady variations of the swirl angle, for which fewer probes are used. Overall, the substantial changes in the flow field

showed in Figure 4-4 confirm that usual AIP measurement techniques based on probe pressure rakes are insufficient to capture the nature of the flow.

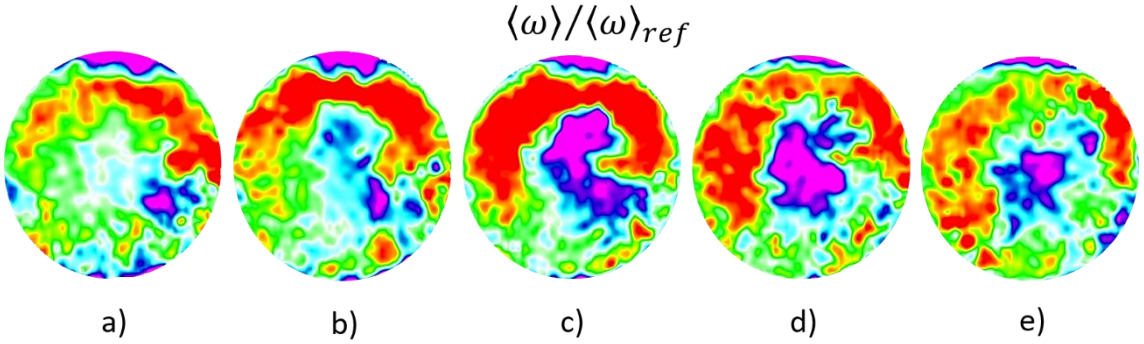

Figure 4-4: Consecutive snapshots of the out-of-plane velocity at the AIP taken from the baseline case. The five snapshots correspond to a time period of 0.001 s.

4.1.2 Fluctuating flow field

One of the concerns in the assessment of intake flow distortion is that there is still limited knowledge in the field of unsteady characteristics of the distortion metrics and the nature of the unsteadiness in the velocity field. To study the main unsteady characteristics of the flow, the distribution of the standard deviation at the AIP was computed for the three velocity components and the swirl angle. As for the time-averaged results, the unsteady data presented in Figure 4-5 and Figure 4-6 were first processed with the software *Davis 8.3*, and then post-processed with *CUData-PRO*. Finally, they were plotted with the software *Tecplot*. In the Figures, the data at a radial position of $^{r}/_{R_{AIP}} > 0.90$ were removed to avoid incorrect results due to light reflections and seeding oil accumulation typical of the areas near the duct wall, indicated with a solid black circle. The region of low seeding is particularly evident in the unsteady results and it is characterized by high levels of distortion. In Figure 4-5 and Figure 4-6, the region is indicated by a dashed circle in the bottom-right region, and since the data in the area are not reliable they are not considered in the discussion. Finally, it is worth mentioning that high levels of unsteadiness are expected, since a high-offset duct is used [4] and as a consequence of the increased spatial resolution of the cameras used in portrait mode, that for this work is of $2.1x2.1mm$. On the other hand, increased levels of unsteadiness, especially in the out-of-plane velocity component, are connected to the presence of mis-calculated vector maps

caused by the faulty laser timing stabiliser device (Table 4-1). Nevertheless, since all the datasets are affected by the problem, a quite reliable comparison can be performed. As for the time-averaged results, a first comparison is made between the baseline case and the case with boundary layer ingestion at $\theta = 0°$, to highlight the effect on the fluctuating flow field at the AIP caused by the ingestion of a thick boundary layer. A comparison between the cases with BL ingestion at different S-duct inlet locations follows.

4.1.2.1 Unsteady flow field comparison, baseline and $\delta/D_{in} = 0.336$ BLI at $\theta = 0°$

To identify the main unsteady characteristics of the flow field connected to the ingestion of boundary layer, the standard deviation of the flow field at the AIP between the baseline and the case with boundary layer ingestion at $\theta = 0°$ is first investigated. In both cases, high levels of unsteadiness are concentrated in the upper region of the AIP (Figure 4-5a and Figure 4-5e), in an area that approximately coincides with the region of high time-averaged axial velocity values (Figure 4-2). Compared to Figure 4-5a, the levels of unsteadiness in case of boundary layer ingestion (Figure 4-5e) are wider and with extended peak values up to $std\langle\omega\rangle/\omega_{ref} = 0.317$, while in the baseline case the maximum values are about $std\langle\omega\rangle/\omega_{ref} = 0.237$. As envisioned, the values of unsteadiness of the baseline case are slightly higher than the results observed by Zachos et al [4] for the same reference inlet Mach number and S-duct geometry. The location of the region of high standard deviation values is instead quite unexpected. With the Low-Bandwidth Stereoscopic Particle Image Velocimetry technique applied on the same duct at a reference Mach number of 0.27, Gil-Prieto [32] observed a distribution of the out-of-plane velocity fluctuation located around the mean shear layer that delimits the main loss region observed in the correspondent time-averaged flow field. A result in between these results and the study of Gil-Prieto [33] is provided by Zachos et al. [4], where the same region was observed in a more central-upper area of the AIP, at the outer limit of the loss region. In this work instead, the region of the out-of-plane velocity fluctuation (Figure 4-5a and Figure 4-5e) is located above the loss region identified in the time-averaged results (Figure 4-2a, Figure 4-2d)), in an area that so far has been observed only at higher Mach numbers. Since this wide area is present also in the baseline case, its main cause cannot be connected to the boundary layer ingestion. A possible explanation is found in the simultaneous presence of mis-calculated vector maps and increased spatial resolution,

that are responsible for both higher velocity magnitudes and wider regions of peak values. The unsteady nondimensional in-plane velocity fluctuations $std\langle u\rangle/\omega_{ref}$ and $std\langle v\rangle/\omega_{ref}$ exhibit different characteristics. The boundary layer ingestion does not affect the peaks of the horizontal standard deviation values, that are similar in both cases, with values of about $std\langle u\rangle/\omega_{ref} = 0.225$. Despite this, the presence of BLI affects the unsteady pattern, and more extensive regions are shown in Figure 4-5f, with two additional lateral branches at the bottom of the AIP. The bottom-right branch appears also in the baseline case, but it is not considered since it corresponds to the low seeding region. Conversely, the ingestion of boundary layer slightly affects the peak values of the vertical flow fluctuations, that are positioned in the same area of the loss region highlighted in the time-averaged nondimensional ω velocity distribution (Figure 4-2). Accordingly to the time-averaged results, the peak values of the baseline case $std\langle v\rangle/\omega_{ref} = 0.226$ (Figure 4-5c) are distributed in a more central area than the case with boundary layer ingestion at $\theta = 0°$, where the presence of the BL increases the values of the vertical unsteadiness up to $std\langle v\rangle/\omega_{ref} = 0.241$. Generally, the in-plane unsteadiness is less affected by the presence of the boundary layer ingestion than the time-averaged results.

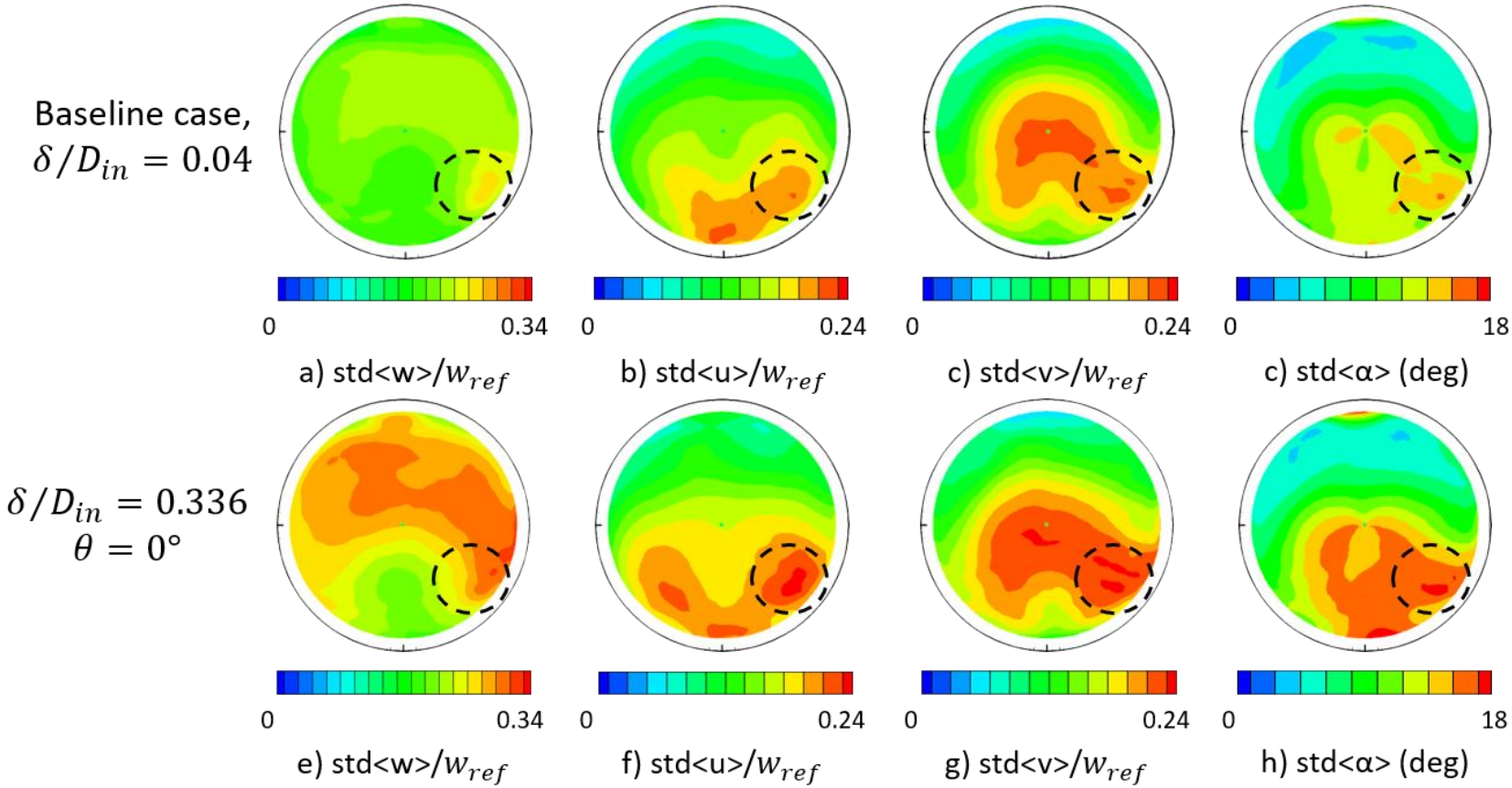

Figure 4-5: Standard deviation of the flow field at the AIP. Baseline (upper row) and $\delta/D_{in} = 0.336$ with $\theta = 0°$ (bottom row) case.

The peak values of the swirling regions are increased from approximately $std(\alpha)(deg) = 15°$ to 19° in case of BL ingestion, where wider regions of peak values can be observed (Figure 4-5h). In particular, peak areas of swirl angle unsteadiness are shown in a region in which the time-averaged distribution appears to be swirl-free. This highlights the importance of the unsteady analysis of the swirl distortion since steady measurements can indicate misleading conclusions. However, the top sector of the AIP remains mostly free of in-plane swirl angle fluctuations.

Unlike the values of the axial unsteady distribution, the other magnitudes observed in the baseline case are quite in line with the results found in previous experiments [4], [33], [40]. This confirms the idea that the increased levels of unsteadiness related to the axial velocity are caused by the presence of mis-calculated vector maps in the dataset.

Overall, the ingestion of boundary layer along the inlet vertical axis of symmetry affects the peaks of unsteadiness and widens the regions of peak value. This is observed mainly in the out-of-plane unsteadiness, that in this work is located at the top of the AIP, unlike past studied. The peaks of axial unsteadiness are also higher than expected and are probably connected to the presence of mis-calculated vector maps in the dataset. The pattern of the horizontal standard deviation is the main affected. Table 4-2 confirms the general tendency, with values of $\mathrm{std}\langle w\rangle/\langle\overline{w}\rangle_{ref}$ that increase from 0.211 to 0.271 in the baseline case and in case of ingestion of a thick BL at $\theta = 0°$, while the swirl angle unsteadiness $\mathrm{std}\langle\alpha\rangle(deg)$ varies from 9.3° to 11.1° respectively.

4.1.2.2 Unsteady flow field comparison, $\delta/D_{in} = 0.336$ thick BLI at $\theta = 45°, 90°, 135°$ and $180°$

The standard deviation of the flow field in the cases with BL ingestion at different inlet location is now analysed. As for the baseline case, also in Figure 4-6 the maximum values of the unsteady axial velocity distribution are concentrated in the same region of the time-averaged axial velocities (Figure 4-3). The high levels of out-of-plane standard deviation are surely connected to the presence of mis-calculated vector maps in the dataset, as already mentioned. The axial velocity fluctuations show the same pattern of the time-averaged out-of-plane velocity also in the case of BL ingestion at $\theta = 180°$, characterized by a region of loss at the top of the AIP and by two regions of high axial standard deviation

peaks at the lateral side of the AIP centre. Despite the area-averaged parameters of Table 4-2 suggest axial unsteadiness values higher than the baseline in all the cases with boundary layer ingestion, the results are not considered reliable. For the cases with BL ingestion at $\theta = 90°$ and $135°$ in fact lower local peak values of fluctuations are shown in all the three velocity components and swirl angle (Figure 4-6). As for the time-averaged results, both the patterns and the peak values of the secondary flow unsteady distributions change as the BLI location changes. The in-plane horizontal standard deviation distribution shows peaks of lateral unsteadiness located between the regions of high and low time-averaged horizontal velocities at the bottom of the AIP, as in Figure 4-3. Values as high as $std\langle u\rangle/w_{ref} = 0.263$ and 0.264 are observed for the BL ingestion cases at $\theta = 45°$ and $180°$, while the peaks fall to $std\langle u\rangle/w_{ref} = 0.218$ and 0.214 for the BL ingestion at $\theta = 90°$ and $135°$ respectively. As highlighted in Section 4.1.2.1, the pattern of the vertical unsteadiness is approximately equal to the region of the axial loss in the time-averaged axial velocity (Figure 4-3). Quite wide regions of peak values can be observed in both the cases with BLI at $\theta = 45°$ and $180°$, with values as high as $std\langle v\rangle/w_{ref} = 0.263$ and 0.257 respectively. A slightly more central-upper distribution can be observed in Figure 4-6i, while for the case with BLI ingestion at $\theta = 180°$ the area covered by the peaks of vertical unsteadiness is more extended than the respective time-averaged loss region, and no unsteadiness connected to the time-averaged secondary loss region at the top of the AIP is shown. As expected, the peak values of the vertical unsteadiness distribution fall in the cases with BL ingestion at $\theta = 90°$ and $135°$. Finally, despite the unsteadiness levels of the secondary flows are quite high, no particular effects on the peak values of the unsteady swirl angles are observed. Significant changes are instead observed in the swirl angle patterns in the cases with BL ingestion at $\theta = 90°$ and $135°$, where a bulk swirl configuration dominates over the classical pair of twin swirl.

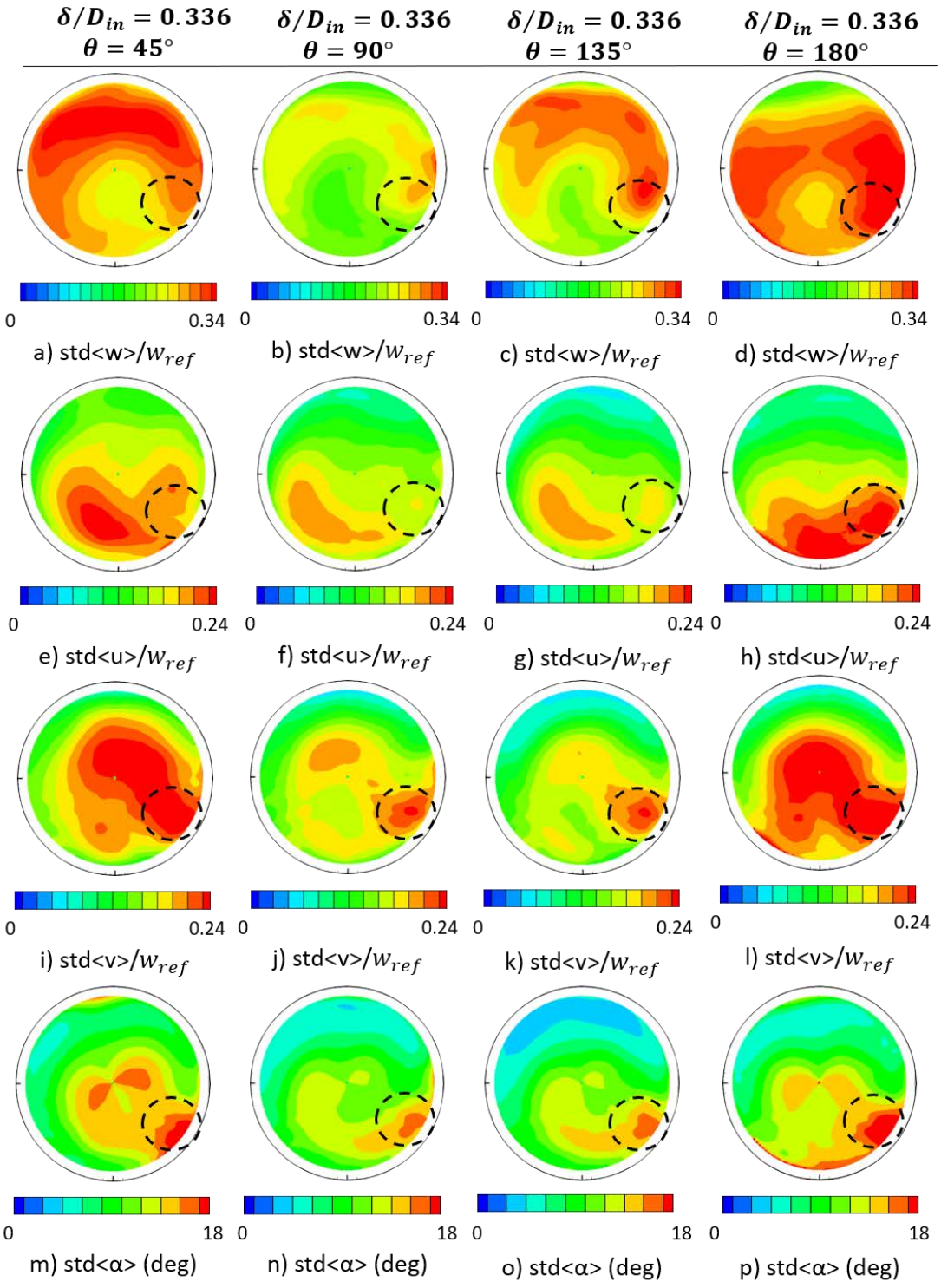

Figure 4-6: Standard deviation of the flow field at the AIP for the cases with the ingestion of a boundary layer of $\delta/D_{in} = 0.336$ thickness at $\theta = 45°, 90°, 135°$ and $180°$.

In line with the time-averaged results, the change in location of the BL ingestion affects both the peak values and the patterns of the unsteady flow field. While the unsteadiness peak values of the cases with boundary layer ingestion at $\theta = 45°$ and $180°$ increase with respect to the baseline case in all the velocity components and swirl angle fluctuations, therefore being negatively affected, the values of the cases with BLI locations at $\theta = 90°$ and $135°$ generally decrease. The region of axial unsteadiness is observed in the same area of the high time-averaged axial velocities in all the cases, while no peaks of unsteadiness are shown in connection to the region of secondary loss. The horizontal unsteady pattern is mainly located between the regions of high and low time-averaged horizontal velocity magnitudes, while the vertical one coincides with the region of loss of the time-averaged axial velocity. Despite quite high levels of standard deviation are observed in the unsteady secondary flows, especially in the cases with BL ingestion at $\theta = 45°$ and $180°$, the peak values of the unsteady swirl angles remain broadly unaffected, even though a dominant bulk swirl pattern is observed in the cases with BL ingestion at $\theta = 90°$ and $135°$, as for the time-averaged results.

4.2 Swirl distortion

One of the key aims of this work is to demonstrate that studies based on steady data are quite limited, since conventional time-averaged measurement underestimate the swirl distortion, and that the observation of unsteady distortion data has great benefits. Moreover, the influence of the ingestion of a thick boundary layer on the unsteady swirl distortion needs to be further assessed, and no other relevant work has investigated the topic yet. A good understanding of the swirl intensity and pattern at the AIP is important, especially from a compressor designer point of view, for whom not only the mean and standard deviations are important, but also the likelihood of unsteady distortion events. The swirl descriptors used to assess these aspects are the Swirl Intensity (SI), Swirl Pairs (SP), and Swirl Directivity (SD) descriptors proposed by the Society of Automotive Engineers [7]. While SI assesses the intensity of the swirl distortion, SD provides indications about the flow direction rotation. SP instead indicates the number of swirl pair that characterises the swirl pattern at the AIP. More information about the descriptors can be found in Section 2.5. The analysis of the unsteady swirl distortion is carried out in three main steps. First, area-averaged swirl descriptors' statistical properties are

presented, to provide an initial idea of the swirl distortion in each studied case. Moreover, they represent a useful means of comparison to evaluate how much steady data underestimate the swirl distortion. Second, plots that interpolate the values of the SI descriptor over the non-dimensional radius r/R_{AIP} are studied, to evaluate which of the radial positions is responsible for the most intense swirl distortion in each case studied. This second analysis brings the discussion further, providing an idea of which areas of the downstream compressor blades are mostly affected by the swirl distortion. Finally, the consideration of the relationship between the metrics evaluated for each snapshot allows to identify the most common and rare swirl distortion patterns that occur at those different radial positions, and to understand which of them is responsible for the promotion of the greatest swirl intensity values.

4.2.1 Area-averaged swirl distortion metrics

Table 4-3 presents the area-averaged and time-averaged values of the swirl descriptors. As expected, based on the swirl angle distributions and variations, the time-averaged swirl intensity SI_{mean} is higher in all the cases with boundary layer ingestion, with the maximum peak being observed for the case with BL ingestion at $\theta = 45°$, $SI_{mean} = 11.1$. The effect of the BL ingestion on the averaged swirl angle standard deviation is instead different, and lower values than the baseline case are observed in both the cases with BL ingestion at $\theta = 90°$ and $135°$. A very key aspect in the discussion is the consideration of the unsteady variation in the swirl distortion metrics since previous data were only concentrated on average levels. The data presented in Table 4-3, where maximum and minimum unsteady values are considered, show that the unsteady swirl aspects are quite substantial. It is of notice that, in spite the baseline case has the lowest time-averaged mean swirl intensity distribution, it also presents the highest unsteady fluctuations compared to the mean value, with maximum magnitudes up to 2.8 times higher. This does not mean that it is also the case with the highest SI_{max} value, that is instead observed in the case with BL ingestion at $\theta = 45°$, where $SI_{max} = 29.2$. Overall, the unsteady values of the baseline case are higher than what was observed by Gil-Prieto [33] and Zachos et al. [4]. The difference might be caused by the presence of mis-calculated vector maps in the dataset. Generally, even though the ingestion of boundary layer is responsible for increased levels of swirl intensity, it generally does not seem to

greatly affect its unsteadiness, and in some cases, it even helps to reduce the unsteady swirl variations.

As depicted in Figure 2-21 of Section 2.5.2.3, the swirl directivity parameter SD varies in the range of $SD = \pm 1$, where the extreme values indicate the presence of counter or co-rotating bulk swirls, while a value of zero represents instead symmetric twin swirls. In the same way, the SP parameter minimum value of $+0.5$ indicates a bulk swirl pattern, while a value as high as 1 is shown in presence of a pair of twin swirls. Higher values of the SP descriptor are reached if multiple swirl pairs appear. For almost all the cases but the BL ingestion at $\theta = 45°$, the mean area-averaged swirl directivity is approximately zero, indicating that the average swirl distortion pattern is quite symmetrical with respect to the vertical axis. The higher value of swirl directivity in the case with BL ingestion at $\theta = 45°$ was expected and it matches the time-averaged result shown in Figure 4-3m, where the presence of a strong bulk swirl pattern is evident, even though its standard deviation is characterized by a symmetrical twin swirl pair. The time-averaged value of SD is highly misleading, and deviations from its values (SD_{std}) are found to be 5 times higher. The maximum swirl directivity fluctuation is almost one in all the cases, indicating unsteady patterns with positive bulk swirls in the flow field. The minimum area-averaged swirl directivity fluctuation on the other hand is higher than -1 in the cases with BLI at $\theta = 45°, 90°$ and $135°$, where a pure counter-rotating bulk swirl pattern is never achieved.

The area-averaged SP values are in the range of $0.8 \div 0.9$ in all the cases, indicating that a slightly unequal counter-rotating one-per-revolution swirl pair pattern is present in all the cases.

Table 4-3: Area-averaged swirl descriptor statistical properties.

	Baseline, $\delta/D_{in} = 0.09$	$\delta/D_{in} = 0.336$ $\theta = 0°$	$\delta/D_{in} = 0.336$ $\theta = 45°$	$\delta/D_{in} = 0.336$ $\theta = 90°$	$\delta/D_{in} = 0.336$ $\theta = 135°$	$\delta/D_{in} = 0.336$ $\theta = 180°$
SI_{mean}, deg	8.4	9.7	11.1	9.3	8.7	9.1
SI_{std}, deg	2.9	3.3	3.5	2.5	2.4	3.2
SI_{min}, deg	2.2	2.4	2.7	2.6	2.5	2.3
SI_{max}, deg	23.9	27.4	29.2	21.9	20.8	25.7
SD_{mean}	0.02	0.03	0.26	0.01	0.05	-0.01
SD_{std}	0.52	0.52	0.48	0.44	0.45	0.51
SD_{min}	-0.99	-0.99	-0.98	-0.92	-0.94	-0.99
SD_{max}	0.99	0.99	1	1	0.99	0.99
SP_{mean}	0.88	0.90	0.82	0.82	0.84	0.91
SP_{std}	0.27	0.28	0.26	0.26	0.27	0.29
SP_{max}	2.78	2.73	2.64	2.76	3.05	2.87

The values found are in good agreement with what is discussed in the work of Zachos et al. [4]. The range found for the time-averaged SP parameter slightly disagrees with the time-averaged result in the baseline and in the BL ingestion at $\theta = 0°$ and $180°$, where a symmetrical twin swirl pattern was observed. The standard deviation of the SP descriptor is lower than that of SD_{std}, with values of about 25% of the mean SP, that indicates different patterns in the flow field from the one suggested by SP_{mean}. Finally, values of SP_{max} between approximately 2.6 and 3 are observed in all the cases, indicating the presence of multiple-per-revolution events, and that up to two or three pairs of contrarotating swirl regions can be developed.

At this point, the general idea from the analysis is that the ingestion of boundary layer does not greatly affect the SP parameter, that has similar values both in terms of mean and unsteady results. The SD time-averaged parameter is found to be highly misleading, and values of standard deviation five times higher are observed in all the studied cases. The swirl directivity descriptor fluctuations suggest that pure positive bulk swirl patterns can be observed in all the cases, while pure negative bulk swirls do not appear at $\theta = 90°$ and $135°$. The swirl intensity is the parameter that changes the most. As already mentioned, the ingestion of boundary layer increases the mean swirl intensity with respect to the baseline case, but the highest fluctuations with respect to the time-averaged value are observed in the baseline case itself. However, higher values of SI_{max} than the baseline case are observed when the BL is ingested at $\theta = 0°, 45°$ and $180°$, while lower maximum values of swirl intensity fluctuations are observed in case of BL ingestion at $\theta = 90°$ and $135°$. These two cases also show reduced standard deviation values in all the three swirl descriptor parameters, showing that the ingestion of a thick boundary layer at those inlet locations improves the swirl distortion standard deviation. This result matches with what was observed in Section 0. Boundary layer ingestion at $\theta = 45°$ has instead a negative impact on the value of SI_{std}, which is 1.2 times higher than the baseline case. In general, high values of standard deviation are shown for all the cases, which once again highlights the unsteady nature of the flow field at the AIP of curved ducts.

4.2.2 Radial distribution of swirl distortion

The area-averaged swirl distortion metrics provide a good starting point to understand that steady data underestimate the swirl distortion, and in the case of the time-averaged SD parameter the results are highly misleading. However, still no information about its radial distribution have been gathered. To investigate the radial positions at which the swirl distortion is more intense, the data have been interpolated in a polar grid. Conventional methods use 40 pressure probes distributed in 8 equi-spaced azimuthal positions at 5 radii at centres of equal area rings [15]. In industry, the common values for the 5 radii are $r/R_{AIP} = 0.32, 0.55, 0.71, 0.84, 0.95$ (Figure 4-7). In experimental investigations made with the S-PIV technique, the last radial position usually corresponds to spurious data near the S-duct wall, and it should not be considered. Since a higher number of radial positions is suggested to have a broad and clear idea of the problem, for this work the number of radial positions chosen for the evaluation of the distortion metrics has been increased to nine, at $r/R_{AIP} = 0.1, 0.2, 0.3, 0.4, 0.5, 0.6, 0.7, 0.8$ and 0.9.

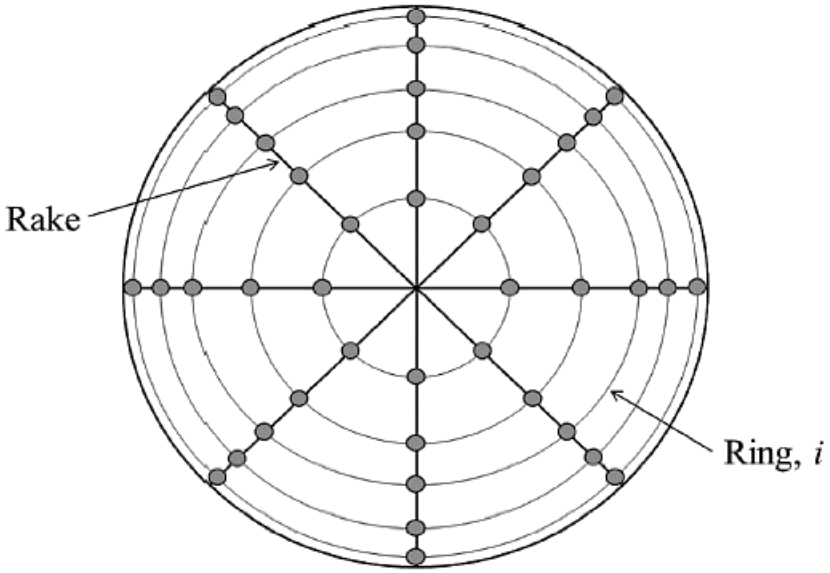

Figure 4-7: Example of 8x5 ring and rake AIP discretization for the inlet flow distortion measurements [15]**.**

The use of the S-PIV technique with the cameras in portrait mode allows to investigate the radial distribution with a good spatial resolution, of about $\Delta r/R_{AIP} = 0.034$. The polar grid used to investigate the swirl radial distribution therefore consisted of 72 equi-

spaced azimuthal positions (rakes) and 9 equi-spaced radii between $r/R_{AIP} = 0.1$ and 0.9.

The radial distribution of swirl distortion is quantified with the swirl intensity (SI) distortion descriptor. For detailed information about the parameter see Section 2.5 In Figure 4-8, Figure 4-9, Figure 4-10 and Figure 4-11 the time-averaged, standard deviation, and minimum and maximum values of the unsteady SI_i are plotted, with *i* being the non-dimensional radial position along the polar grid. In the baseline case, the mean swirl intensity (SI_{mean}) shows a monotonic reduction as the radius increases, from 10° at $r/R_{AIP} = 0.1$ to 7° at $r/R_{AIP} = 0.9$. The same decreasing trend is shown by all the other cases until the radial position $r/R_{AIP} = 0.6$ ($r/R_{AIP} = 0.7$ for the case with BL ingestion at $\theta = 0°$) is reached. An increasing trend until the last radial position follows.

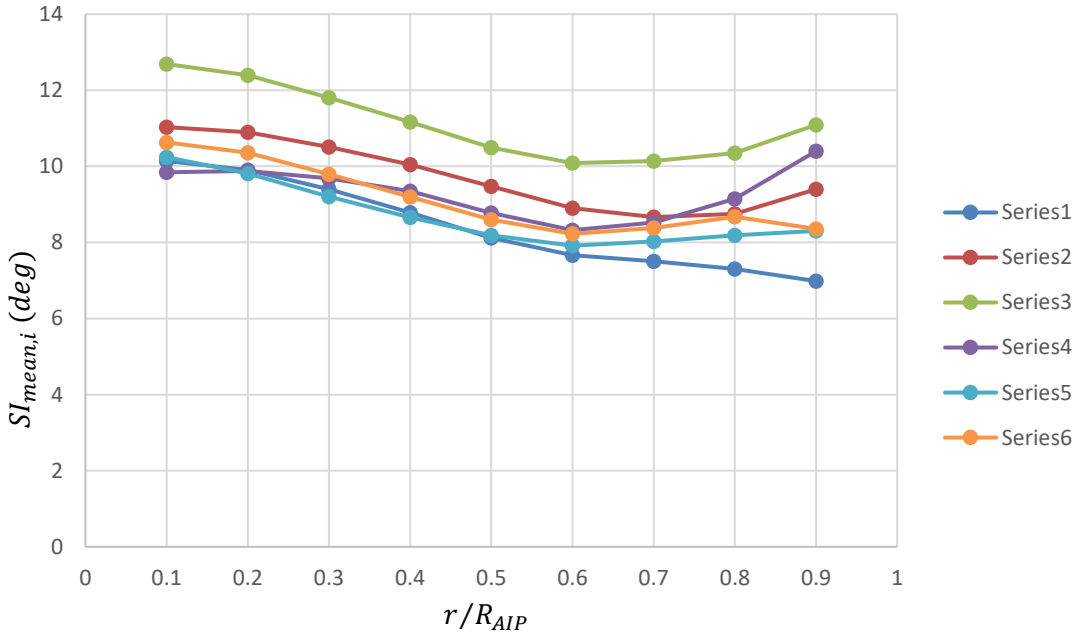

Figure 4-8: Time-average swirl intensity at different radial positions.

The major levels of SI_{mean} are observed at the inner-most radial position for all the cases, with the only exception of the case with boundary layer ingestion at $\theta = 90°$, where SI_{mean} at $r/R_{AIP} = 0.9$ is about 10.5° and about $SI_{mean} = 10°$ at $r/R_{AIP} = 0.1$.

For this case, the major levels of SI_{mean} are observed at the outer-most radial position. It is worth underlying the trend shown by the case with BL ingestion at $\theta = 180°$, with a decreasing curve of about 1.6% between $r/R_{AIP} = 0.8$ and 0.9, to a value of $SI_{mean} = 8.5°$. The anomaly between the last two radial positions appears not only in the mean swirl intensity plot, but also in the following ones. The standard deviation of the swirl intensity also shows a monotonic decreasing trend, with peak values located at the inner-most ring.

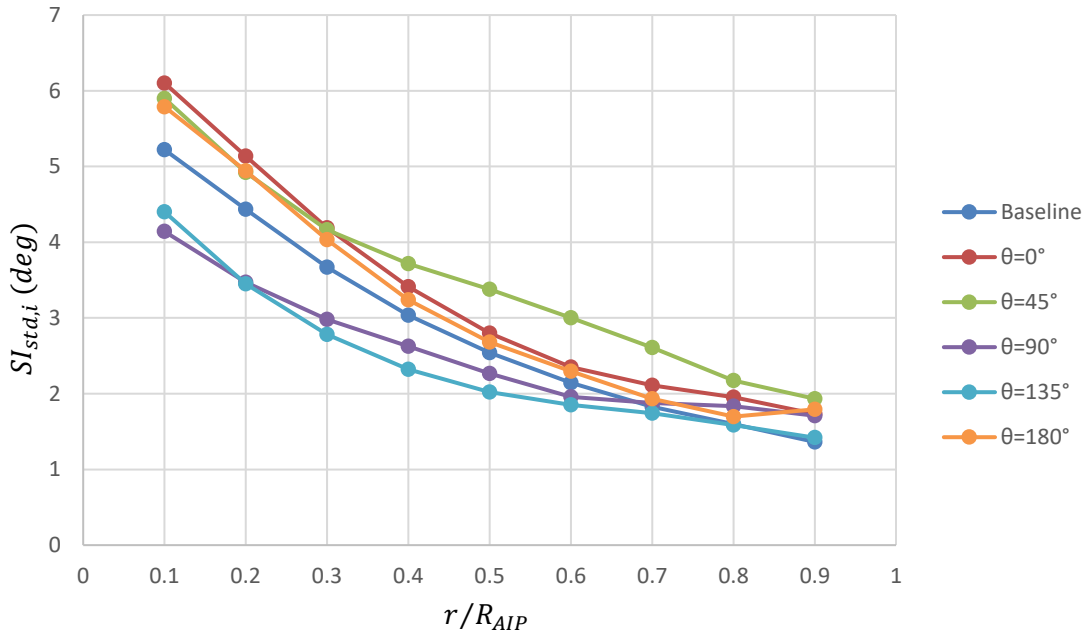

Figure 4-9: Swirl intensity standard deviation at different radial positions.

The peak values confirm the area-averaged results: the boundary layer ingestion increases the levels of swirl intensity standard deviation, with the exception of the cases at $\theta = 90°$ and 135°. Despite the case with the highest peak at the inner-most location is shown for the case with BLI at at $\theta = 0°$ and not for the case with BLI at $\theta = 45°$ (Figure 4-9), that according to Table 4-3 is supposed to be the case with the highest area-averaged swirl intensity standard deviation, the trends of the two cases suggest that, overall, the latter case have higher values as the radius increases. The value of $std(SI)$ reduces in all the cases of approximately $25 - 30\%$ between the inner and the outer radial position. Again, the case with BL ingestion at $\theta = 180°$ shows a trend exception between the two final radial positions, with a slight increasing curve. As already highlighted in the area-

averaged results, the levels of standard deviation clearly indicate that the nature of the swirl distortion is highly unsteady. In addition, the radial distribution analysis suggests that the fluctuation levels shown in Figure 4-9 are approximately 50% and 20% of the respective time-averaged values at the inner-most and outer-most radial positions. The lower percentage perfectly matches with the study of Gil-Prieto [33], while the values of the standard deviation at the inner-most radial position are 10% higher. The 10% increase in fluctuations might be connected to the presence of mis-calculated vector maps in the dataset, whose percentage quite matches with the result. In addition, the analysis points out that the area-averaged results underestimated the levels of swirl intensity standard deviation at the AIP centre and overestimated them at the duct wall. As expected, the lowest values of minimum instantaneous swirl intensity are observed at the most-inner radial position $r/R_{AIP} = 0.1$ (Figure 4-10), in a range of about $SI_{min} = 0.5 \div 1$ for all the cases. The general trend increases in a fragmented way until the last radial position. Table 4-3 showed that the case with the minimum value of SI_{min} was the baseline case, result confirmed also in Figure 4-10, where the case also presents the lowest values of minimum instantaneous swirl intensity at all radial positions, with two even lower peaks at $r/R_{AIP} = 0.4$ and 0.8. On the contrary, the case with BL ingestion at $\theta = 45°$ showed the highest time-averaged area-averaged result (Table 4-3), and again the result corresponds to the trend shown in Figure 4-10, with the highest values up to approximately $SI_{min} = 4.7°$ at the outer-most radius. However, the most interesting trend is provided by the case with BL ingestion at $\theta = 135°$, where an important decreasing trend with values as low as 2.4° is shown between $r/R_{AIP} = 0.5$ $r/R_{AIP} = 0.7$. Figure 4-3o indicates that this radial location might correspond to the area of low swirl angles depicted in the upper part of the AIP. Despite this, the loss is immediately recovered while approaching the S-duct wall. Again, the case with BL ingestion at $\theta = 180°$ shows an exceptional trend between the last two radial positions.

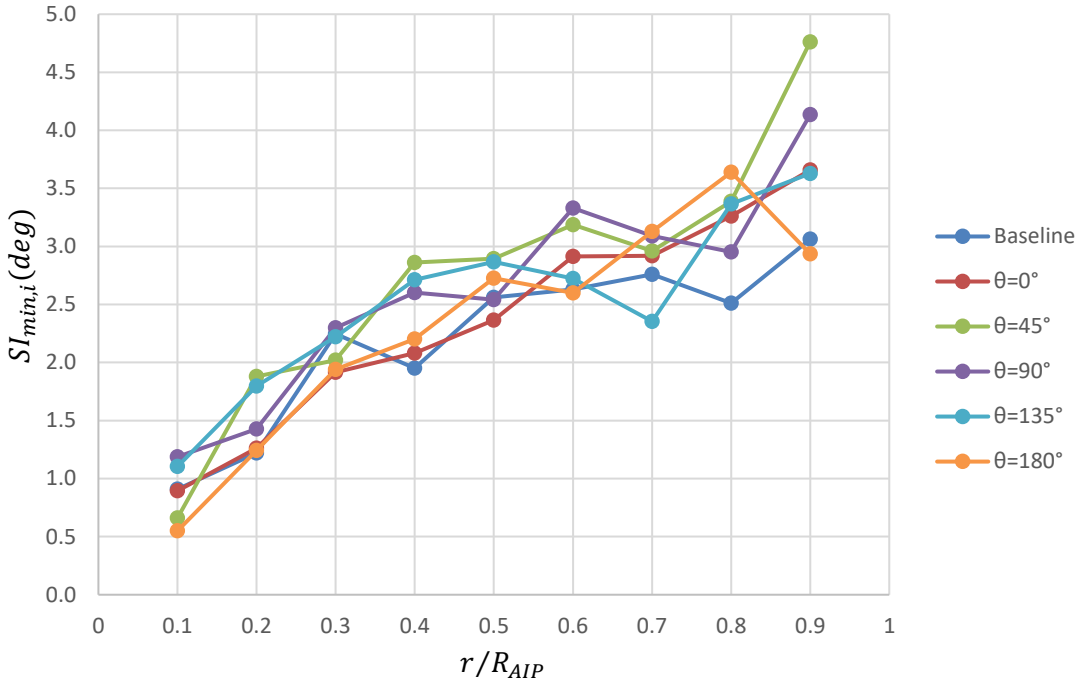

Figure 4-10: Minimum instantaneous swirl intensity at different radial positions.

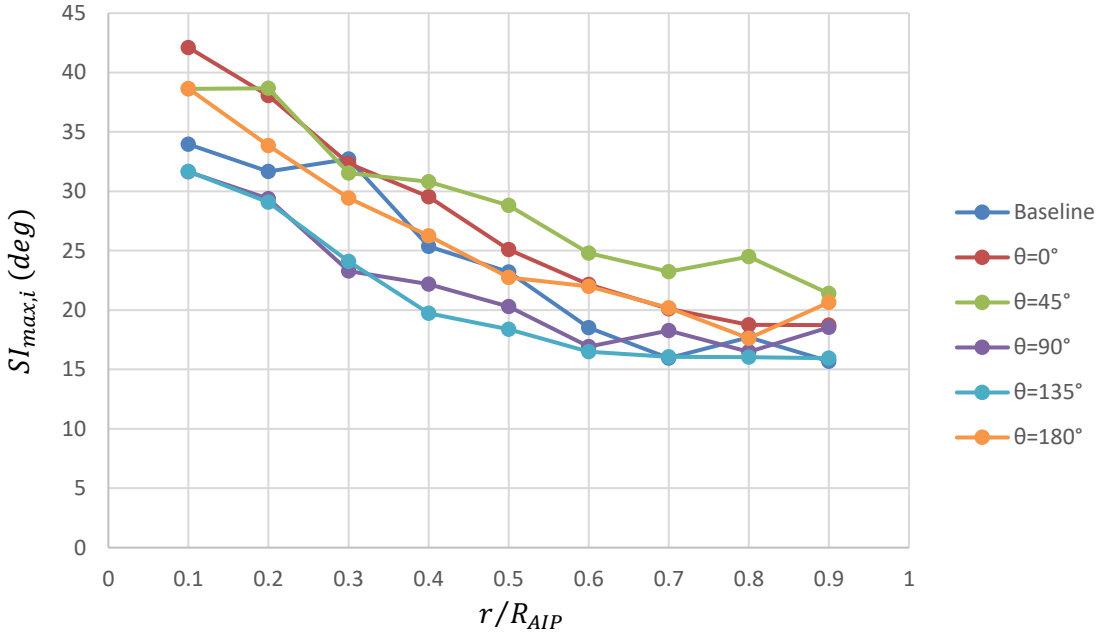

Figure 4-11: Maximum instantaneous swirl intensity at different radial positions.

Finally, the maximum instantaneous swirl intensity radial distribution is investigated. SI_{max} shows a trend similar to SI_{std}, with the greatest values found at the most-inner

radial position. At that radial position, the peak of $SI_{max} = 44°$ is shown in the case with BL ingestion at $\theta = 0°$. The prediction of low levels of instantaneous fluctuation of Table 4-3 in the cases with the distortion screen positioned at $\theta = 90°$ and $135°$ is correct, and they show the lowest values of SI_{max} at almost all the radial positions. The minimum values of instantaneous fluctuations are found at $r/R_{AIP} = 0.8$ for the ingestion of boundary layer at $\theta = 90°$ and $180°$, and at $r/R_{AIP} = 0.9$ in all the other cases, with values that drop of about half with respect to those of the inner-most radial position. The final range showed by all the cases is about $SI_{max} = 15.6° \div 20.3°$, with the two extreme values being of the baseline and the case with BL ingestion at $\theta = 45°$ respectively. The peaks observed in the maximum instantaneous swirl intensity descriptor are a good indication of the unsteady distortion that affects the fluid flow, with maximum values for all the cases that are about 3 or 3.5 times greater than the respective time-averaged levels of SI_{mean} at the inner-most radial position. The distorted performance at the radial position of $r/R_{AIP} = 0.9$ of the case with BL ingestion at $= 180°$, that has been noticed in all the charts of the SI distortion metrics parameters, is probably due to a combination of factors, like an increased influence of the area of low seeding, the presence of the highest percentage of mis-calculated vector maps in the case, and possible increased accumulation of the seeding oil on the duct wall, as well as light reflections.

Table 4-3 highlighted the fact that the ingestion of boundary layer (BL) has a negative impact on the mean values of the swirl distortion intensity at all the different ingesting locations, results confirmed in the current section for also almost all the radial positions. The area-averaged results are also in good agreement with the plot of Figure 4-9, where it is shown that the ingestion of boundary layer has a negative impact on the swirl intensity standard deviation when ingested at $\theta = 0°, 45°$ and $180°$ in all the radial positions, while its impact is positive if ingested at $\theta = 90°$ and $135°$. Finally, the maximum fluctuations are also observed at the inner-most radial position, with lowest values of SI_{min} and highest values of SI_{max}. Among all, the case with BL ingestion at $= 135°$ shows the best performance in the swirl distortion analysis, baseline case included, since it has time-averaged levels of SI_{mean} similar to the baseline case, but lower fluctuations.

Overall, the analysis performed has shown how steady data are not only incapable of providing information about the unsteady swirl distortion, but they also highly

underestimate the levels of swirl intensity. Conventional measurement methods that asses the swirl distortion intensity with pneumatic probes can provide only steady information, underpredicting the results. Moreover, they cannot provide information about the regions of greatest swirl intensity, being a great limitation since peak events can drive engine instabilities. The investigation performed at different radial positions clears also that the area-averaged distortion metrics provide a good indication of the general trend of the swirl distortion parameters, but obviously underestimate or overestimate the instantaneous values at different radial positions. The need for unsteady swirl data to capture the nature of the swirl distortion in complex S-duct has therefore been demonstrated. For this work, the highest levels of SI_{mean}, SI_{std} and SI_{max} are observed at the most-inner radial position, that means that the most distorted flow invests the area at the hub of the compressor blades in the downstream machine. The results found agree with previous works [4], [33].

4.2.3 Unsteady characteristics of swirl distortion

In the previous section, the magnitude of the swirl distortion intensity descriptor was quantified at different radial positions. The aim of this section is to identify the most common and rare swirl distortion patterns that occur at those different radial positions, and to understand which of them is responsible for the promotion of the greatest swirl intensity values. Understanding the two aspects is important since the response of the fan depends on both the intensity of the swirl distortion at different radial positions. Although the analysis performed so far provides a good quantitative description of the distortion metrics, additional interesting information can be extracted from the consideration of the relationship between the metrics evaluated for each snapshot. The swirl descriptors chosen for this work are the same of those used to analyse the area-averaged results, and are the Swirl Pair (SP), the Swirl Intensity (SI) and the Swirl Directivity (SD). Further information on the parameters are found in Section 2.5. At a certain radial position, SI is a measure of the swirl intensity, SP indicates the number of swirling region pairs that appears in the circumferential distribution of the swirl angle, while SD evidences in which sense the swirling flow is rotating. For example, while the swirl intensity can assume whatever value in each case, SD varies between ± 1, with -1 indicating a counter-rotating swirl, 0 a symmetric pair of swirl, and 1 a co-rotating swirl (Figure 2-21). Similarly, $SP =$

0.5 indicates the presence of a counter or co rotating swirl, $SP = 1$ is typical of a one-per-revolution swirl pair, while higher values of the SP descriptor indicate multiple-per-revolution swirling regions (Figure 2-22). For the analysis, the descriptors have been calculated with the aid of the same polar grid described in Section 0, and so at the same radial positions. Finally, it is important to highlight that such an analysis on the unsteady swirl distortion is possible only thanks to the use of the Stereo Particle Image Velocimetry Technique, that combines a good level of spatial resolution together with a synchronous acquisition. To characterise the pattern of the swirl distortion, the probability maps with the joint-Probability Density Function (PDF) of the SD and SP descriptors are first computed. The probability maps of SI and SP descriptors are later investigated, to understand which of the previously identified swirl patters promotes the highest levels of intensity. To evaluate the joint-PDF, each descriptor range was first discretized into 60 equispaced partitions, resulting in a resolution of approximately 0.5°, 0.03° and 0.03° for the SI, SP and SD descriptors respectively. An integration of the PDF over the area followed, to obtain the probability to find the distorted pattern in the desired region. For example, for the SP-SD descriptors, the equation would be:

$$\boldsymbol{P(SD_A \leq SD < SD_B, SP_A \leq SP < SP_B) = \int_{SP_A}^{SP_B} \int_{SD_A}^{SD_B} PDF\, dSD\, dSP} \qquad \textbf{(4-2)}$$

As already mentioned, probability maps for SP-SD are useful to assess the relative likelihood of the different unsteady swirl patterns in the flow field. Figure 4-13, Figure 4-14 and Figure 4-15 show these probability maps only at $r/R_{AIP} = 0.1$ 0.5 and 0.8, for the sake of brevity. A complete overview of the probability maps about all the missing radial positions can be found in Appendix A.2. The inner-most radial position has been chosen since it is where the most important swirl distortion is observed, while $r/R_{AIP} = 0.8$ is a good representative of the swirl distortion region near the duct wall, where the maximum instantaneous swirl intensities are located. The outer-most radius has been avoided to get rid of possible residual spurious data connected to the wall reflections or seeding accumulation. A medium radial position was finally considered a useful means of comparison. Most of the results show that the flow tends to oscillate between different areas with high probabilities associated with twin swirl ($SP = 1.0, SD = 0.0$), negative or positive bulk swirl ($SP = 0.5, SD = -1.0/1.0$) or non-symmetric paired swirl patterns. Equation (4-2) allows to quantify the probability of having twin and bulk swirl

events with an integration of the PDF over small areas around the ideal values that are associated with these states. The area considered for twin swirl patterns is defined by $SP \in [0.9, 1.1]$ and $SD \in [-0.1, 0.1]$ (4-3), while for the probability to have bulk swirl patterns is calculated for $SP \in [0.5, 0.7]$ and $|SD| \in [0.8, 1.0]$ (4-4), with the latter including both positive and negative events.

$$\boldsymbol{P_{twin} = \int_{0.9}^{1.1} \int_{-0.1}^{0.1} PDF\ dSD\ dSP} \quad \textbf{(4-3)}$$

$$\boldsymbol{P_{bulk} = \int_{0.5}^{0.7} \int_{-1.0}^{-0.8} PDF\ dSD\ dSP + \int_{0.5}^{0.7} \int_{0.8}^{1.0} PDF\ dSD\ dSP} \quad \textbf{(4-4)}$$

Table 4-4 shows the calculated probabilities for all the cases at $r/R_{AIP} = 0.1, 0.5$ and 0.8, while a more complete table with the probabilities calculated at all the radial positions is reported in Appendix A.2. Another consideration that must be made is that Figure 4-13, Figure 4-14 and Figure 4-15 show values of the SP parameter as high as $SP = 2/2.5$. This indicates that the flow not only oscillates between different swirl states, but also exhibits a variety of swirl patterns with multiple swirling regions, and not only the classical swirl pair that appears in the time-averaged results of Section 4.1.1. To ease the analysis, a path of high probability is considered, that follows the formula $SP = 1/(1 + |SD|)$ and is plotted in Figure 4-12. This high probability path represents the lowest value that the swirl descriptor SP can adopt for any given value of SD, and it is valid for only one-per-revolution swirl patterns with two main swirling regions. Along the path, one of the two swirling regions dominates over the other, with the flow switching between positive and negative bulk swirl patterns. Any position above this high probability path is characterised by values of SP greater than 1, and therefore indicates the presence of multiple swirling regions.

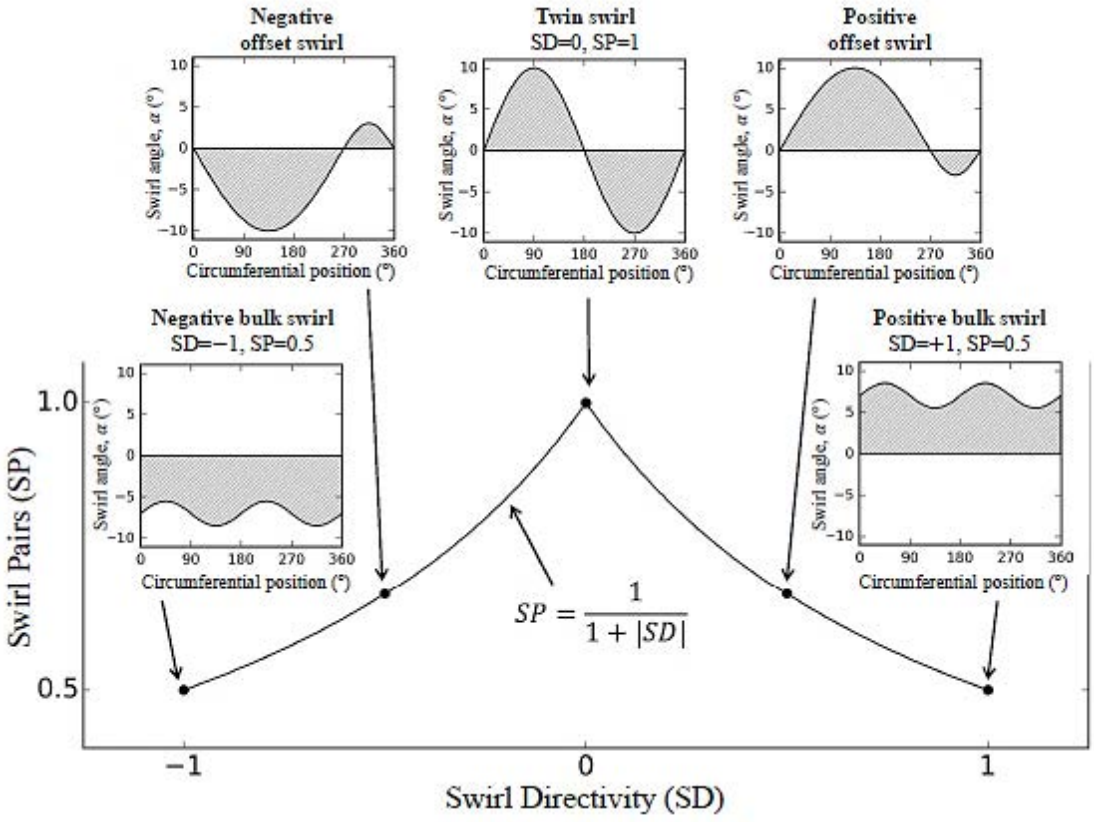

Figure 4-12: One-per-revolution bulk to swirl high probability path [33]**.**

The probability map of the baseline case at the inner-most radial position shows a quite good agreement with the time-averaged results of Figure 4-2, with a 24.8% probability to have the same symmetrical twin swirl pair pattern ($SP = 1, SD = 0$). Despite this, less frequent events with SP values as high as 2 are also observed, that indicate possible additional swirling regions. Moreover, 9.8% probability to have a bulk swirl pattern, mainly counter-rotating, is also shown ($SP = 0.5, SD = -1.0$).

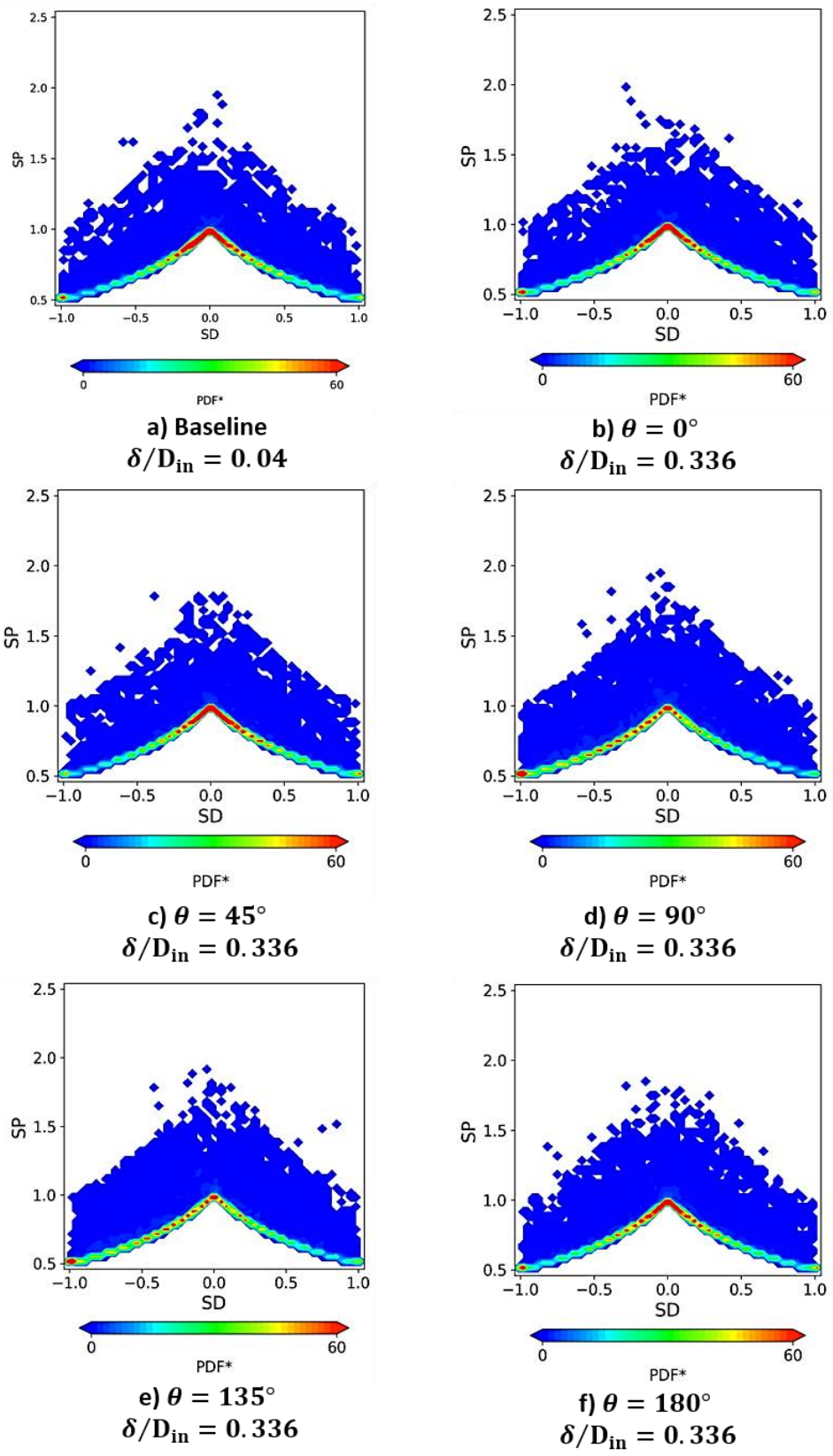

Figure 4-13: SP_SD probability maps at $r/R_{AIP} = 0.1$ for the baseline and the cases with BL ingestion at $\theta = 0°, 45°, 90°, 135°$ and $180°$.

The amount of twin swirl patterns reduces significantly to $P_{twin} = 4.3\%$ at an intermediate radial position ($r/R_{AIP} = 0.5$), where both positive ($SP = 0.5, SD = 1$) and negative ($SP = 0.5, SD = -1.0$) bulk swirl events are found (20.9%), whereby with a flow rotation in a single direction. Finally, a good probability to find twin swirl events is re-established near the wall ($P_{twin} = 10.8\%$), while the probability for the flow to rotate in one single direction falls to 5.4%. A similar swirl distortion pattern to the one just described for the baseline case is observed in the cases with BLI at $\theta = 0°$ and 180°, and this matches with all the results found so far. For the BL ingestion at $\theta = 45°$, the probability maps indicate significant deviations from the time-averaged results at the inner-most radial position. Figure 4-2 shows that the flow has one predominant non-symmetrical vortex, but in Figure 4-13 a twin swirl pattern dominates (22.6%) and the probability to have bulk swirls is only 9.8%. The result is instead in line with the standard deviation values in Figure 4-6. At $r/R_{AIP} = 0.5$ and 0.8 instead (Figure 4-14 and Figure 4-15) P_{twin} drops to 4.2% and 4.9% respectively, while the number of bulk swirl events recovers, with percentages as high as $P_{bulk} = 23.7\%$ and 21%. The value of the SD parameter indicates that the flow mainly rotates in a co-rotating direction ($SD = 1$). In the cases with BL ingestion at $\theta = 90°$ and 135° quite different patterns are observed at the different radial positions. In Figure 4-13d and Figure 4-13e the unsteady P_{bulk} and P_{swirl} are quite balanced (~15%). In contrast, at $r/R_{AIP} = 0.5$ negative bulk swirl events predominate ($SP = 0.5, SD = -1.0$), with probabilities up to three times higher than twin swirl configurations. Near the wall, the situation inverts. Figure 4-15d and Figure 4-15e finally show more frequent excursions towards co-rotating bulk swirls (15.7% and 7.5% for the BLI cases at $\theta = 90°$ and 135°) ($SP = 0.5, SD = 0.5$), while twin swirl events are less frequent, with P_{twin} of about 3.6% and 5% respectively. Multiple swirling regions with values of SP as high as 2.5 are shown at any deviation from the high probability path for all the cases at all the radial positions.

Overall, Figure 4-13 shows flow patterns driven by twin swirl configurations in all the studied cases, even though the same percentage is found for bulk swirl events in the cases with BL ingestion at $\theta = 90°$ and 135°.

Table 4-4: Probability associated with twin ($P_{twin}(\%)$) and bulk ($P_{bulk}(\%)$) swirl events in all the analysed cases at different radial positions.

r/R_{AIP}	Probability	$\delta/D_{in} = 0.09$ Baseline	$\delta/D_{in} = 0.336$ $\theta = 0°$	$\delta/D_{in} = 0.336$ $\theta = 45°$	$\delta/D_{in} = 0.336$ $\theta = 90°$	$\delta/D_{in} = 0.336$ $\theta = 135°$	$\delta/D_{in} = 0.336$ $\theta = 180°$
0.1	$P_{twin}(\%)$	24.8	23.6	22.6	15.1	14.7	20
	$P_{bulk}(\%)$	9.8	11.8	9.8	14.8	15.1	11.5
0.2	$P_{twin}(\%)$	16.9	15.9	14.5	7.8	7.8	13.4
	$P_{bulk}(\%)$	14.7	16.7	15.1	21.5	20.2	14.1
0.3	$P_{twin}(\%)$	10.9	10.6	8.7	4.5	4.5	9.4
	$P_{bulk}(\%)$	18.2	19.2	19.6	24.5	21.5	15.9
0.4	$P_{twin}(\%)$	6	6.3	5.2	4.1	3.4	6.6
	$P_{bulk}(\%)$	20.5	18.9	22.9	23.7	18	17.1
0.5	$P_{twin}(\%)$	4.3	3.6	4.2	4.9	4.7	5
	$P_{bulk}(\%)$	20.9	17	23.7	16.6	11.8	17.2
0.6	$P_{twin}(\%)$	4.6	3.2	5.6	7.4	7.3	5.5
	$P_{bulk}(\%)$	16.5	13.5	22.1	7.9	5.7	13.4
0.7	$P_{twin}(\%)$	8.2	5.8	7	8.6	9.3	9.1
	$P_{bulk}(\%)$	9.5	9.1	20.4	5.2	3.8	7.6
0.8	$P_{twin}(\%)$	10.8	10.2	4.9	3.6	5	11.5
	$P_{bulk}(\%)$	5.4	6.3	21	15.7	7.5	3.8
0.9	$P_{twin}(\%)$	4	6.4	2.	0.3	0.6	3.2
	$P_{bulk}(\%)$	3.5	3.1	17.9	43.6	41.1	3

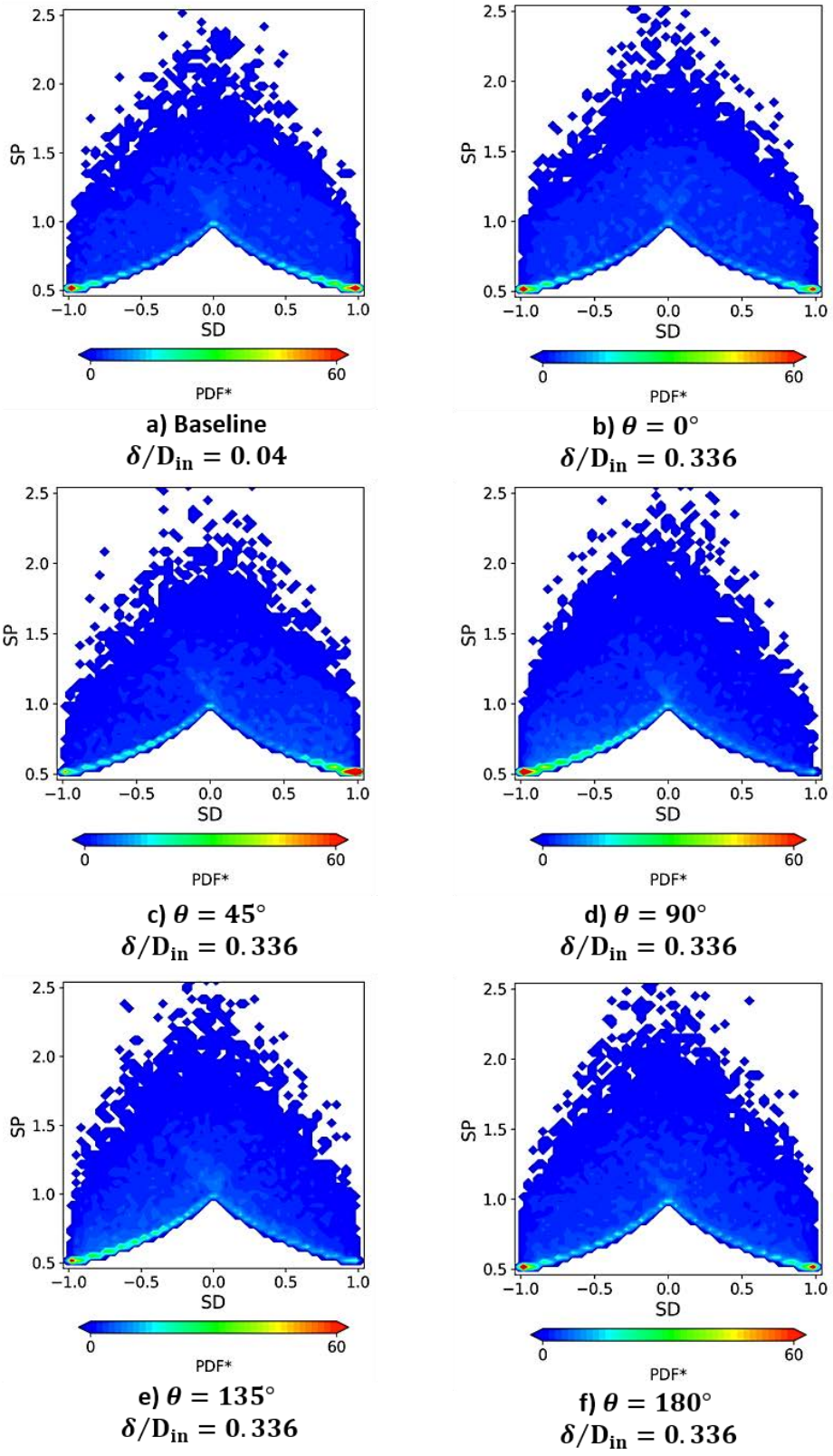

Figure 4-14: SP_SD probability maps at $r/R_{AIP} = 0.5$ for the baseline and the cases with BL ingestion at θ=0°,45°,90°,135° and 180°.

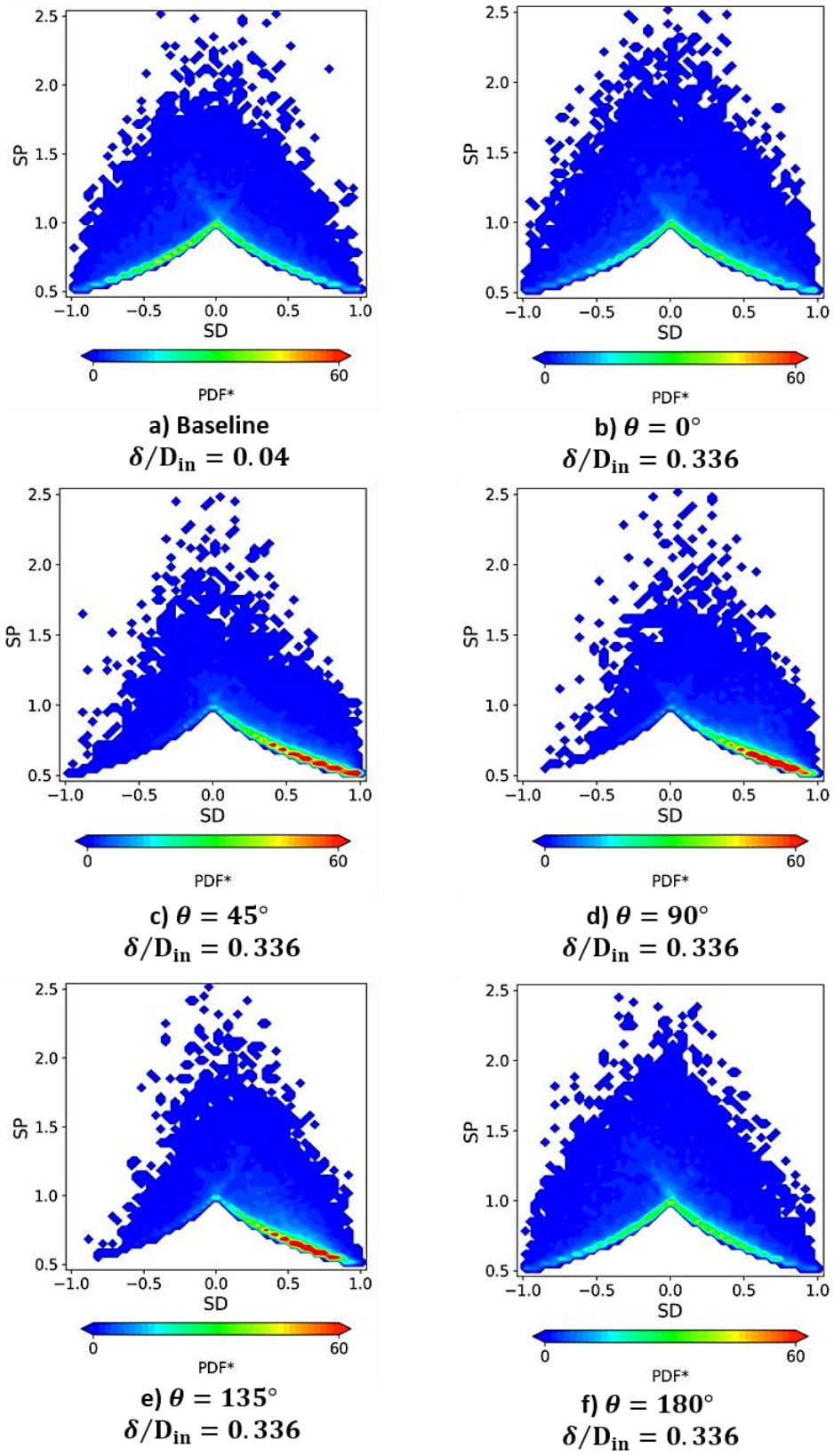

Figure 4-15: SP_SD probability maps at $r/R_{AIP} = 0.8$ for the baseline and the cases with BL ingestion at θ=0°, 45°, 90°, 135° and 180°.

At $r/R_{AIP} = 0.5$ the tendency is exactly the opposite (Figure 4-14), with higher percentages of P_{bulk}. $r/R_{AIP} = 0.8$ is instead characterised by twin swirl pairs in the baseline and in the cases with boundary layer ingestion along the vertical axis, while bulk swirl events predominate in the other cases. Lower values of both P_{bulk} and P_{twin} compared to the other radial positions are observed, which indicate a more uniform joint-PDF distribution near the duct wall. The tendency is confirmed in **Error! Reference s ource not found.** (Appendix A.2), where also the percentages related to the last radial positions are showed. However, an exception is noticed in the cases with BL ingestion at $\theta = 90°$ and $135°$ in the outer-most radial position, with P_{bulk} values that suddenly increase to 43.6% and 41.1% respectively (**Error! Reference source not found.**, Appendix A.2). The probability maps indicate a wide variety of unsteady swirl patterns, that quite deviate from the twin swirl pattern predicted in the time-averaged results. In this context, it is highlighted again that the values of the mean SD descriptor of Table 4-3 are quite misleading. The probability maps show that one-per-revolution bulk or twin swirls are more likely, and this agrees with SP_{mean} Table 4-3, even though less frequent events with two or three swirling regions are observed in all the cases at all radial positions, especially at $r/R_{AIP} = 0.5$. The comparison is useful to confirm again the limitation that time-averaged results have in providing a complete and accurate picture of the unsteady flows at the AIP of a complex intake, both in terms of swirl patterns and in their radial locations. Generally, the presence of the boundary layer ingestion affects the swirl intensity, but not the swirl pattern if the ingestion is located along the vertical axis of symmetry. On the contrary, both the intensity and the swirl pattern are affected in case of BLI at $\theta = 90°$ and $135°$, while in case of ingestion at $\theta = 45°$ the highest levels of swirl intensity are observed, with different swirl patterns that develops as the non-dimensional radius increases.

The most common and rare swirl patterns in all the cases and at different radial positions have been investigated with the aid of the SP-SD probability maps. The following aim is to investigate which of them promotes the most intense swirl distortion events.

To achieve this, the probability maps of the SI-SP descriptors are investigated at the same radial positions of the previous analysis. The missing probability maps can be found in Appendix A.2.

The inner-most radial position (Figure 4-16) shows high values of SI concentrated between $SP = 0.5$ and $SP = 1.0$, associated with one-per-revolution swirl patterns, while for $SP > 1.0$ the levels of swirl intensity highly reduce. Therefore, at the most inner radial position all the cases show high intensities connected to both twin and bulk swirl events. However, slightly higher intensities are associated with twin swirl patterns in the cases with BLI at the $\theta = 90°$ and $135°$.The situation changes at the medium radial position (Figure 4-17), where the general trend is that bulk swirl patterns ($SP = 0.5$) tend to promote the most intense swirl distortions. are more likely to generate the most intense distortion events. However, some high values of SI are also associated with twin swirl patterns ($SP = 1.0$), especially in cases with BL ingestion at $\theta = 0°$ and $90°$, but they are more isolated cases (Figure 4-17b, Figure 4-17d). The SI gradually reduces for greater SP, and the levels of swirl intensity are about one-half of the maximum values associated with bulk swirl events for $SP > 1.5$. As the radial position increases, the SI distribution flattens across the range of SP values (Figure 4-18). Near the wall, high values of swirl intensity are associated with both bulk and twin one-per-revolution swirl pair events ($SP = 0.5 \div 1.0$) in the case with boundary layer ingestion at $\theta = 90°$, while in the baseline case and in the cases with BLI at $\theta = 0°, 45°$ and $180°$ bulk swirl events tend to promote the most intense swirl distortions. The only case in which twin swirl events have higher intensities near the wall is when the BL is ingested at $\theta = 135°$. For values of $SP > 1.5$ lower SI levels are observed. Among all the cases with BL ingestion, the case with BL ingestion at $\theta = 135°$ produces the lowest levels of SI at all the radial positions.

It is worth mentioning that the pattern shown in Figure 4-16, with such different values of swirl intensity before and after $SP = 1.0$, does not match with the expected results and it is probably due to a bug of the code used to extract the images. The data below the value $SP = 1.0$ are therefore not considered reliable, and further investigation is suggested.

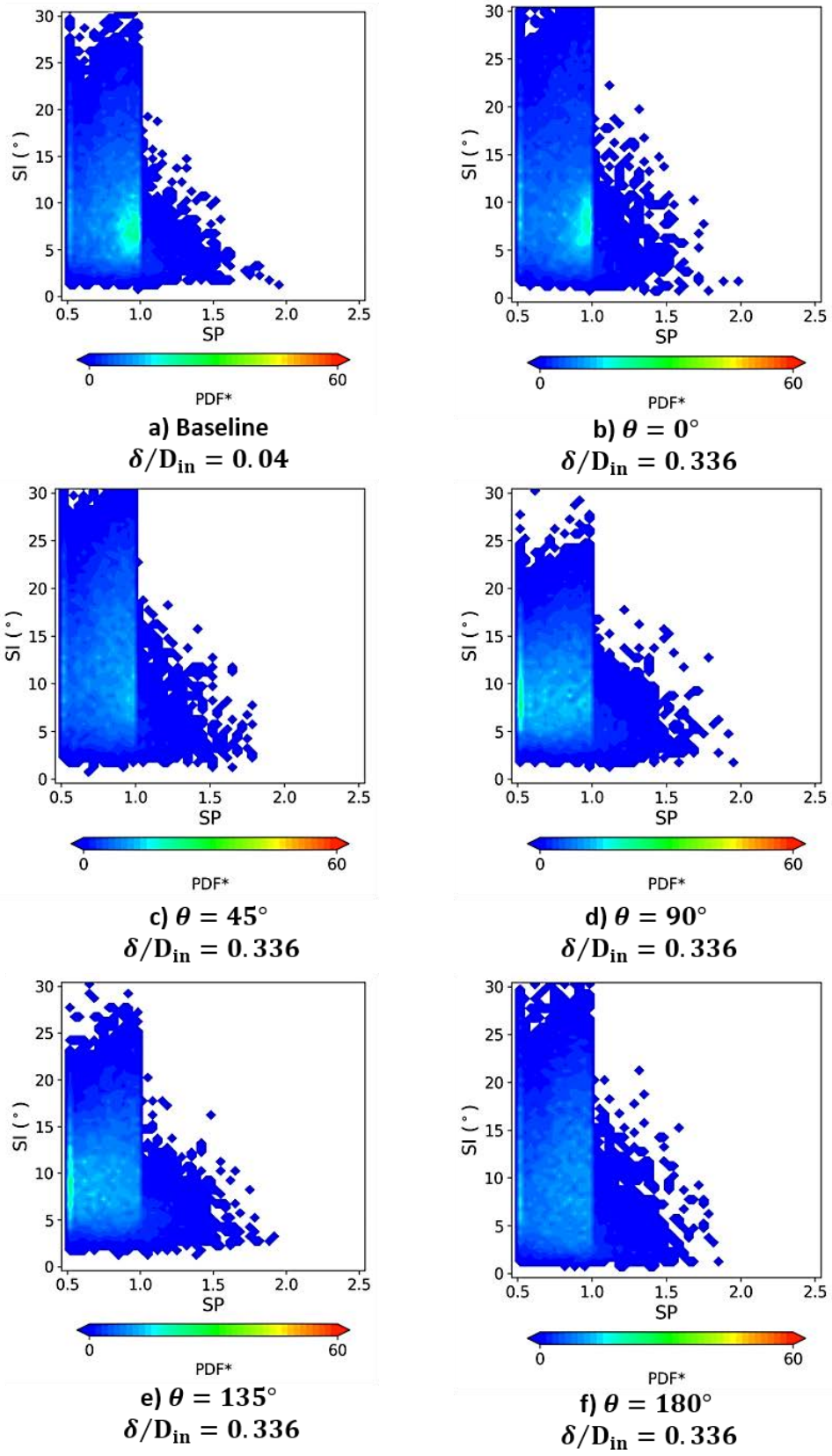

Figure 4-16: SI_SP probability maps at $r/R_{AIP} = 0.1$ for the baseline and the cases with BL ingestion at θ=0°,45°,90°,135° and 180°.

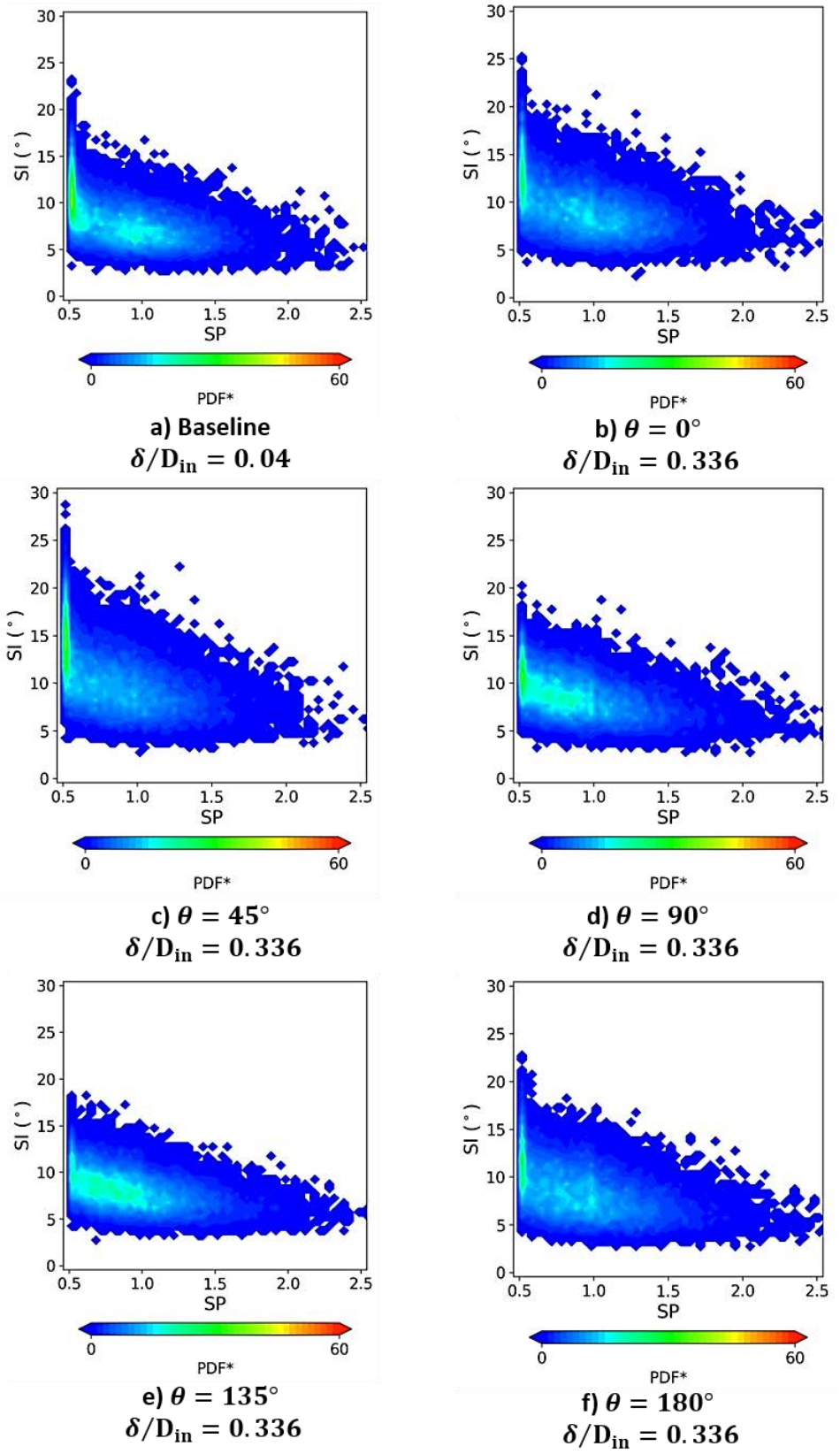

Figure 4-17: SI_SP probability maps at $r/R_{AIP} = 0.5$ for the baseline and the cases with BL ingestion at θ=0°,45°,90°,135° and 180°.

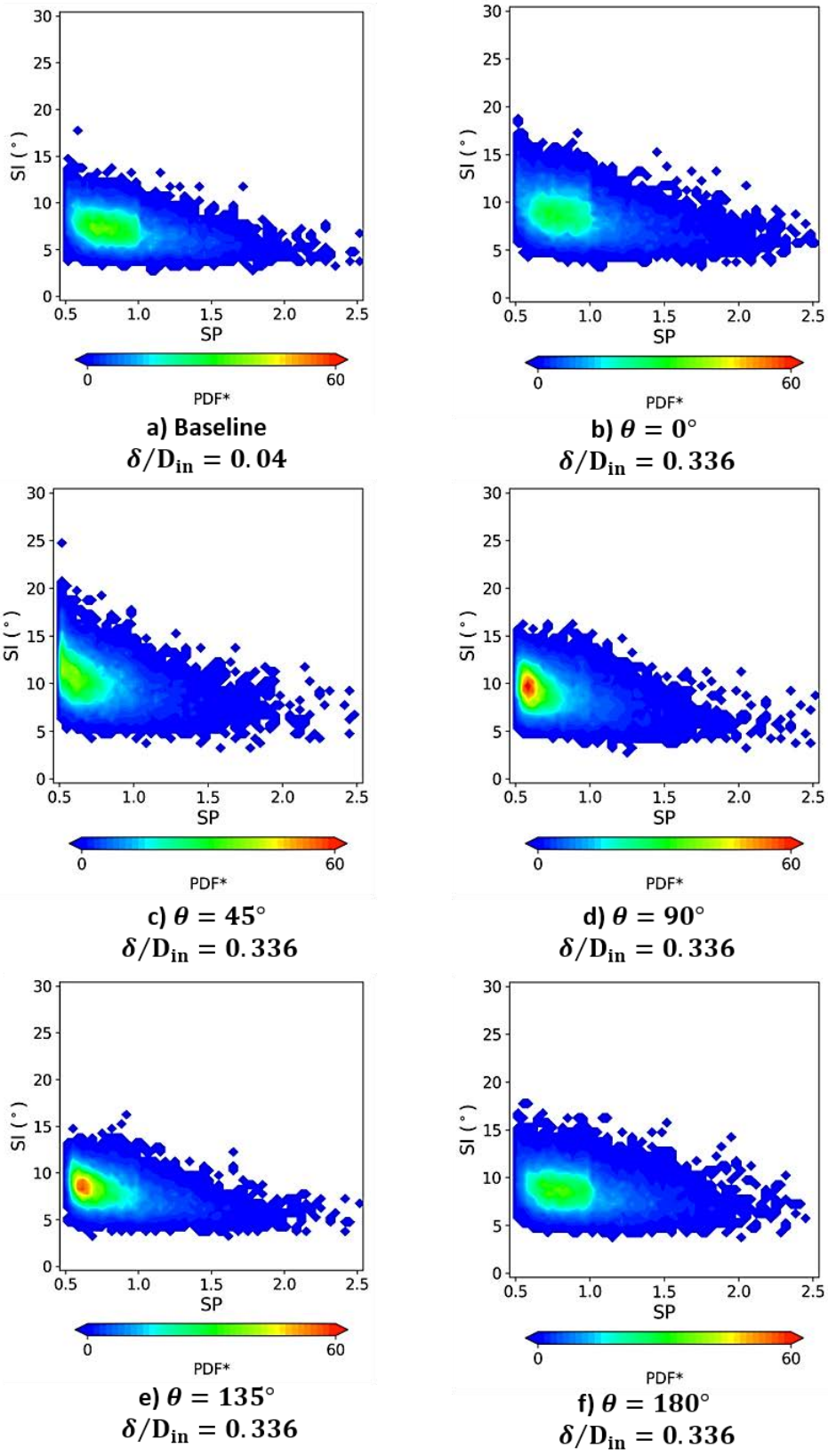

Figure 4-18: SI_SP probability maps at $r/R_{AIP} = 0.8$ for the baseline and the cases with BL ingestion at θ=0°,45°,90°,135° and 180.

5 SUMMARY AND CONCLUSIONS

In this chapter, a brief summary of the entire MSc work is provided, together with the main findings. The main conclusions are derived, and the impact of the work is discussed.

5.1 Project summary

This MSc work aims to quantify the unsteady flow distortion at the Aerodynamic Interface Plane (AIP) of a high-offset S-duct caused by the ingestion of a non-uniform flow profile at different inlet locations with the Stereoscopic Particle Image Velocimetry (S-PIV) technique. S-PIV is a non-intrusive optical technique that allows to acquire unsteady synchronous flow measurements with a high spatial resolution, necessary to accurately assess the phenomenon. Current industry practice relies on intrusive rakes with low spatial resolution that are insufficient to capture the nature of the flow and underestimate the swirl distortion, therefore a lack of knowledge exists about the unsteady characteristics of the distortion metrics and the nature of the unsteadiness in the velocity field.

The experiment took place in a bespoke facility at Cranfield University, modularly designed to host a range of different S-ducts and to allow good optical access to enable S-PIV measurements at the Aerodynamic Interface Plane (AIP), located 61 mm after the S-duct exit. The duct used for the measurements, with an S shape, is designed with the same non-dimensional geometry investigated by Wellborn et al. [25] and Garnier [34]. The operating condition of the rig was set to $M_{ref} = 0.27$, quantified at the calibration reference plane upstream the duct inlet. To re-create a boundary layer profile of $\delta/D_{in} = 0.336$ thickness, that is the same profile studied by Giuliani [9], a 3D printed distortion screen in polylactic acid was placed at a distance $L_{screen} = 2.55D_{in}$ from the S-duct entrance, where $D_{in} = 121.6\,mm$ indicates the diameter of the inlet cross-sectional area of the duct. Five rotations were applied to the distortion screen during the experimental measurements, to obtain five different boundary layer ingestion locations. The studied cases with a non-uniform inlet profile were in total five, and presented a boundary layer of $\delta/D_{in} = 0.336$ thickness ingested at $\theta = 0°, 45°, 90°, 135°$ and $180°$, with θ being the clockwise angle between the vertical axis of symmetry of the fixed duct inlet plane and the local vertical axis of symmetry of the distortion screen, as seen from

a downstream point of view. A baseline case with an almost uniform boundary layer profile of $\delta/D_{in} = 0.04$ thickness was also tested to be used as a reference. For the first time, the cameras of the S-PIV technique were used in portrait mode and tilted of an angle of approximately 15°. The cameras' acquisition frequency was set to 4kHz and 20,000 snapshots were taken in each studied case. The time delay between the two laser pulses was chosen to be $\Delta t = 4\mu s$. This configuration allowed to achieve a final spatial resolution of about $2.1x2.1\ mm$ and 3095 velocity vectors were detected at the AIP. After the measurements, the images were processed with Davis 8.3.1 commercial software through a list of operations that was selected among others to provide the best output. Finally, the results were post-processed with the software CUData-PRO and plotted with the commercial software Techplot.

5.2 Conclusions

Overall, the time-averaged results of the baseline case are characterised by high distortion levels connected to the use of a high-offset duct, whose values are in line with the study of Zachos et al [4]. The ingestion of a thick boundary layer enhances the levels of distortion, with ranges and patterns that highly depend on the ingestion location. If the BL ingestion location is outside the vertical axis of symmetry of the S-duct inlet plane, substantial changes in the flow distortion distribution are observed, both in terms of peak values and distortion patterns, and the case with BL ingestion at $\theta = 45°$ is demonstrated to be the most affected. The secondary flows are also enhanced with high horizontal velocities with values up to three times higher than in the baseline case. Consequently, strong swirling regions appear with increased swirl angles and patterns that tend toward bulk swirl pairs. If the BL is ingested along the vertical axis, the ranges and regions of the secondary flows and swirl angles are only slightly stressed, and the antisymmetric distribution of the in-plane velocities, as well as the classical pair of twin swirl pattern, is maintained. The main differences are observed in the patterns of the out-of-plane velocity.

High values of unsteadiness are observed in all the cases, and they are partially due to the presence of mis-calculated vector maps in the dataset. Unlike previous works [4] [33], the out-of-plane unsteadiness is observed at the top of the AIP, in the same area of the time-averaged high axial velocity values, which is more typical of flow fields characterised by higher Mach numbers. The unsteadiness peak values and distributions

of the cases with boundary layer ingestion at $\theta = 0°, 45°$ and $180°$ increase with respect to the baseline case in all the three velocity components and swirl angle fluctuations, while they decrease in case of BLI at $\theta = 90°$ and $135°$. The horizontal unsteady pattern is approximately located between the regions of high and low time-averaged horizontal velocity magnitudes, while the vertical one coincides with the region of loss of the time-averaged axial velocity. The peak values of the unsteady swirl angles are not particularly affected, despite the presence of strong secondary flows. However, a dominant bulk swirl pattern is observed in the cases with BL ingestion at $\theta = 90°$ and $135°$.

The flow field is highly unsteady, therefore unsteady, synchronous and high-spatial resolution measurements are necessary to quantify the flow distortion caused by the boundary layer ingestion at the AIP of a complex intake. This is important especially for the assessment of the swirl distortion, whose intensity and pattern highly affect the performance of the downstream engine. Conventional measurements underestimate the swirl distortion, while steady measurements are found to result in misleading conclusions. Area-averaged parameters are good means of measure only for an initial overview of the swirl distortion behaviour, since an analysis of the swirl distortion behaviour at different radial positions is fundamental for the correct understanding of the problem. Stereoscopic Particle Image Velocimetry has been demonstrated to be a feasible and accurate experimental technique for the acquisition of unsteady flow distortion measurements and great benefits derive from the observation of the unsteady flow fields.

The unsteady swirl distortion measurements evidence that the pattern of the unsteady swirl distortion significantly deviates from the classical twin swirl configuration observed in the time-averaged flow field. Overall, one-per-revolution patterns are more probable and intense, even though multiple swirling regions with lower intensities and probabilities to appear are observed in all the cases at all radial positions. At the inner most radial position of all the cases the swirl patterns are mainly driven by twin and bulk swirl configurations that are associated with the most intense swirl distortion levels. At a medium location the tendency inverts, and bulk swirl patterns dominate the flow. However, some high values of SI are also associated with twin swirl patterns, especially with BL ingestion at $\theta = 0°$ and $90°$, but they are more isolated cases. Near the duct wall, the flow patterns highly depend on the BL ingestion location. High intensities are equally

shared between bulk and twin one-per-revolution swirl pair events in the case with boundary layer ingestion at $\theta = 90°$, even though bulk swirl events predominate. Twin swirl pairs and bulk swirl events characterize the swirl distortion near the wall in the baseline and in the cases with boundary layer ingestion along the vertical axis, but bulk swirl events tend to promote the most intense swirl distortions. Finally, when the BL is ingested at $\theta = 135°$, twin swirl events are more intense, even though bulk swirl patterns are more likely to appear. Among all the cases with BL ingestion, the case with BL ingestion at $\theta = 135°$ produces the lowest levels of SI in all radial positions.

The ingestion of a non-uniform flow profile at different inlet locations highly affects the unsteady swirl distortion. Increased intensity levels are observed at the most-inner radial position where also the highest fluctuations and standard deviation values are observed. Among all, the highest peak is presented by the case with BL ingestion at $\theta = 45°$. Consequently, the regions at the hub of the compressor blades in the downstream machine are the most affected by the distorted flow. Despite this, the highest fluctuations with respect to the area-averaged value of intensity are still observed in the baseline. The BL ingestion at $\theta = 90°$ and $135°$ consistently reduce the flow unsteadiness, and the latter case overall presents the best performance between all the studied cases at almost all the radial positions investigated. Generally, with the exception of the axial velocity component, the cases that ingest the non-uniform flow profile along the vertical axis of symmetry present magnitudes and patterns of distortion that are more similar to the baseline case than the other ingestion locations.

5.3 Impact of this MSc work

In the industrial practice, flow distortion is conventionally quantified with the use of pressure probes that asses the flow field in terms of total pressure. The method is intrusive, and it cannot provide reliable results after the measurement plane. Moreover, it has a reduced spatial resolution that is insufficient to capture the complex and unsteady nature of the flow field at the exit of a S-duct. In this work, Stereo Particle Image Velocimetry (S-PIV) has been proven to be a feasible and reliable technique for unsteady measurements of velocity fields at the exit of complex intakes, with a higher spatial resolution than traditional methods. In addition, it has been demonstrated to be a feasible technique for measurements of unsteady velocity field caused by the ingestion of non-

uniform flow profiles. Higher levels of flow distortion and unsteadiness have been quantified connected to the ingestion of a boundary layer profile. The data give access to greater understanding of the aerodynamic performance of the S-duct, that can educate the design process of new propulsion system integration technologies. Overall, S-PIV allows to have an accurate understanding of the flow field at the S-duct exit, responsible to cause engine instabilities and lower fan performances.

The camera configuration in portrait mode used for the current work demonstrated to increase the spatial resolution of the experiment, with respect to previous results obtained within the Cranfield research group. Higher levels of unsteadiness were in fact detected in the baseline case, even though partially connected to the presence of mis-calculated vector maps in the dataset. However, high levels of background noise were also detected in the upper part of the cameras' snapshots, potentially connected to the tilted angle of the cameras, responsible for an increase in the portion of glass that the cameras' sensor has to penetrate to reach the AIP plane.

The use of a 3D-printed distortion screen was proven to be a useful device to re-create the ingestion of a boundary layer profile during an experimental measurement. In addition, different distortion screen rotations allowed to correctly simulate the ingestion of non-uniform flow profiles at different inlet locations of the duct.

Swirl distortion is an important source of instabilities for engines that rely on the boundary layer ingestion technology. High-offset S-ducts were proven to be affected by flow distortion and separation [4] [33], and the impact of such distorted flow fields on the downstream machine is consistent. Despite this, little attention appears to have been given to the problem in the open literature, and much needs to still be investigated. Stereoscopic Particle Image Velocimetry (S-PIV) applied at the Aerodynamic Interface Plane of a curved duct has been demonstrated to be an adapt experimental technique to investigate unsteady swirl distortion with adequate levels of accuracy. High levels of swirl distortion have been detected at the exit of curved ducts. Moreover, the ingestion of a thick boundary layer was demonstrated to cause even stronger swirl distortion levels. The results obtained in this work provide good swirl distortion data that can be considered at early stages of the design process of new engine technologies.

Steady swirl data have been demonstrated to result in misleading conclusions about the intensity of swirl distortion, as well as its pattern and location. Unsteady flow measurements are therefore recommended if an accurate analysis of the swirl distortion is needed.

Swirl distortion has been proven to be strongly dependant on the boundary layer ingestion location. Overall, changes in swirl distortion intensity, fluctuations and patterns are observed, that have the potential to differently and strongly affect the downstream machine. A good knowledge of the phenomenon at early stages of the design process can potentially de-risk the development programs of new aircraft concepts and technologies. In addition, expensive and time-consuming changes at later stages of the engine development can be avoided.

Despite good results and findings have been achieved, it is not possible to quantify the amount of flow distortion introduced by the faulty laser timing stabiliser device in the dataset. Overall, higher levels of unsteadiness than Zachos et al. [4] have been evidenced in the baseline case of this work, and it has not been possible to separate the amount of unsteadiness introduced by the increased spatial resolution provided by the camera in portrait mode from that introduced by the presence of mis-calculated vector maps. Moreover, the affected snapshots were found in different percentages in each studied case. The problem was detected only at an advanced stage of this work and it slightly affects the reliability of this results.

6 FUTURE WORK

In this chapter some ideas of future work are provided, to improve the work done in this work and complement the findings.

6.1 Improvements

Despite the measurements taken for this work have allowed to obtain good results and interesting finding, the measurement of another dataset with the same duct geometry, distortion screen and flow operating conditions, but with a fully-functionable laser timing stabilizer device is suggested. The amount of disturbance introduced by the faulty laser timing stabiliser device can therefore be avoided and the real contribution of the cameras in portrait mode assessed. Moreover, additional improvements to this work could be to increase the amount of seeding particle injected in the flow field, together with a higher level of illumination. These two aspects should help to reduce the regions of low seeding and to further improve the quality of the measurements.

Since the ingestion of a non-uniform flow profile at different duct inlet locations is studied for the first time, this work could also be complemented with a frequency analysis applied to both the flow field and the swirl distortion metrics. The frequency analysis would be useful to identify the main frequencies of the flow distortion, as the frequencies that are lower than the critical frequency of the minimum response time of the fan (St_{crit}) greatly affect the engine [33]. Moreover, also the Proper orthogonal decomposition (POD) of the three velocity components could be applied, to determine the most energetic, determinist and coherent structures in the flow fields.

6.2 Comparison with computational methods

Unsteady swirl distortion is a major concern for the engine stability for new concepts of integrated propulsion that rely on complex intakes. This work has demonstrated for the first time that the ingestion of a non-uniform inlet flow profile introduces additional flow distortion. Moreover, different peak values and patterns have also been demonstrated with the ingestion of the non-uniform flow profile at different inlet locations. A comparison of this work with the findings of computational methods investigating the same cases with the same boundary conditions could complement this work and provide useful

information about the reliability of the results, both in terms of flow and swirl distortion. The final aim in the long terms would me to develop a reliable computational method able to assess the flow distortion of different non-uniform flow profiles at different duct locations without the need for the experimental verification. Experimental measurements are in fact expensive, time-consuming and delicate. In addition, their accuracy partially depends also on human and atmospheric external factors.

6.3 Effect of the engine presence on the flow distortion

The flow field studied in this work entered a duct at whose end the presence of an engine was missing. Despite important conclusions can be derived, the presence of the engine has been proved to affect the distortion of the flow upstream [41][42][43]. Measurements taken in S-duct without the presence of the engine tend to overestimate the distortion in the flow field with respect to those observed in flight conditions [41]. Moreover, the presence of the engine can result in delayed flow separations and lower levels of distortion in straight intakes that operate at high angles of attack [42]. Despite these results, the effect of the engine in the upstream flow distortion characteristics has been investigated only in straight intakes, but never in S-ducts. Gil-Prieto designed and 3D-printed a static blockage device similar to the one proposed by Larkin and Schweiger, able to choke the flow for a reference Mach number $M_{ref} = 0.27$ [33]. The device was mounted on a cylindrical section that was placed at the S-duct outlet. Since the device obstructed the cameras 'view, they had to be located upstream of the measurement plane. A transparent S-duct was appositely designed for the experiment. However, no results of adequate quality were obtained due to high reflections of the transparent duct. Nonetheless, the measurement of the engine impact on the upstream flow field in convoluted S-duct would be a great step ahead in the literature, and even more accurate measurements of the unsteady flow distortion could be achieved, and more realistic data would be implemented and used in the industrial design process.

6.4 Further distortion screens investigations

This work provides for the first time an overview of the flow distortion measured at the Aerodynamic Interface Plane of curved ducts. However, more numerous and accurate datasets need to be provided to have a wider understanding of the phenomenon, that is of

great importance due to the recent interest in the industry on embedded propulsion systems that feature boundary layer ingestion (BLI). It is therefore recommended to further investigate the ingestion of non-uniform flow profiles on intakes with different curvatures and shapes and at different reference Mach numbers. Moreover, it is also recommended to design and test different shapes of distortion screens of different materials, able provide various non-uniform profiles. While doing this, a consistent design method for the distortion screens should be developed, to be able to reproduce them systematically and not to introduce disturbances due to the manufacturing process.

6.5 Pressure field reconstruction from velocity fields

Previous works exist both terms of swirl distortion and total pressure distortion, but there is a lack of knowledge about the relationship between the two aspects. A greater understanding is important, since the combination of total pressure and swirl distortion has been seen to cause great reductions of the engine surge margin [5][7]. Conventional pressure measurements are intrusive and modify the downstream flow field, therefore cannot be combined with the S-PIV technique. To be able to extract the pressure field from the velocity data, some early studies have been performed at Cranfield University [8], and different reconstruction methods have been assessed based on representative steady and unsteady computational simulations. The results of this early study show that the distortion metrics can be quite accurately predicted, and there is margin for further investigations. It is therefore recommended to continue the study and to apply the pressure reconstruction methods to experimental data. Once the pressure field is reconstructed, the combination of probability maps of both swirl and total pressure distortion descriptors should be studied. Finally, it is suggested to perform the study on experimental data coming from the measurements of both uniform and non-uniform flow profiles.

REFERENCES

[1] Rutherford D. and M. Zeinali, “Fuel efficiency trends for new commercial jet aircraft. Technical report,” 2015.

[2] W. Thollet, “Modélisations simplifiées de turbomachines pour l’analyse par la simulation des installations motrices complexes d’avions/Body force modeling of fan-airframe interactions,” 2017.

[3] D. K. Hall, “Aircraft Propulsor Modeling and Design for Boundary Layer Ingestion Boundary Layer Ingestion (BLI),” *NASA Ames Res. Cent.*, vol. Advanced M, 2017.

[4] P. K. Zachos, D. G. MacManus, D. G. Prieto, and N. Chiereghin, “Flow Distortion Measurements in Convoluted Aeroengine Intakes,” *AIAA J.*, vol. 54, no. 9, pp. 2819–2832, 2016.

[5] A. S. Gohardani, “A Synergistic Glance at the Prospects of Distributed Propulsion Technology and the Electric Aircraft Concept for Future Unmanned Air Vehicles and Commercial/Military Aviation,” *Prog. Aerosp. Sci.*, vol. 57, pp. 25–70.

[6] R. T. Kawai, D. M. Friedman, and L. Serrano, “Blended Wing Body (BWB) Boundary Layer Ingestion (BLI) inlet configuration and system studies,” *NASA Contract Rep.*, vol. 214534, no. December, pp. 1–26, 2006.

[7] SAE, “A Methodology for Assessing Inlet Swirl Distortion,” Warrendale, PA, 2007.

[8] P. K. Zachos, M. Frascella, D. G. MacManus, and D. Gil-Prieto, “Pressure Flowfield and Inlet Flow Distortion Metrics Reconstruction from Velocity Data,” *AIAA J.*, vol. 55, no. 9, pp. 2929–2941, 2017.

[9] J. E. Giuliani and J.-P. Chen, “Fan Response to Boundary-Layer Ingesting Inlet Distortions,” *AIAA J.*, vol. 54, no. 10, pp. 3232–3243, 2016.

[10] M. D. Williams, *Propulsion System Performance and Integration-lecture material*, vol. 1. Cranfield University, 2016.

[11] L. . Smith, “Wake Ingestion Propulsion Benefit,” *J. Propuls. Power*, pp. 74–82, 1993.

[12] A. Plas, “Performance of a Boundary Layer Ingesting Propulsion System,” *Archives*, no. January, p. 114, 2006.

[13] M. Drela, “Making an extraordinary machine better: the D8 aircraft concept.",”

2012.

[14] D. K. Hall, “Analysis of Civil Aircraft Propulsors with Boundar Ingestion y Layer ARCHIVES Signature redacted,” Massachusetts Institute of Technology, 2015.

[15] D. N. Bissinger and T. Breuer, “Encyclopedia of Aerospace Engineering-Volume 8-Basic Principles-Gas Turbine Compatibility-Intake Aerodynamic Aspects,” in *Encyclopedia of Aerospace Engineering*, W. S. Richard Blockley, Ed. John Wiley and Sons, Ltd., 2010.

[16] L. Hardin, G. Tillman, O. Sharma, J. Berton, and D. Arend, “Aircraft System Study of Boundary Layer Ingesting Propulsion,” *48th AIAA/ASME/SAE/ASEE Jt. Propuls. Conf. & Exhib.*, no. August, pp. 1–12, 2012.

[17] R. V. Florea, C. Matalanis, L. W. Hardin, M. Stucky, and A. Shabbir, “Parametric Analysis and Design for Embedded Engine Inlets,” *J. Propuls. Power*, vol. 31, no. 3, pp. 843–850, 2015.

[18] E. J. Gunn and C. A. Hall, “Aerodynamics of Boundary Layer Ingesting Fans,” *Vol. 1A Aircr. Engine; Fans Blowers*, p. V01AT01A024, 2014.

[19] M. B. Greitzer, E. M. and Tan, C. S. and Graf, “Generation of streamwise vorticity and three-dimensional flow,” in *Internal Flow: Concepts and Applications*, First Edit., New York: Cambridge University Press, 2004, p. 736.

[20] N. C. Bissinger and T. Breuer, “Basic Principles - Gas Turbine Compatibility - Inyake Aerodynamic Aspects,” in *Encyclopedia of Aerospace Engineering*, vol. 8, pp. 1–11.

[21] M. Alpe, “Impact of a Fan Simulator on a Complex Aero-engine Intake Aerodynamics,” 2017.

[22] SAE, “Gas Turbine Engine Inlet Flow Distortion Guidelines,” 2002.

[23] T. Bissinger, N. N., and Breuer, “Basic Principles-Gas Turbine Compatibility-Intake Aerodynamics Aspects,” in *Encyclopedia of Aerospace Engineering*, Wiley, Hoboken, NJ, 2010, pp. 1–10.

[24] N. Chiereghin, D. MacManus, M. Savill, and R. Dupuis, “Dynamic Distortion Simulations for Curved Aeronautical Intakes,” Bristol, 2014.

[25] S. R. Wellborn, T. H. Okiishi, and B. A. Reichelbert, “Study of the Compressible Flow in a Diffusing S-Duct,” 1993.

[26] D. G. MacManus, D. G. Chiereghin, N. Gil Prieto, and P. Zachos, “Complex

Aeroengine Intake Ducts and Dynamic Distortion," in *33rd AIAA Applied Aerodynamics Conference, AIAA paper 2015-3304*, 2015.

[27] W. Meyer, W. Pazur, and L. Fottner, "The Influence of Intake Swirl Distorion on the Steady-State Performance of a Low Bypass Twin-Spool Engine," 1991.

[28] B. Bouldin and Y. Sheoran, "Inlet Flow Angularity Descriptors Proposed for Use With Gas Turbine Engines," *SAE Tech. Pap.*, vol. 01-2919, no. 724, 2002.

[29] D. S. Miller, *Internal Flow Systems*. 1978.

[30] SAE, "Inlet Total-Pressure-Distortion Cosiderations for Gas-Turbine Engines," 1999.

[31] M. C. Raffel, S. Willert, J. Wereley, and Kompenhans, *Partcle Image Velocimetry, A Practical Guide*, Second Edi. Springer, 2007.

[32] LaVision GmbH, "FlowMaster," 2016.

[33] D. E. Gil-Prieto, "Unsteady Flow Distortion in Complex Aero-engine Intakes," Cranfield University, 2018.

[34] E. Garnier, "Flow Control by Pulsed Jet in a Curved S-Duct: A Spectral Analysis," *AIAA J.*, vol. 53, no. 10, pp. 2813–2827.

[35] Industries International Photonics Inc., "DM Dual Head Green Series Brochure," 1800 Ocean Avenue, Ronkonkoma, NY 11779, US, 2018.

[36] Vision Research Inc., "Phantom UHS-12 Series Datasheet," 100 Dey Road, Wayne, NJ 07470, US, 2007.

[37] A. Melling, "Tracer particles and seeding for particle image velocimetry," *Meas. Sci. Technol.*, vol. 8, no. 12, pp. 1406–1416.

[38] LaVision GmbH, "Product-Manual for Imaging Tools fro Davis 8.3," Gottingen, 2015.

[39] D. Delot, A. L. and Garnier, E. and Pagan, "Flow Contro in a High-Offset Subsonic Air Intake," in *47th AIAA/ASME/SAE/ASEE Joint Propulsion Conference and Exhibit, AIAA Paper 2011-5569*, 2011, vol. 10.

[40] D. Gil-Prieto, D. G. MacManus, P. K. Zachos, G. Tanguy, F. Wilson, and N. Chiereghin, "Delayed Detached-Eddy Simulation and Particle Image Velocimetry Investigation of S-Duct Flow Distortion," *AIAA J.*, vol. 55, no. 6, pp. 1893–1908, 2017.

[41] D. L. Motycka, "Reynolds Number and Fan/Inlet Coupling Effects on Subsonic

Transport Inlet Distortions," *J. Propuls. Power*, vol. 1, no. 3, pp. 229–234, 1985.

[42] B. K. Hodder, "An Investigation of Engine Influence on Inlet Performance," 1981.

[43] M. J. Larkin, "Ultra high bypass nacelle aerodynamics: Inlet flow-through high angle of attack distortion test," 1992.

APPENDICES

A.1 - New processing tree definition

For the processing to be implemented, the software *Davis 8.3.1* was used, and a new processing tree was defined. New settings were tested and compared with those previously used for the measurements taken with the Cranfield facility. The first step of the processing aims to reduce the background noise by applying a filter. For each image, depending on the filter choice, the minimum, maximum, average or Gaussian average intensity for each pixel position for a certain range (filter length) of images is calculated, and subsequently subtracted before the calculation of the cross-correlation (Figure A.1-1). To define the filter to be applied to this experimental work, an initial parametric study was run on a test case of 200 images (Figure A.1-2). No smoothing was applied to the postprocessed data at this stage.

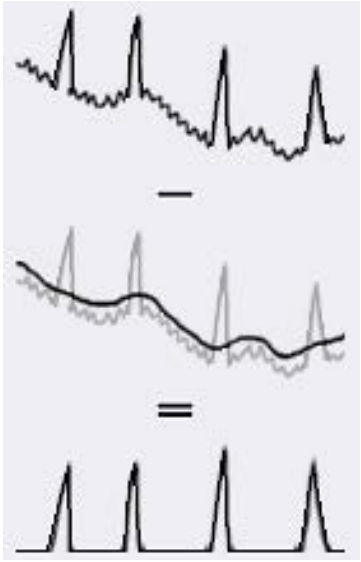

Figure A.1-1: Example of filter application: subtract average filter.

The initial study allowed to immediately exclude the option of the subtract minimum filter. Even though for the results with the cameras in landscape configuration it generally provided the best results, in this case it showed the worst results both in terms of average velocity and correlation value.

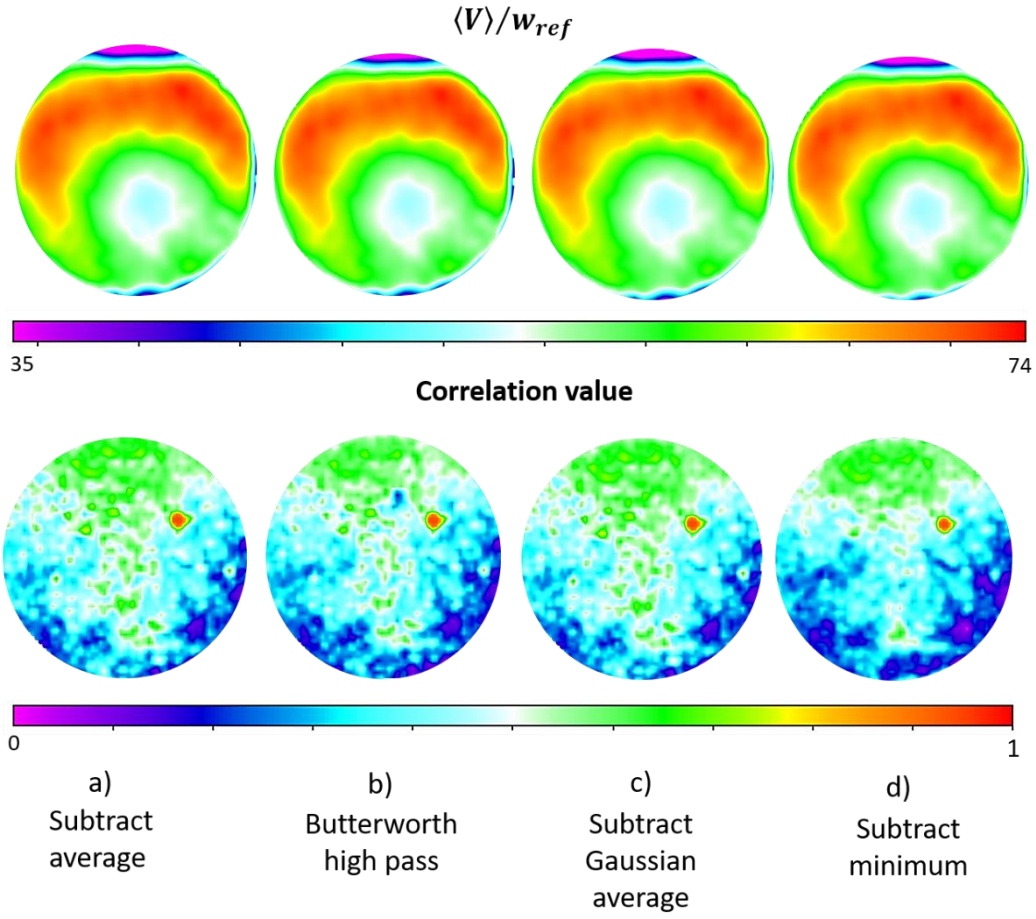

Figure A.1-2: Parametric study to define the filter type to be applied to the test cases. The study was performed on a range of 200 images. Upper row: Average velocity of the three velocity components in m/s. Bottom row: Correlation value.

No particular difference was found among the results provided by the other filters, therefore a new study implemented on the complete images range was necessary (Figure A.1-3). For this study, a smoothing was applied to the postprocessed data. The subtract Gaussian average and Butterworth high pass filters provided less symmetrical average velocity field output than the subtract average filter, and a higher and less symmetrical standard deviation. Moreover, the results provided by the Subtract Gaussian average filter were not good enough to justify its use, since the processing duration required was of approximately 160h, an exaggerated period length if compared to the 24h of processing required by the other two filters. Finally, according to Davis' manual *FlowMaster* [32], the use of the Butterworth filter is justified only if there is a considerable amount of unsteady laser light reflection, while more traditional filtering methods provide good

results when the reflection intensity is constant. Since the amount of reflection during the experimental measurement could be considered approximately constant in the region of interest, the subtract average filter was chosen as the reference filter for the new processing tree.

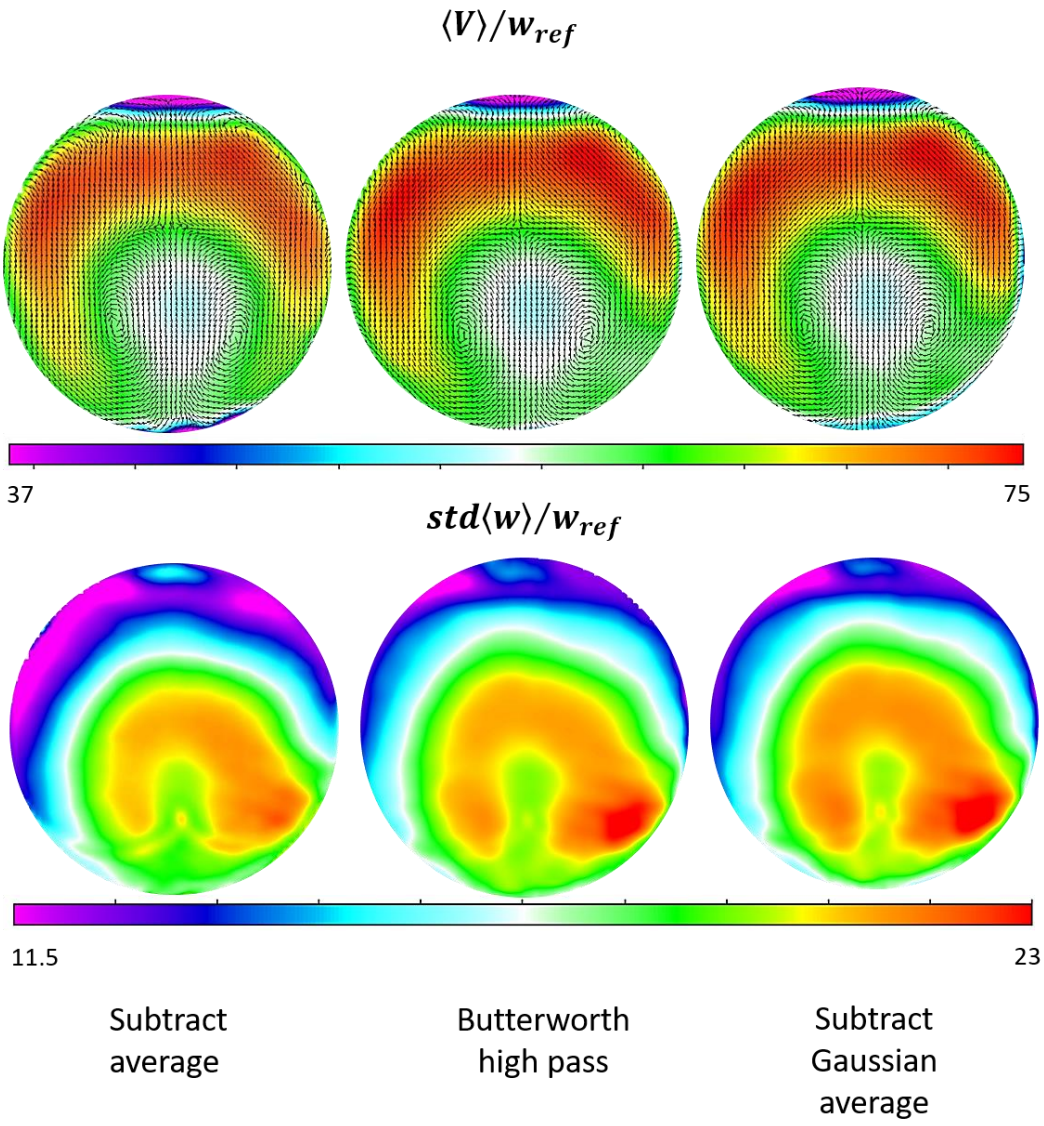

Figure A.1-3: Parametric study to define the filter, applied to a range of 20000 images. Upper row of images: Average velocity of the three velocity components [m/s]. Bottom row of images: average standard deviation [m/s].

For the filter length definition, a comparison between the results provided by the entire range of images and by part of it (filter length) was done. The filter length was set to 999 images, the maximum length allowed by the software, and a comparison between the symmetrical, forward (the last n images get the same information), and backward (the first n images get the same information) modes was studied (Figure A.1-4: Filter length comparison.). Since no evident difference in both the processing duration and the results between the different filter lengths and modes was found, the filter length was set to the entire range of images.

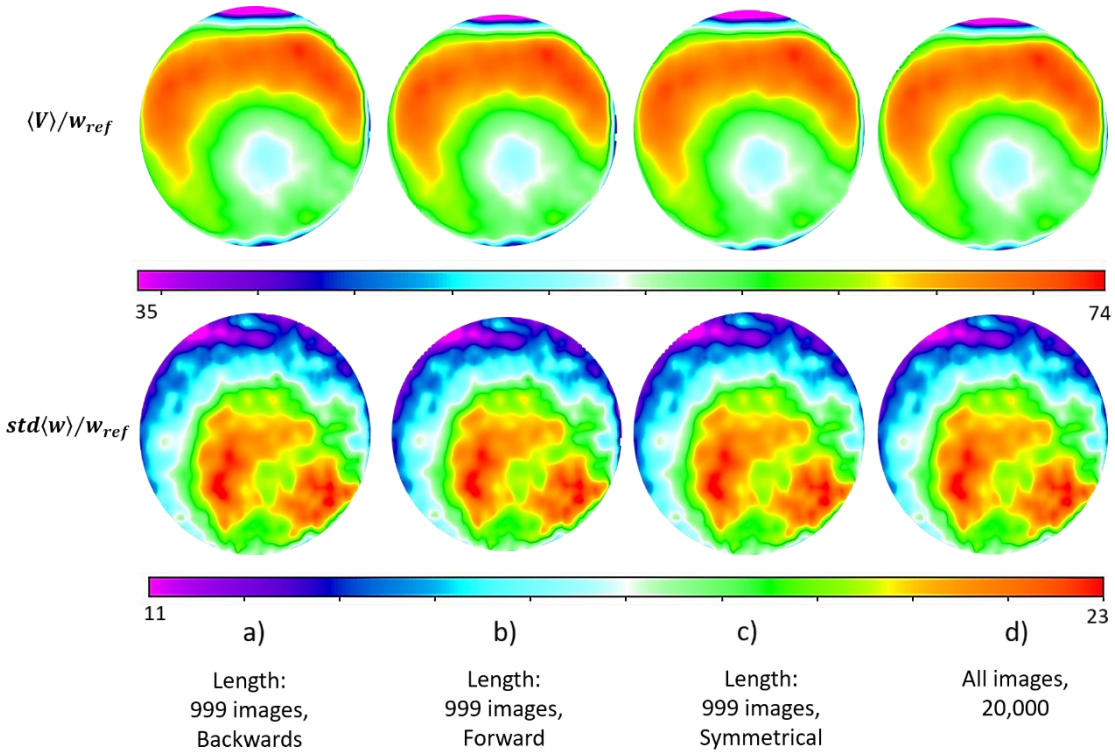

Figure A.1-4: Filter length comparison. Upper row of images: Average velocity of the three components [m/s]. Bottom row of images: average standard deviation [m/s].

Before the vector calculation, a pre-processing was applied, to manipulate the particles and improve the quality of the results. The sliding background was subtracted by the images with a scale length in pixel dimensions of 2. The dimension was well above the double size of the mean particle diameter, as suggested in the manual of Davis software © *FlowMaster* [32].

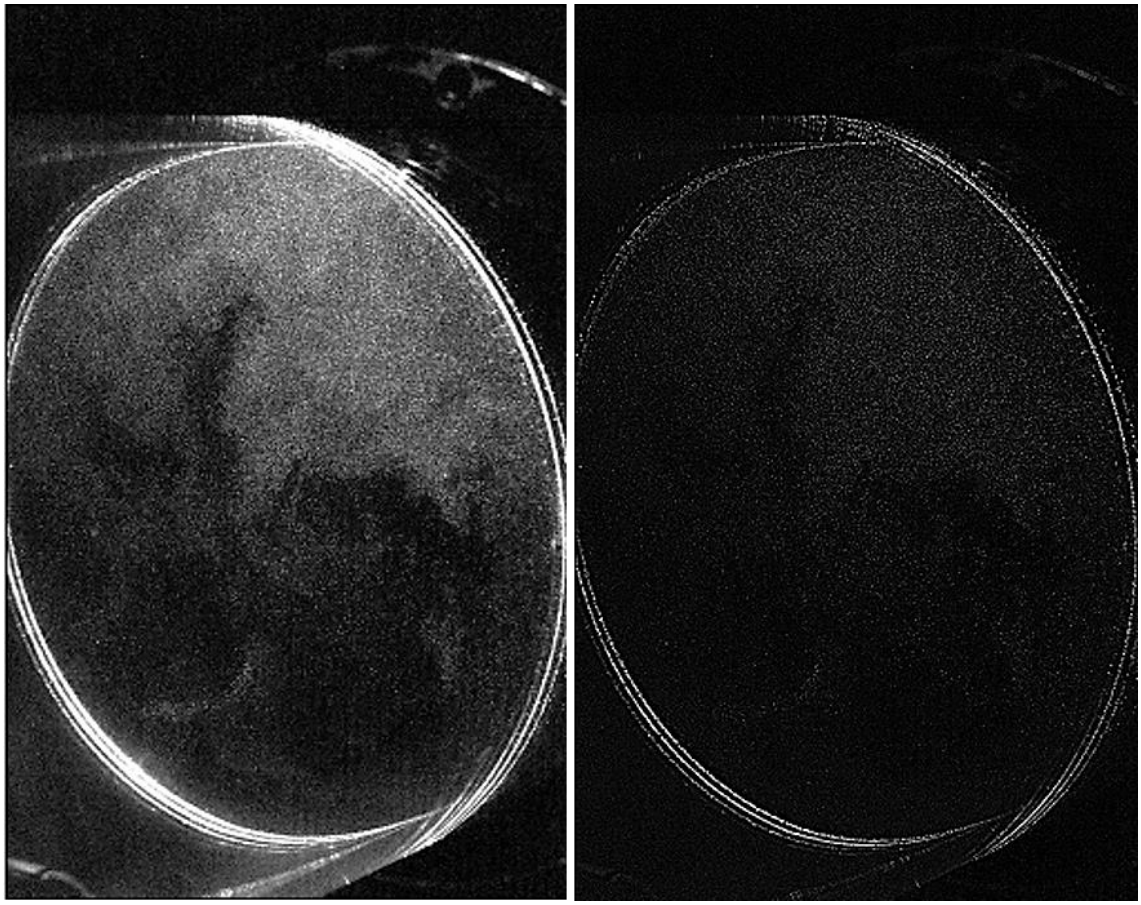

Figure A.1-5: Pre-processing image correction.

The method is particularly useful in presence of intensity fluctuations, and provides corrected images with a constant background level, where the large intensity fluctuations have been filtered [32] (Figure A.1-5).

After the vector pre-processing and before the cross-correlation, the common region of both cameras was manually delimited with the use of a geometric polygonal mask, defined and applied to the entire range of images. This allowed to further consider and calculate only valid pixels, and to take out the consistent wall reflections that would only provide incorrect results. The processing algorithm was based on a GPU cross-correlation method, applied to the masked source of data coming from the cameras. The GPU operation calculates PIV cross-correlation in the Nvidia graphics processing unit (GPU) instead of the computer's central processing unit (CPU) [32]. This allowed to speed up the data processing up to 15 times, without affecting the precision and the robustness of the results [32]. During the correlation process, the image is divided in interrogation

windows, and in the end only one velocity vector per window is yielded. The correlation function acts inside the window on the intensity, and passes through the PIV recording with a certain shift of the window [32]. Since the correlation mode to utilize depends on the camera mode during the experimental acquisition, the stereo cross-correlation mode was selected for this work. The stereo cross-correlation was applied with multi-pass decreasing windows' size. The multi-pass option allows to first reconstruct a reference vector field with the first pass, while for the following pass the window size is half and the previous vector calculated is used as a best-choice window shift [32]. The window shift is therefore adaptively improved along the process. With the selection of the multi-pass option, the image is reconstructed through pixel-mapping, that allows to have a better signal-to-noise ratio of the correlation function, better accuracy of the velocity measurements, and a more suppressed peak locking effect [32]. Window sizes of 128x128, 64x64 and 32x32 are in general preferred in presence of background noise, while for an iteration to converge, the suggested number of passes is usually between two and four.

Comparative studies were performed to select the best windows' size, overlap and passes number for this work. To select the best windows' size, a comparative study was conducted by changing the size and keeping constant the number of passes (Figure A.1-6). In particular, one pass was used for the initial window, and three passes were used for the smallest window, as previous research experience at Cranfield suggested. The study clearly showed that cases a) and c) were the best ones. In the end, case a) was used as a reference case. Figure A.1-7 instead revealed that the best overlap was provided by case a), since the results were more symmetrical in terms of average velocity field, and with more reasonable values in terms of standard deviation. Also in this study, the number of passes was respectively 1 and 3 for the initial and the smallest window. In the end, the study for the final number of passes (Figure A.1-8) showed equal results in terms of standard deviation, but slightly more symmetrical results for case b). Therefore that case was taken as a reference for the new processing tree.

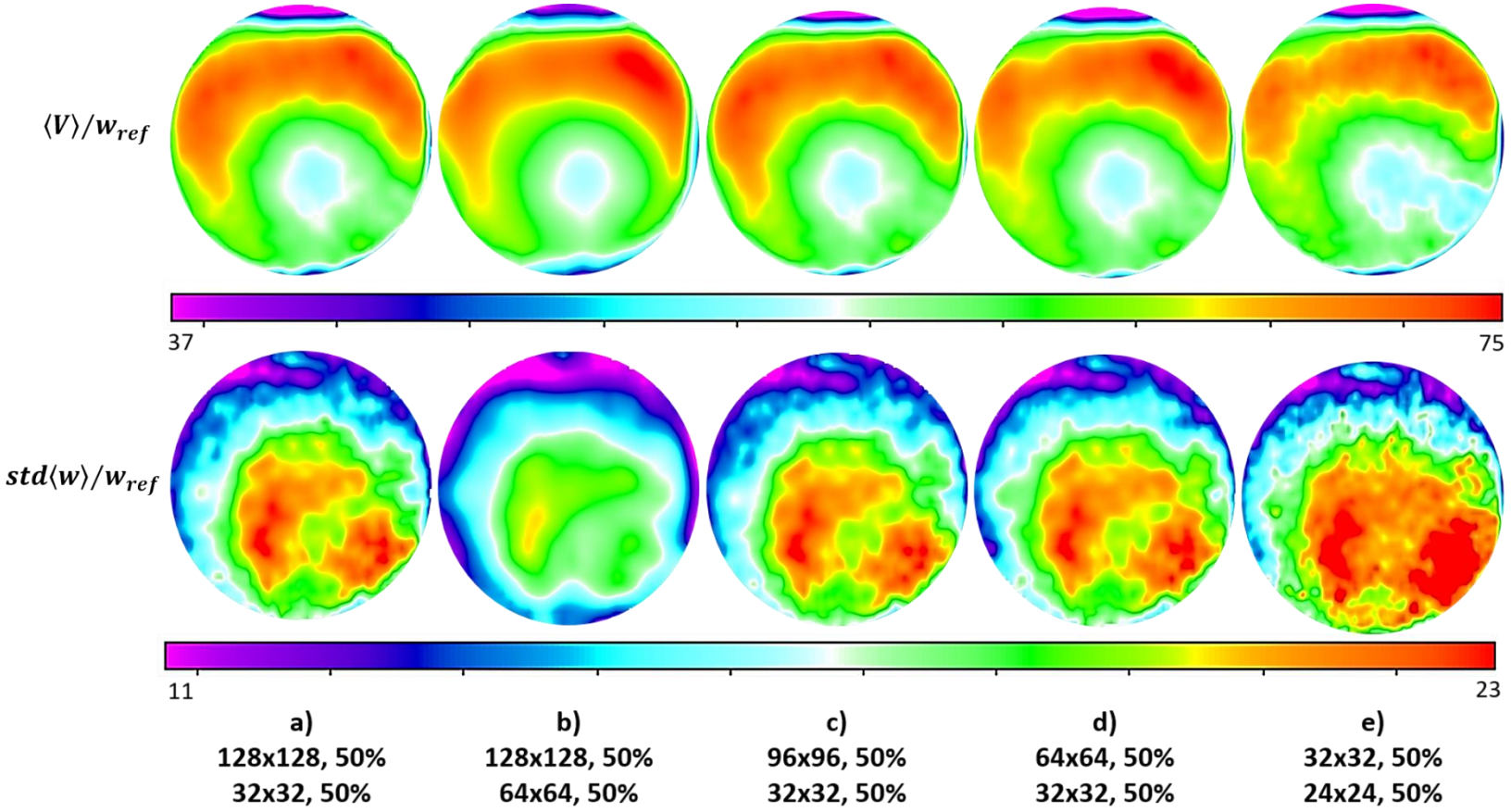

Figure A.1-6: Windows' size comparative study. Upper row: average velocity field of the three velocity components [m/s]. Bottom row: Standard deviation [m/s].

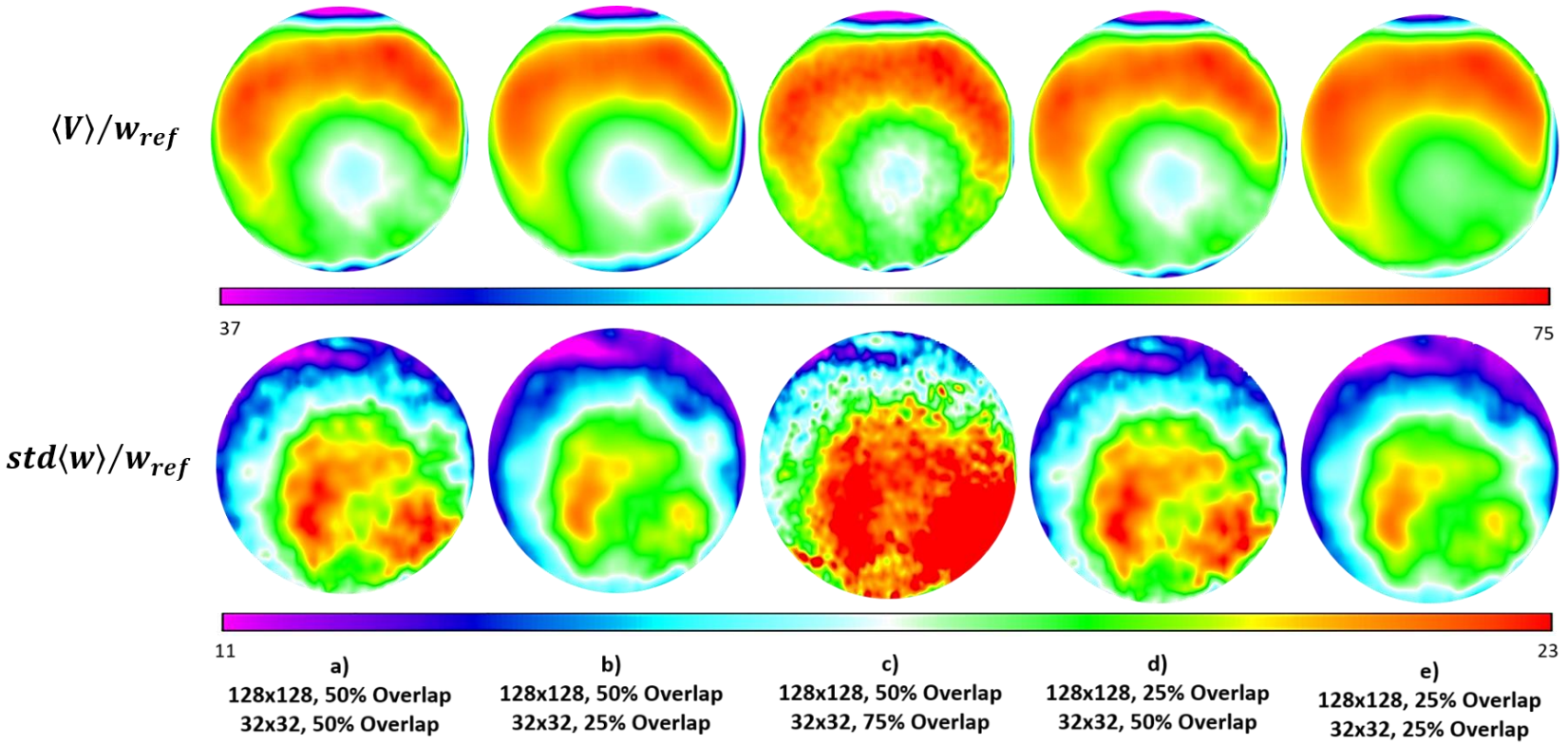

Figure A.1-7: Comparative study for the definition of the windows' overlap. Upper row: average velocity field of the three velocity components [m/s]. Bottom row: average standard deviation [m/s].

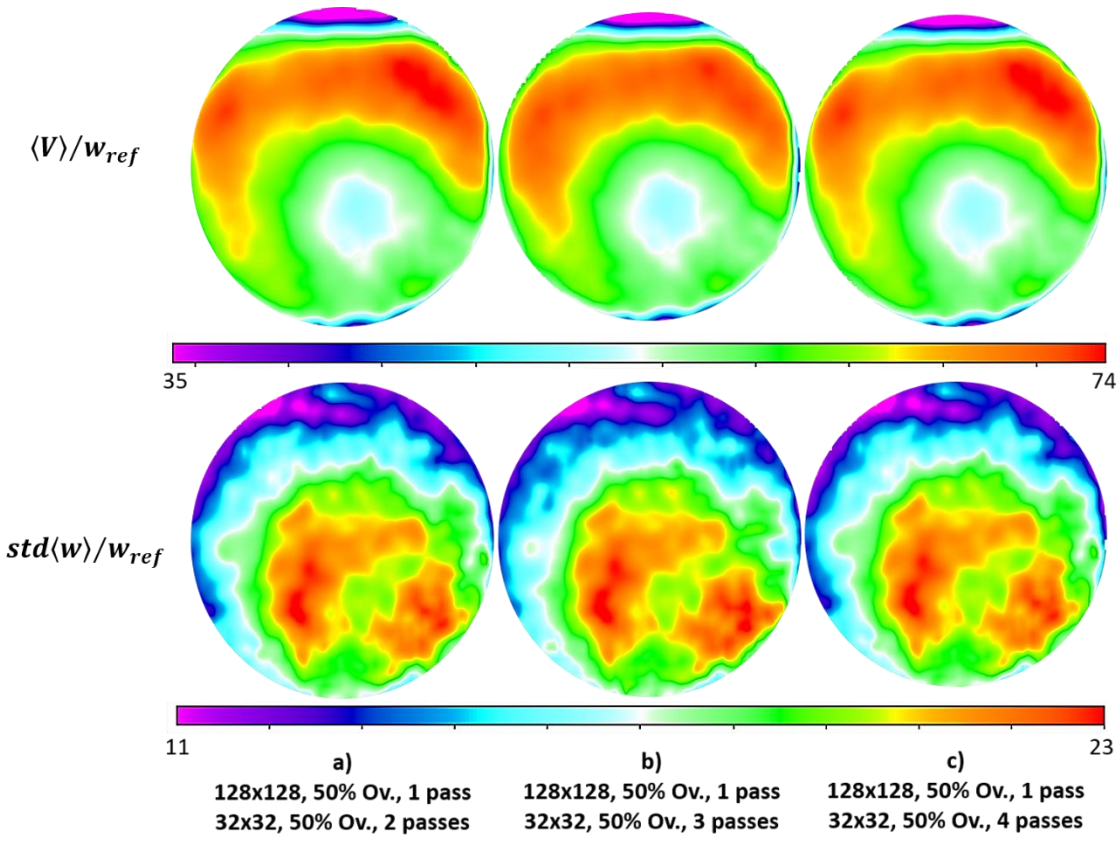

Figure A.1-8: Comparative study for the definition of the ideal number of passes. Upper row: average velocity field of the three velocity components [m/s]. Bottom row: average standard deviation [m/s].

As a consequence of the studies, the total number of passes was 7, and no weighting function was applied. For the first window pass, a window size of 128x128 pixels, with 50% overlap and a maximum shift 0f 4 pixel was used, where maximum shift defines the sized in pixel unit of the resulting correlation function, in which the peak of the correlation is searched [32]. For the second pass, a window of 64x64 pixels, an overlap of 50% and a maximum change in shift of 3 pixels was chosen. For the third, fourth and fifth pass, a window of 32x32 pixels with an overlap of 50% was used, and the maximum change in shift was set to 3 pixels. For the image reconstruction, the initial window shift was set constant, and the maximum reconstruction error for the 3D vector validation was chosen to be equal to three pixels. A multi-pass postprocessing was used to validate each vector field before it was used as a reference for the next pass. During the procedure, spurious vectors were removed with a threshold value bigger than twice the standard deviation of

the neighbour vectors. At the same time, the spaces left by the removed vectors through a data interpolation, and a smoothing with a 3x3 filter was used. After the vector field was calculated, the real vector postprocessing took place. This allowed to remove spurious or false vectors present in the final velocity field. Usually, two good quality indices for the vector postprocessing are the peak ration and the correlation value, and high values of the two parameters indicate good levels of confidence in the calculation.

The peak ratio is defined as [32]:

$$\boldsymbol{Q = \frac{P1-min}{P2-min} > 1} \quad \textbf{(A.1-1)}$$

Where:

- Min = is the lowest value of the correlation plane
- P1 and P2 = are the peak heights of the two highest correlation peaks

The peak ratio is therefore related to the background level or its noise. The correlation value is a value in the range from 0 to 1, where a value of 0 indicates that there is no preferred shift direction detection, and 1 means that the two distributions of intensity are identical and that there is no noise.

The postprocessing took place through some steps. First, a range was defined to restrict the vectors to filter, and the vectors outside the range were deleted. For this work, the range was between 0 and 20 pixels for the three velocity components. Subsequently, vectors with a peak ratio $Q < 1.2$ were deleted. As a third postprocessing step, a median filter was applied. This computes a median vector from a group of neighbouring vectors. Later, it compares the median vectors with the median vector +/- the deviation of the neighbour vectors with the following criteria [32]:

$$\boldsymbol{U_{median} - U_{rms} \leq U \leq U_{median} + U_{rms}} \quad \textbf{(A.1-2)}$$

$$\boldsymbol{V_{median} - V_{rms} \leq V \leq V_{median} + V_{rms}} \quad \textbf{(A.1-3)}$$

$$\boldsymbol{W_{median} - W_{rms} \leq W \leq W_{median} + W_{rms}} \quad \textbf{(A.1-4)}$$

Where:

- U_{median}, V_{median}, W_{median}= median of respectively all U, V, Z components of neighbour vectors
- U_{rms}, V_{rms}, W_{rms} = deviation of respectively U, V, Z components of the neighbour vectors

If the centre vector is outside the range, it is replaced by a vector corresponding to the next highest correlation peak detected within the interrogation window. As suggested in the software manual [32], the threshold for the vector removal was set twice the standard deviation. After the median filter was applied, the group of vectors with less than 5 vectors were removed, and the empty spaces filled up with interpolated vectors. Finally, the final vector field was smoothened by a 3x3 smoothing filter to further reduce the noise.

A.2 Additional probability maps of swirl descriptors and swirl type probabilities

In this appendix, the missing joint-PDF maps of the $SP - SD$ and $SI - SP$ swirl descriptors are reported for the radial positions $r/R_{AIP} = 0.2, 0.3, 0.4, 0.7$ and 0.9 that were not included in Section 4.4. The probability maps have been computed for all the studied cases: baseline, BL ingestion at $\theta = 0°, 45°, 90°, 135°$ and $180°$. A complete table with all the probabilities associated with twin ($P_{twin}(\%)$) and bulk ($P_{bulk}(\%)$) swirl events at the different radial positions is also reported, for all the cases studied.

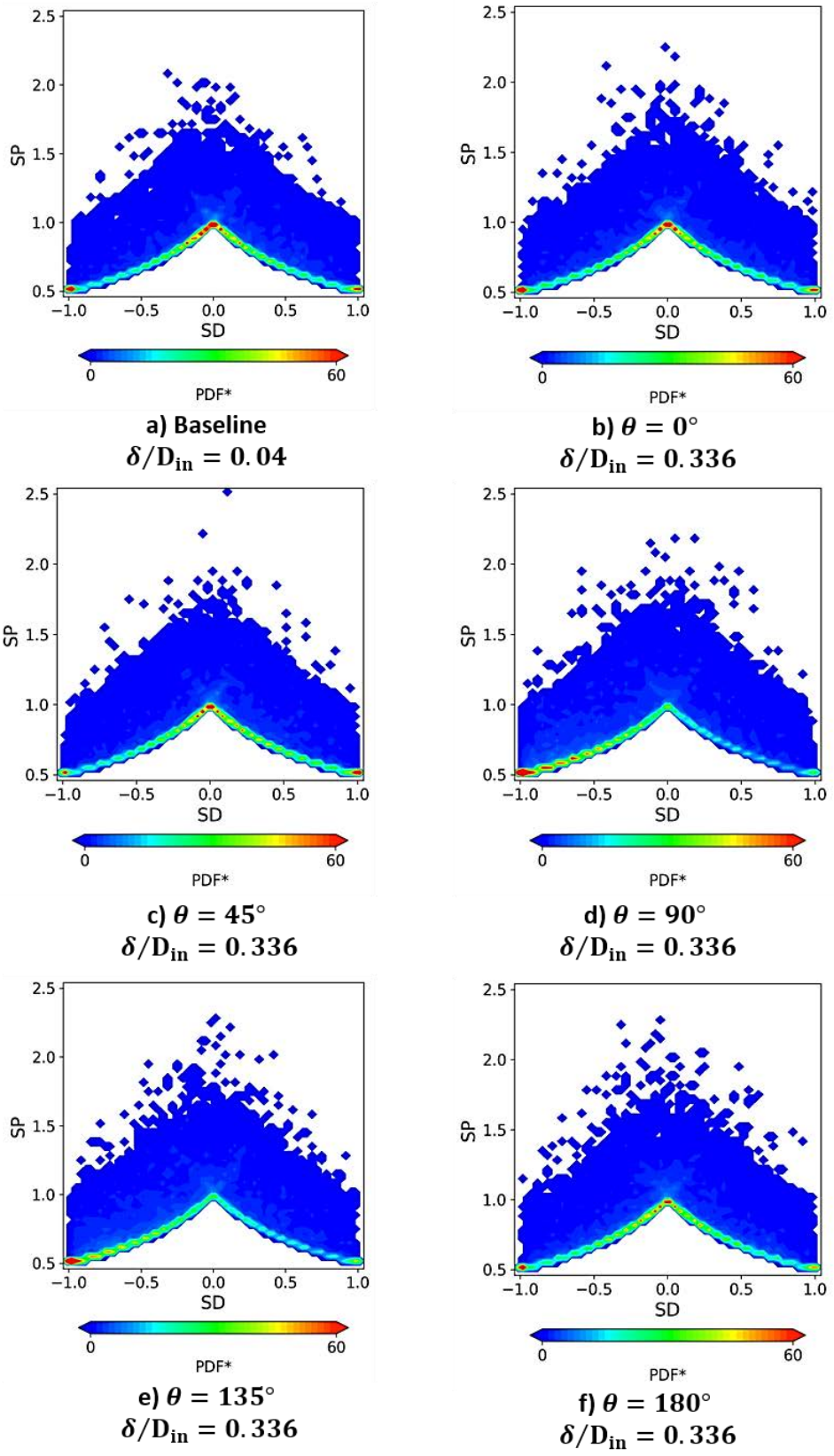

Figure A.2-1: SP_SD probability maps at $r/R_{AIP} = 0.2$ for the baseline and the cases with BL ingestion at θ=0°, 45°, 90°,135° and 180°.

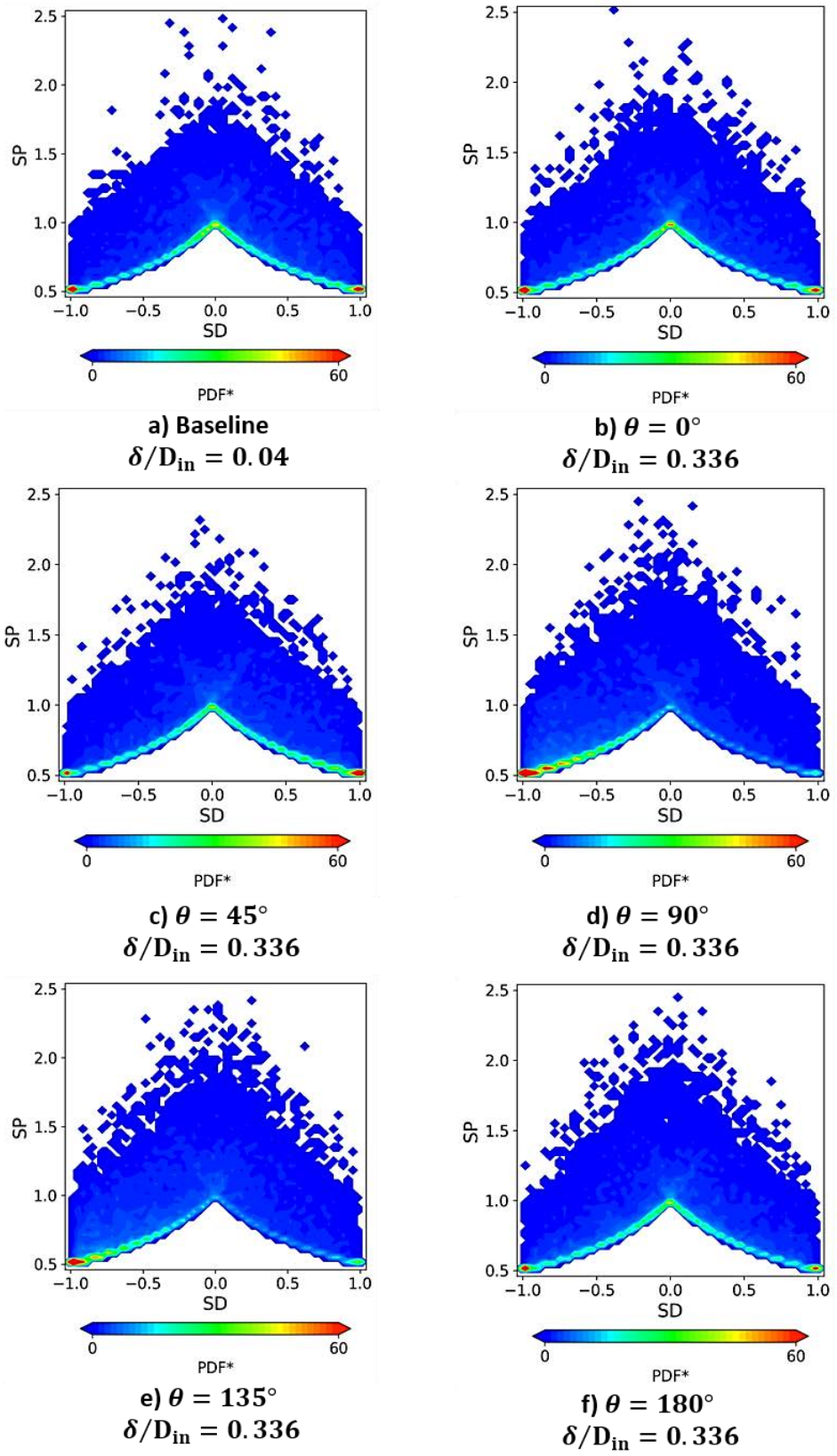

Figure A.2-2: SP_SD probability maps at $r/R_{AIP} = 0.3$ for the baseline and the cases with BL ingestion at θ=0°,45°,90°,135° and 180°.

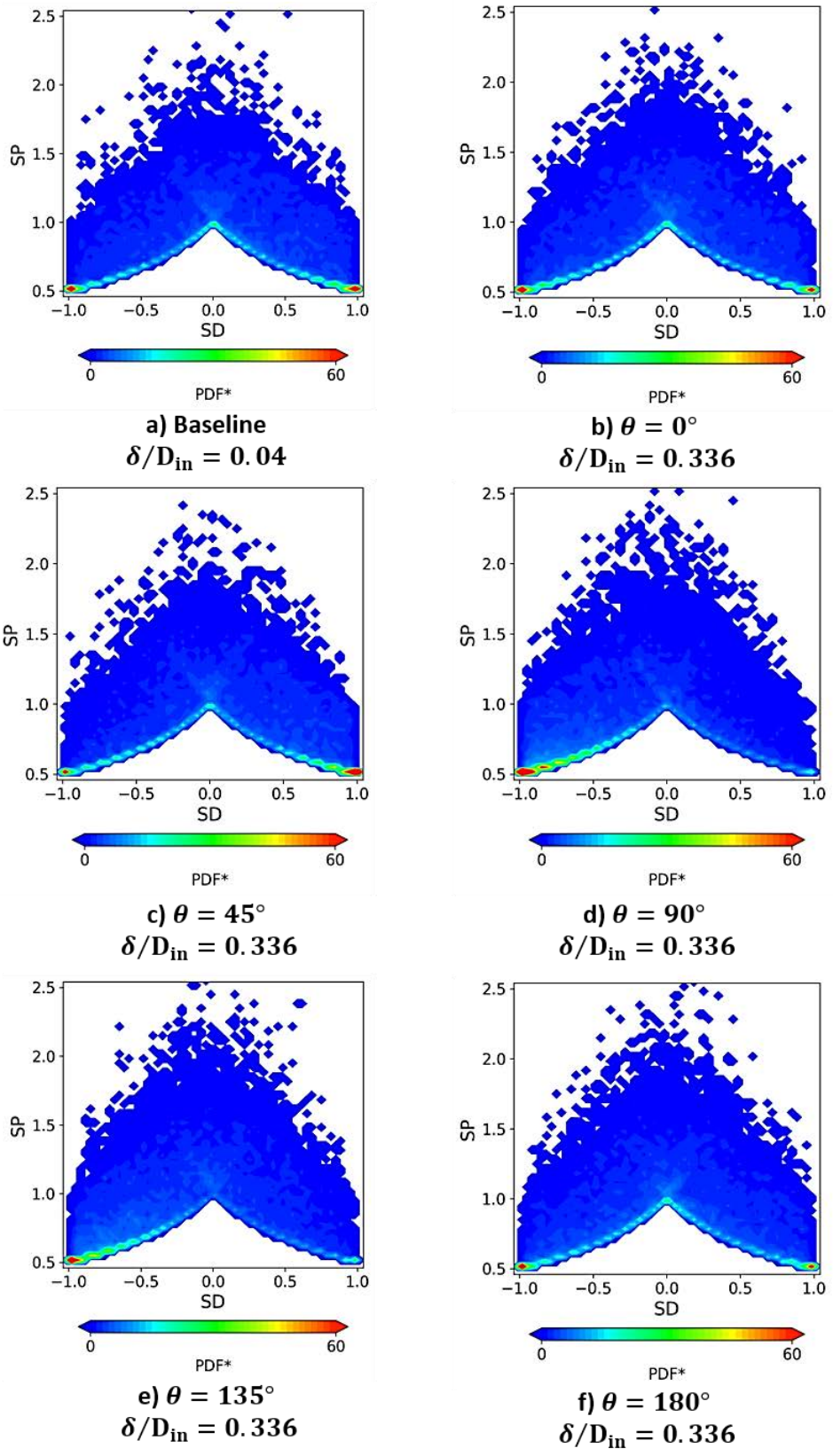

Figure A.2-3: SP_SD probability maps at $r/R_{AIP} = 0.4$ for the baseline and the cases with BL ingestion at θ=0°,45°,90°,135° and 180°.

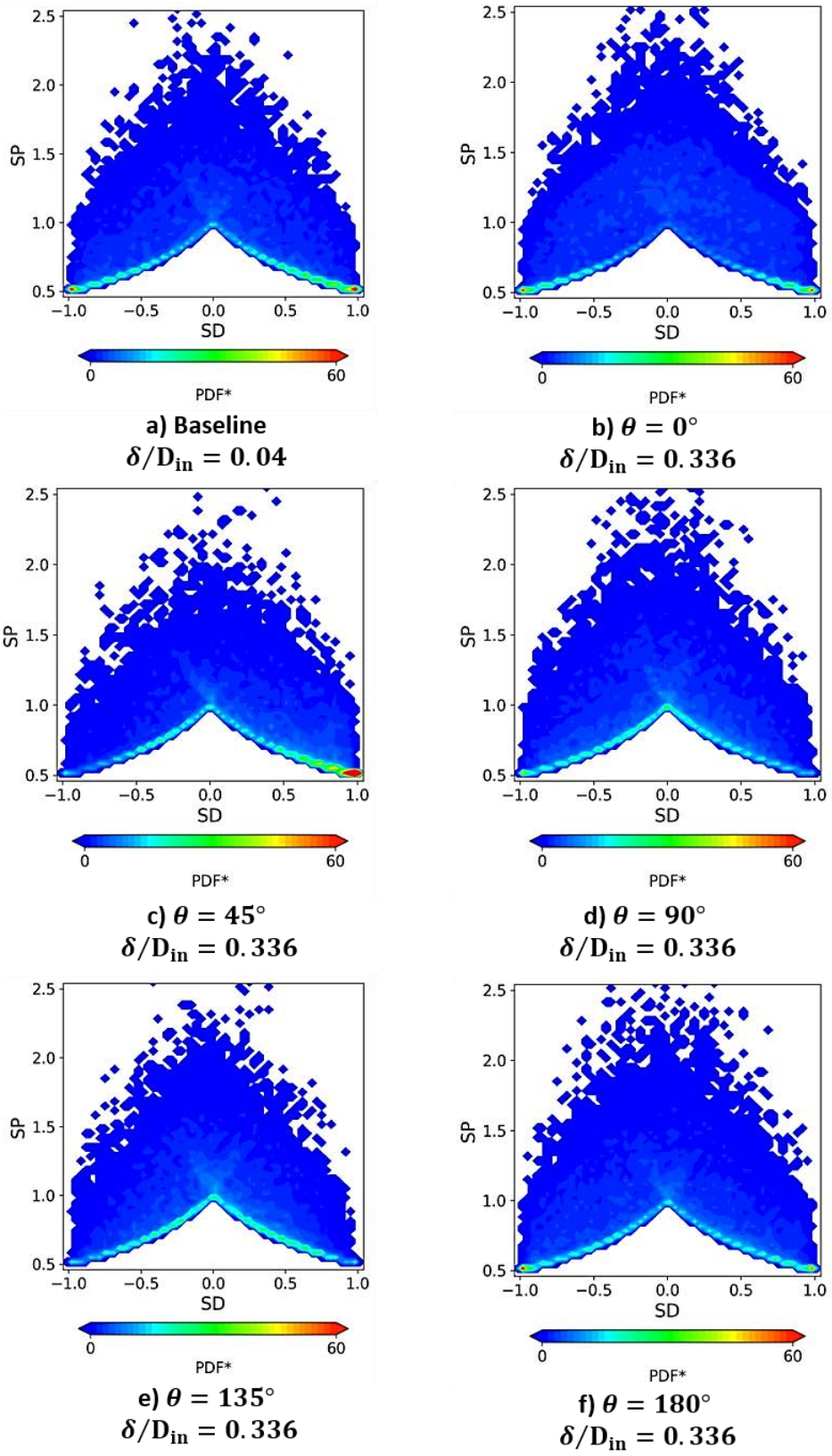

Figure A.2-4: SP_SD probability maps at $r/R_{AIP} = 0.6$ for the baseline and the cases with BL ingestion at θ=0°,45°,90°,135° and 180°.

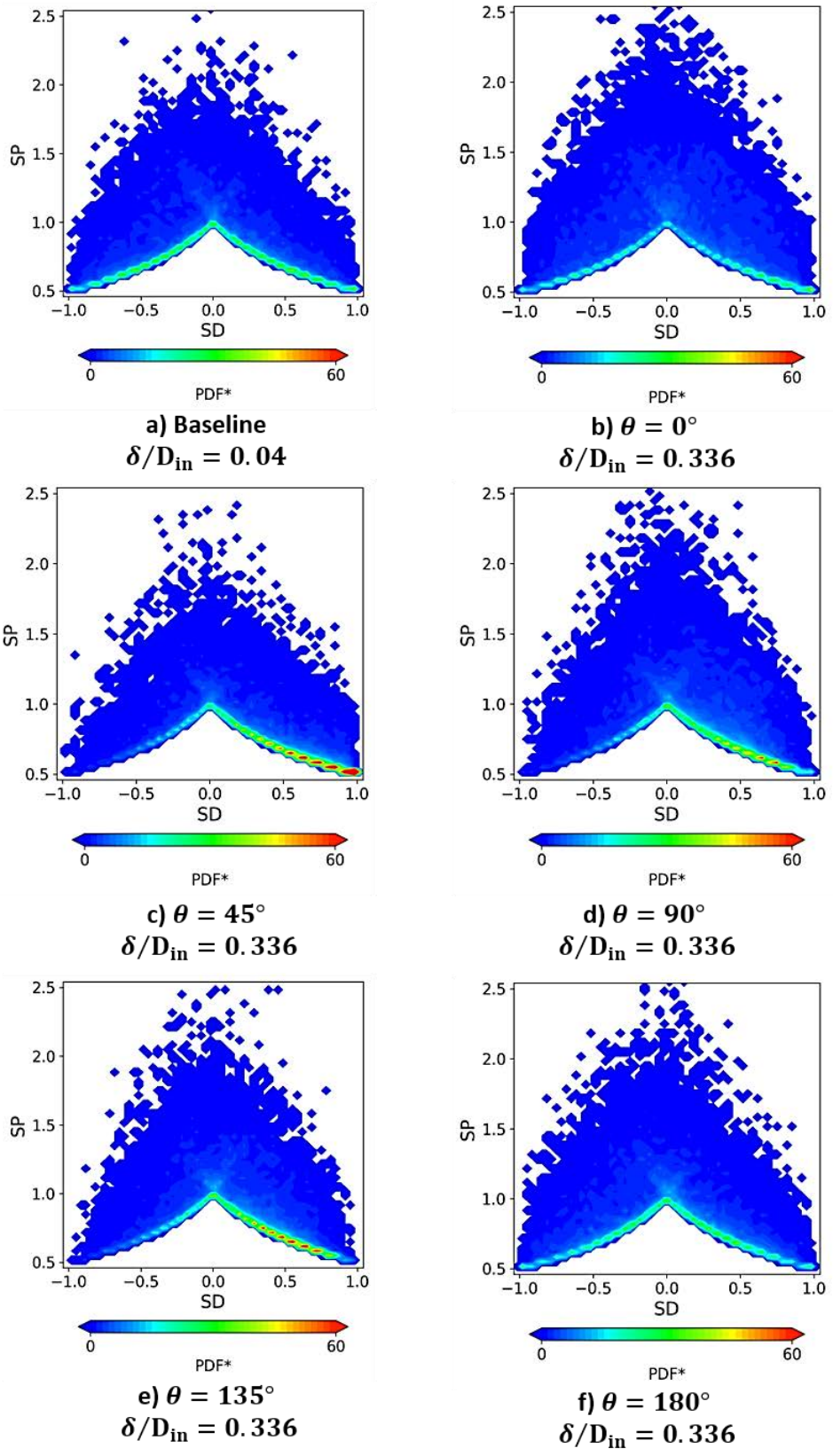

Figure A.2-5: SP_SD probability maps at $r/R_{AIP} = 0.7$ for the baseline and the cases with BL ingestion at θ=0°,45°,90°,135° and 180°.

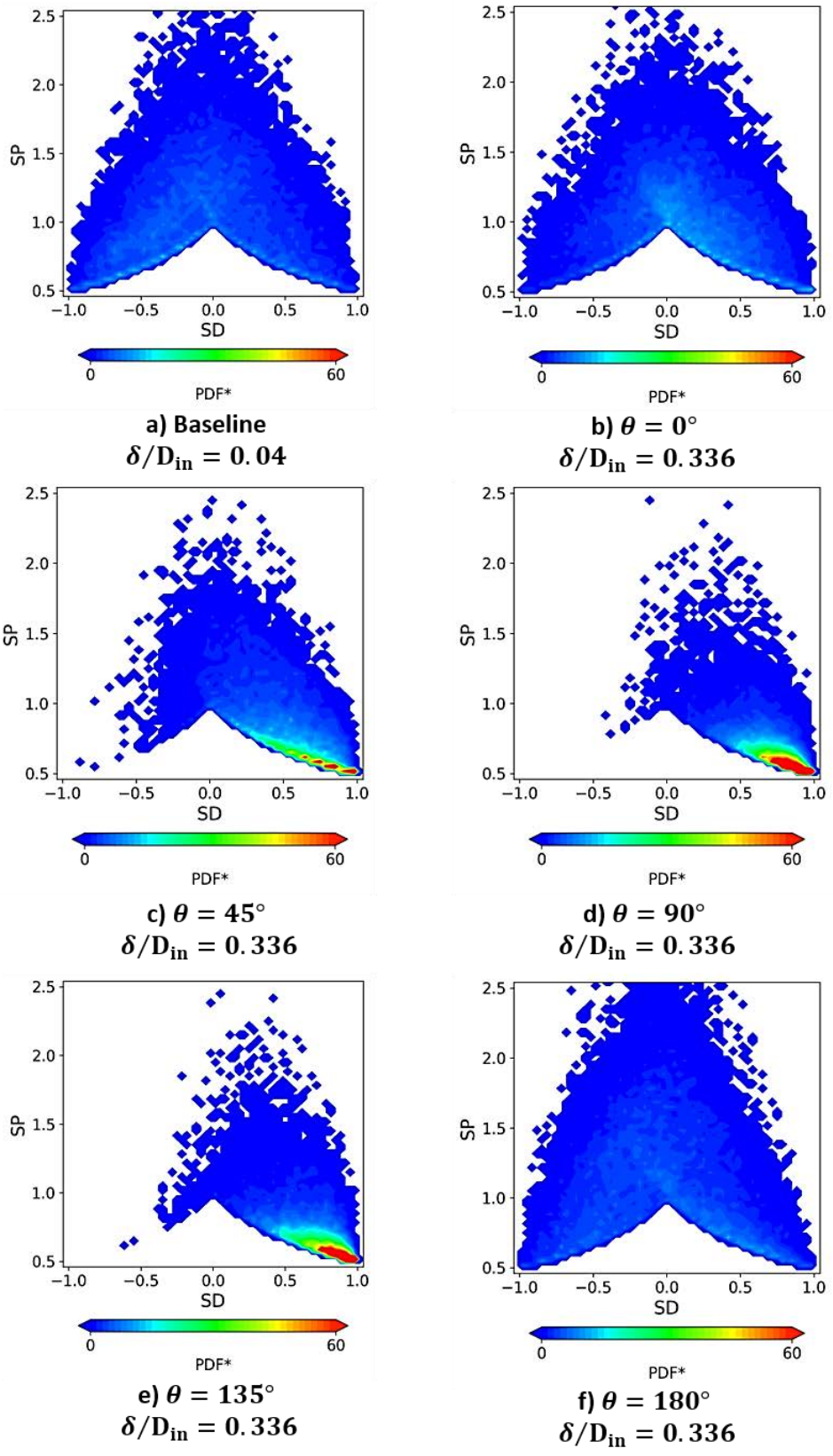

Figure A.2-6: SP_SD probability maps at $r/R_{AIP} = 0.9$ for the baseline and the cases with BL ingestion at θ=0°,45°,90°,135° and 180°.

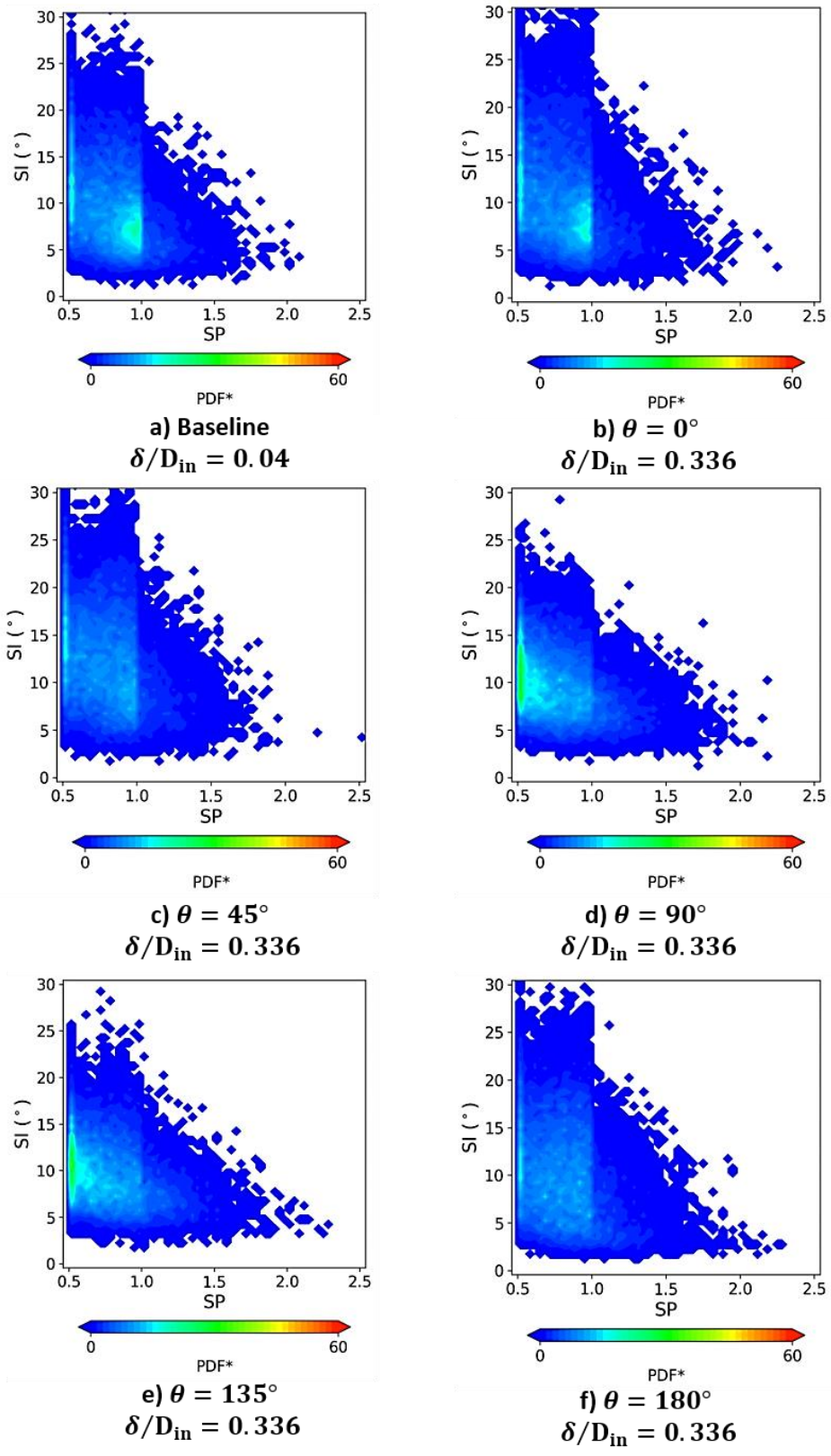

Figure A.2-7: SI_SP probability maps at $r/R_{AIP} = 0.2$ for the baseline and the cases with BL ingestion at θ=0°,45°,90°,135° and 180°.

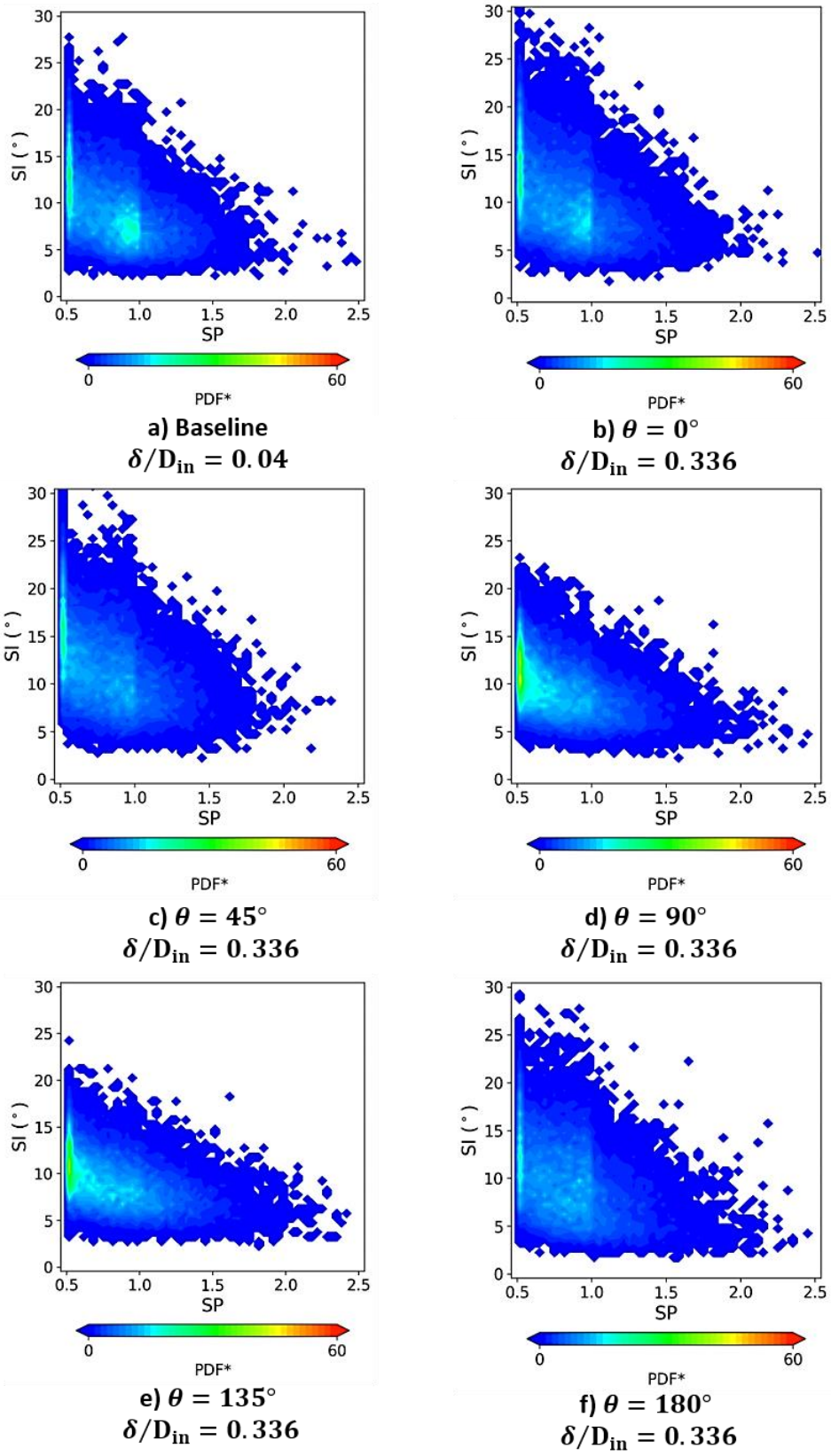

Figure A.2-8: SI_SP probability maps at $r/R_{AIP} = 0.3$ for the baseline and the cases with BL ingestion at θ=0°,45°,90°,135° and 180°.

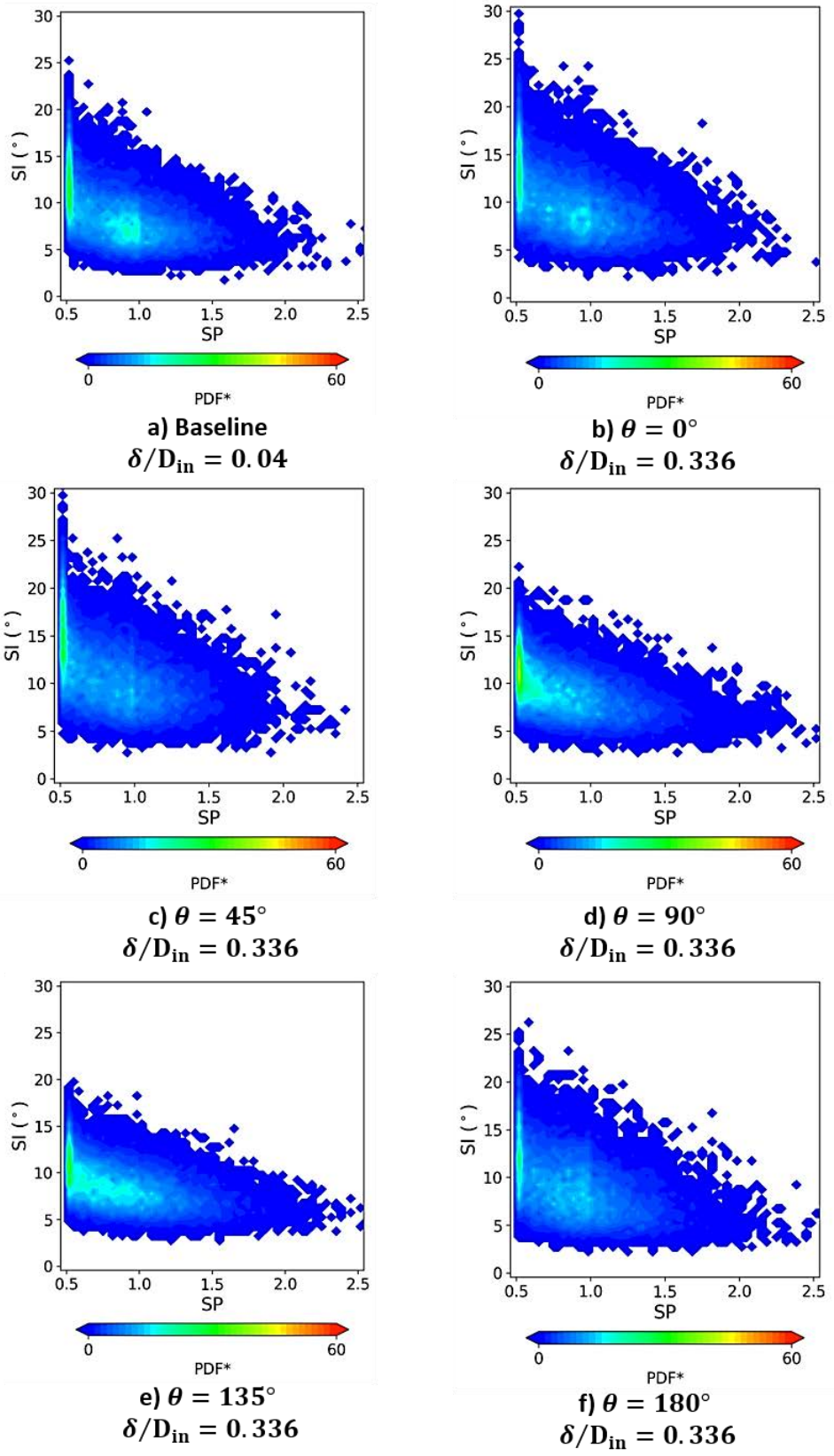

Figure A.2-9: SI_SP probability maps at $r/R_{AIP} = 0.4$ for the baseline and the cases with BL ingestion at θ=0°,45°,90°,135° and 180°.

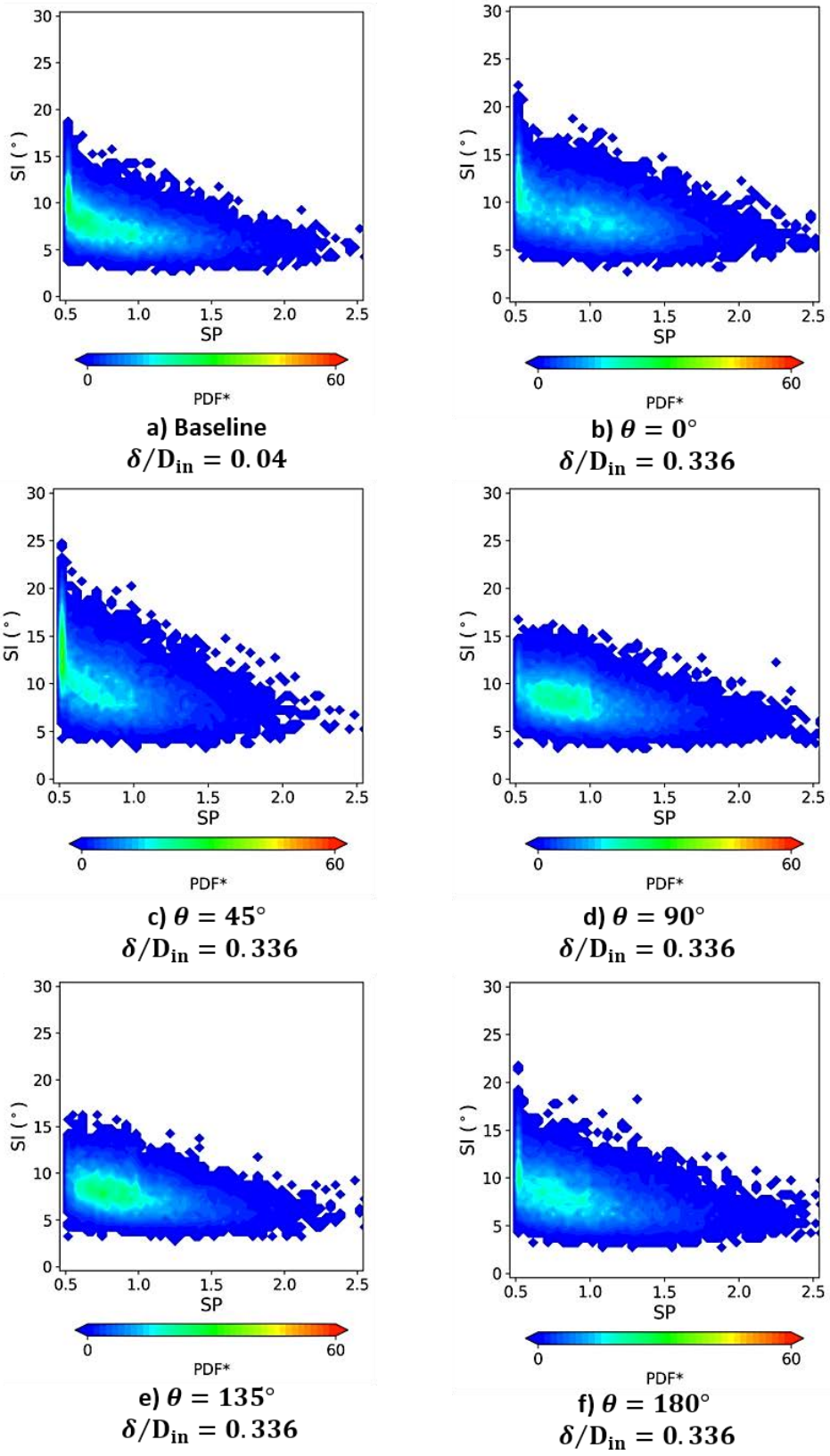

Figure A.2-10: SI_SP probability maps at $r/R_{AIP} = 0.6$ for the baseline and the cases with BL ingestion at θ=0°,45°,90°,135° and 180°.

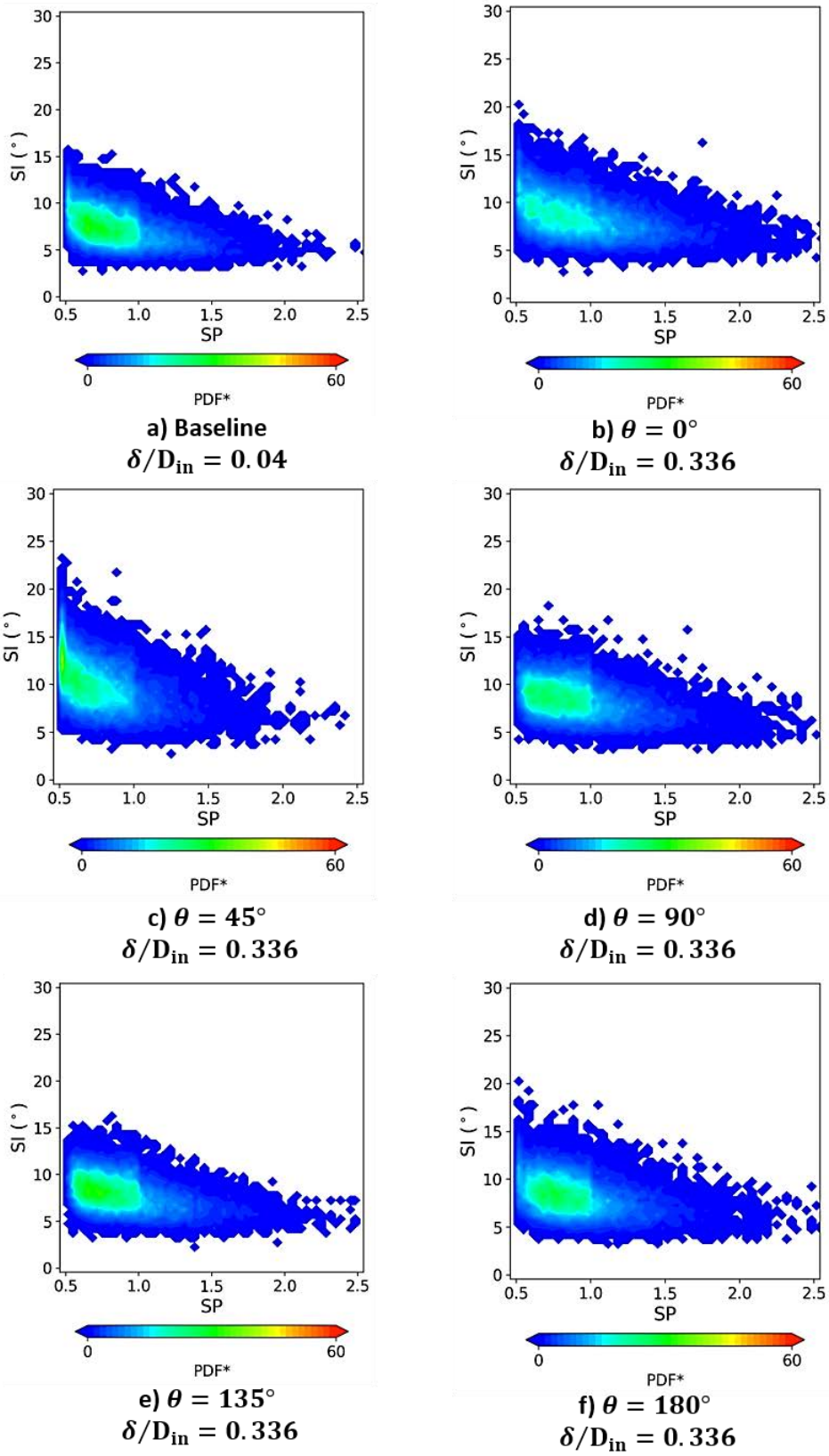

Figure A.2-11: SI_SP probability maps at $r/R_{AIP} = 0.7$ for the baseline and the cases with BL ingestion at θ=0°,45°,90°,135° and 180°.

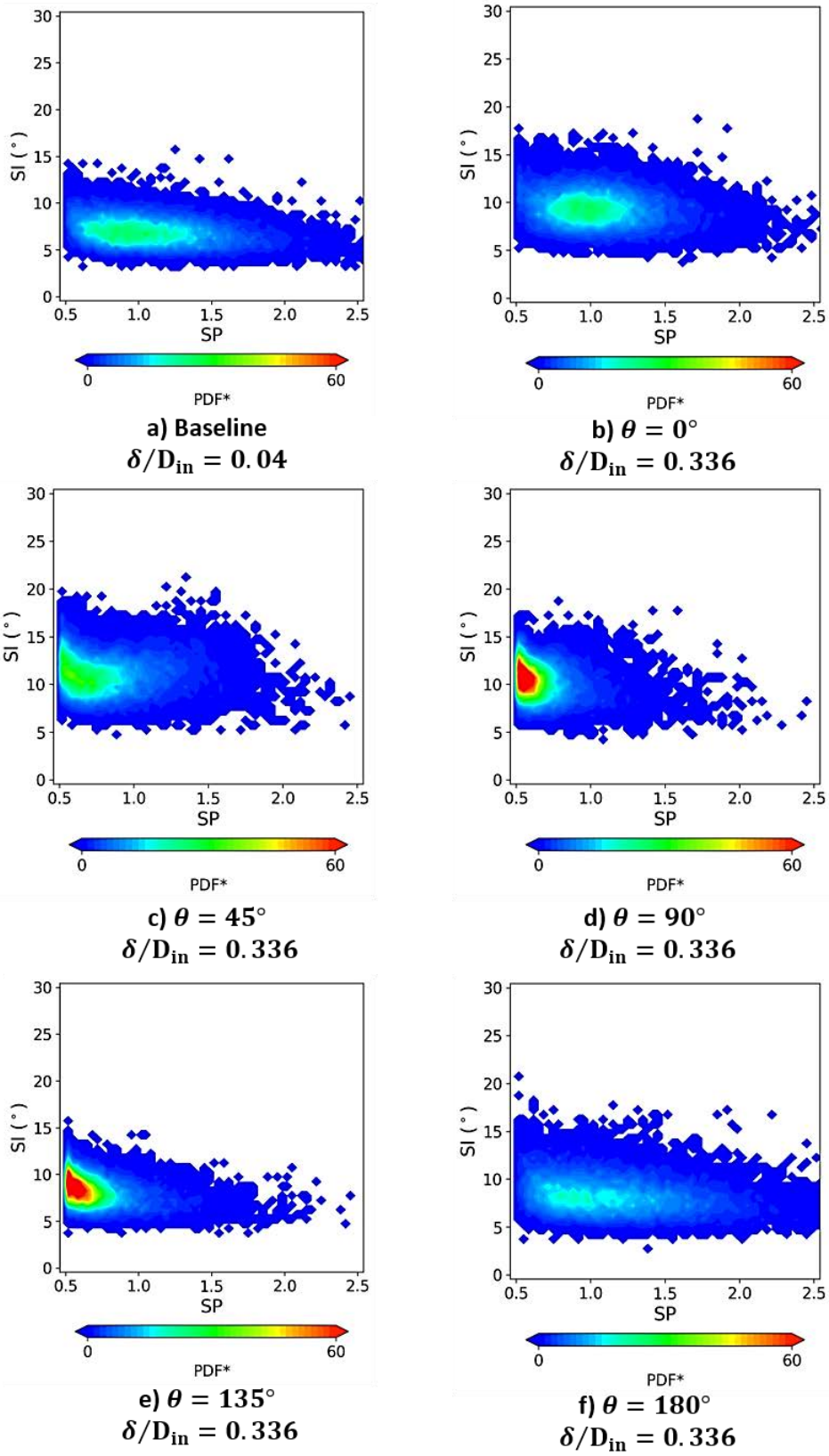

Figure A.2-12: SI_SP probability maps at $r/R_{AIP} = 0.9$ for the baseline and the cases with BL ingestion at θ=0°,45°,90°,135° and 180°.